Physik Department
der Technischen Universität München
Theoretische Physik T30

Dynamics of single polymers at surfaces

Andreas Serr

Vollständiger Abdruck der von der Fakultät für Physik der Technischen Universität München zur Erlangung des akademischen Grades eines

Doktors der Naturwissenschaften (Dr. rer. nat.)

genehmigten Dissertation.

Vorsitzender:		Univ.-Prof. Dr. A. R. Bausch
Prüfer der Dissertation:	1.	Univ.-Prof. Dr. R. Netz
	2.	Univ.-Prof. Dr. R. Metzler

Die Dissertation wurde am 07.08.2007 bei der Technischen Universität München eingereicht und durch die Fakultät für Physik am 29.08.2007 angenommen.

Die folgende Arbeit wurde unter der Betreuung durch Herrn Prof. Dr. Roland R. Netz am Physik-Department der Technischen Universität München sowie an der Fakultät für Physik der Ludwig-Maximilians-Universität München angefertigt.

Herrn Prof. Dr. R. R. Netz danke ich herzlich dafür, dass er diese Arbeit begleitete und mit seiner Diskussionsbereitschaft und seinem Interesse zahlreiche fundamentale Beiträge zu Ihrer Anfertigung leistete, alle hier vorgestellten Teilprojekte mit seinen Ideen initiierte und mich zu ihrer wissenschaftlichen Bearbeitung anleitete. Große Teile von Kapitel 2 stammen aus zwei seiner Vorlesungen.

Herrn Prof. Dr. R. Metzler bin ich sehr dankbar dafür, dass er sich bereit erklärte, diese Arbeit zu prüfen. Bei Herrn Prof. Dr. H. J. Kreuzer und Herrn F. Hanke, PhD, bedanke ich mich für ihre fachliche Hilfestellung auf dem Gebiet der Transfermatrixmethode zur Berechnung von Polymerkonformationen und ihre vorzügliche Gastfreundschaft wärend eines zweimonatigen Aufenthalts an der Dalhousie University in Halifax, Kanada. In Zusammenarbeit mit Herrn F. Hanke wurden außerdem einige quantenchemische Berechnungen zur mechanischen Elastizität von Polymerfragmenten angefertigt. Herrn Prof. Dr. H. E. Gaub, Herrn Dr. F. Kühner und Herrn Dipl.-Phys. M. Erdmann bin ich für eine fruchtbare Kollaboration und zahlreiche Gespräche und Anregungen mit dem Schwerpunkt der Reibung von einzelnen Polymeren an Festkörperoberflächen dankbar. Herrn Dr. D. Horinek danke ich für seine umfangreiche Hilfe bei der Durchführung von atomistischen Molekulardynamiksimulationen von Spinnenseidenproteinfragmenten, Herrn Prof. Dr. T. Hugel, Herrn Dipl.-Phys. M. Geisler und Herrn Dipl.-Phys. T. Pirzer für kraftspektroskopische Untersuchungen dieser Proteine. Auch diese Zusammenarbeit war besonders inspirierend und hat viele Fragen und Antworten auf dem Gebiet der hydrophoben Wechselwirkung aufgeworfen. Herr Dipl.-Phys. C. Sendner hat durch Bereitstellung von Programmcode und viele Diskussionen maßgeblich zur Aufklärung des Einflusses hydrodynamischer Wechselwirkung auf die Nichtgleichgewichtsadsorption von Polymeren beigetragen. Herrn Prof. Dr. A. R. Bausch, Frau Dr. P. A. Neff und Herrn Dipl.-Phys. B. K. Wunderlich danke ich für interessante Einblicke in polymerdesorptionsgestützte Mikrosensoren und deren biophysikalische Anwendung.

Für materielle und ideelle Unterstützung spreche ich dem Graduiertenkolleg CompInt des Elitenetzwerks Bayern meinen Dank aus. Der Deutschen Forschungsgemeinschaft bin ich für die zweitweise Finanzierung meiner Forschungs- und Lehraufgaben dankbar. Beim Leibniz-Rechenzentrum bedanke ich mich für Rechenzeit und bei seinen Mitarbeitern für ihren Support.

»Ich habe Sie nicht um Ihre Meinung, sondern um eine Auskunft ersucht.«

»Es tut mir außerordentlich leid, aber ich bin nicht in der Lage, Ihnen die gewünschte Auskunft zu erteilen.«

»Sie sind kein Kavalier, mein Herr.«

Mintzlaff machte ein zerknirschtes Gesicht. »So ist es im Leben«, sagte er. »Sie baten mich um eine Auskunft, die ich Ihnen nicht geben konnte, und ich erhalte eine Auskunft, um die ich Sie nicht gebeten habe.«

Erich Kästner, Der Zauberlehrling

Contents

List of Figures

Chapter 1

Introduction and outline

1.1 Polymers close to solid surfaces

A large number of technological applications makes use of polymers adsorbed to solid substrates. Especially polyelectrolytes which are polymers with charged or ionizable monomers can stabilize colloidal suspensions as employed in pharmaceutical or cosmetic products, or by the food industry [1–5]. Also modern water soluble paints and anti-limestone washing powder rely on polymer technology. The use of polycarboxylates as incrustation inhibitors is explained in Fig. 1.1. On the other hand, via bridging or depletion forces polymers provide means to control phase separation and flocculation as used in waste water treatment, oil recovery or mining [5–8]. Polymers function as adhesives and strength enhancing agents, *e.g.* in paper making, for adhesive tapes or even glueing metal parts together as used in the automotive industry [5, 9]. Polymers in the form of thin films adsorbed to substrates or cement particles can greatly reduce friction forces and are thus widely used as lubricants [5, 10]. Medical applications such as implants make use of tailor-made combinations of biological polymers and solid substrates. Biosensors and biologically functionalized chips are expected to have great impact not only in the medical sector but also for other technologies [11]. From a different point of view, many of the biologically active molecules are macromolecules or polymers, such as the nucleic acids DNA and RNA, sugar molecules, or the huge families of proteins and polypeptides [12]. Both to understand their functioning in natural environments and to build up powerful analysis and separation tools it is vital to learn about the interaction of biopolymers with solid substrates. These extensive fields of industrial applications as well as fundamental questions in biosciences form the central motivation to investigate polymers close to surfaces.

In practically all cases mentioned above, the polymer-substrate system is in contact with a solution; other applications involve the presence of a liquid at some preparatory stage. Biopolymers in contact with solid substrates are virtually always also immersed in a liquid solvent, usually water. In a large number of applications and problems these systems are characterized by a small concentration of the

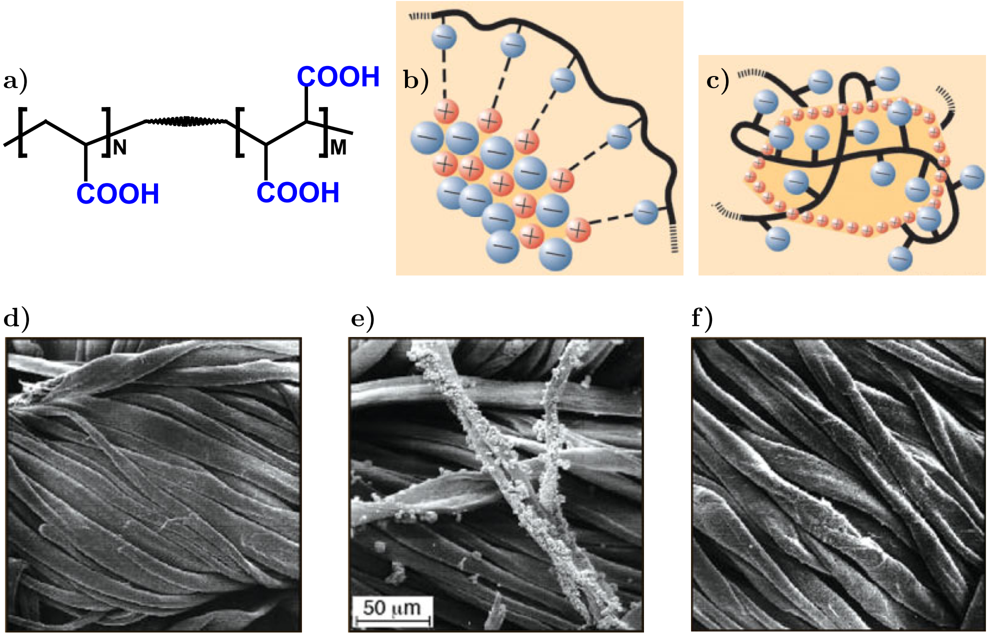

Figure 1.1: Polycarboxylates, *i.e.* negatively charged block copolymers mainly derived from acrylic and maleic acid, see **a)**, are common incrustation inhibitors and are thus widely used in washing powders, desalination plants and other applications involving heat transfer in solution [5]. These functional polymers make up between 3 and 8 percent by weight of modern washing powders corresponding to a market of about 2×10^4 tons per year in Germany [13, 14]. Polycarboxylates function as cobuilders and carriers, *i.e.* they build complexes with metal ions such as Ca^{2+} or Mg^{2+} and pass these ions on to builders with a larger ion uptake capacity, such as zeolites. Thus, they support the sequestration of these metal ions and thereby reduce the formation of calcite crystals. However, recently it has been found that inhibition of incrustation is also accomplished through the complexation of crystal nuclei by the polycarboxylates (see **b)**, taken from Ref. [5]) and by the adsorption of the polycarboxylates on crystallites or on growth surfaces of larger crystals inhibiting further growth (see **c)**, taken from Ref. [5]) [15, 16]. This process is a perfect example for the application of functional polymers in conjunction with solid surfaces of colloidal particles. The progress in understanding the complexation and adsorption processes has indeed been complemented by simulation tools [15, 17]. **d)-f)** Electron micrographs demonstrate the efficiency of incrustation inhibition (taken from Ref. [15]); they show **d)** a cotton fabric, **e)** a cotton fiber after a 5 minute exposure to $CaCO_3$ precipitation when calcite deposition is clearly visible and **f)** a fiber after 5 minute exposure in the presence of polycarboxylates where no calcite deposition is observed.

polymers in the solvent. The so-called dilute regime is reached when characteristic dimensions of size, such as the range of interaction or the radius of gyration of the polymer, are smaller than the typical distance between any two polymer molecules in solution. In other words, in the dilute regime interactions of polymers between each other need not to be taken into account. Applicationwise, this is an important limit, again sometimes due to the dilute character of initial stages in polymer accumulating systems. On the scientific side so-called single polymer experiments have become available with the rather recent advent of single molecule probes such as the atomic force microscope (AFM) [18], optical and magnetic tweezers [19], and confocal optical methods, *e.g.* confocal fluorescence microscopy or fluorescence correlation spectroscopy (FCS) [20]. These experimental methods have tremendously improved the understanding of dilute systems, and in some cases go far beyond methods averaging over whole ensembles.

One of the most direct experimental means to follow the adsorption of polymers to solid surfaces is to partly pull off the polymer from the surface which it is adsorbed to and simultaneously measure the force needed to do that. In thermodynamic equilibrium this process of desorption is reversible and perfectly resembles the reverse situation of adsorption. A polymer can be forced to desorb from a surface by increasing the distance of two surfaces which the polymer is bridging. Experimental realizations have been achieved with the surface force apparatus (SFA) with micrometer sized surfaces and in the single polymer regime with the AFM force spectroscopy and the tweezers technology [10, 21]. The situation in a typical AFM experiment is depicted in Fig. 1.2. At the substrate side the polymer can be either adsorbed by weak interactions, also called physisorbed, or grafted by strong covalent bonds. At the other side it is covalently bound to the surface of the AFM cantilever tip whose position can be controlled with a precision between one Ångstrom and one nanometer along the surface normal, which will in this work be denoted as the $\hat{z}$ direction, and in the lateral directions $\hat{x}$ and $\hat{y}$. The bending of the cantilever tip is detected through the deflection of a laser light beam and can be converted into a force acting on the cantilever once its bending stiffness has been determined. Using commercial setups the force resolution is in the piconewton range. By moving the AFM cantilever in any dimension it is possible to record response forces of the polymer caused by *e.g.* stretching the polymer, desorbing it from the surface or moving it across the surface. Since these experiments are typically conducted in solution, AFM force spectroscopy provides excellent access to many questions of polymer-surface systems in the dilute polymer regime. Many, but not all of the problems discussed in the following chapters are related to AFM single molecule experiments or could be tackled with that approach.

Many applications of polymers that are mentioned above have in common their inherent non-equilibrium state. Often, such situations are less well understood from the theoretical point of view and despite great efforts in the past still lack understanding in many areas. Also due to the advent of experimental techniques with sufficient time resolution such as FCS, the theoretical description of single polymer systems far from equilibrium and their dynamics is an active research area. In this

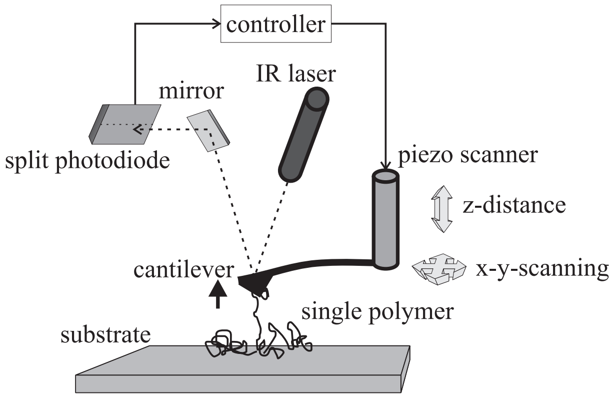

Figure 1.2: Principle of AFM single polymer experiments. The polymer is attached to both a solid substrate and the cantilever tip. Using a laser light beam, the cantilever deflection is recorded. The force acting on the cantilever tip is calculated from the previously calibrated cantilever spring constant. At the same time the cantilever position can be controlled in all three dimensions by piezo elements.

work, both equilibrium states and the non-equilibrium dynamics of single polymers close to surfaces are explored.

1.2 Theoretical descriptions of polymers

Many of the relevant biological macromolecules and industrially used polymers are so-called linear polymers, *i.e.* they have an essentially sequential backbone in which one monomer unit is attached to the next and so forth as schematically depicted in Fig. 1.2. In this work we will solely focus on this linear type of polymers as opposed to *e.g.* branched polymers or comb-like polymers. Even in the case of very simple systems consisting of only linear polymers in the dilute regime, the theoretical approaches to polymers at solid-liquid interfaces can be very demanding. This is connected to the *softness* of these systems which are mainly characterized by two facts. Firstly they are typically composed of a large number of molecular constituents, and secondly the energies that govern the intra- and intermolecular interactions of these constituents are comparably low. Commonly, the energy scale is of the order of the thermal energy $k_\mathrm{B}T$, where k_B and T are the Boltzmann constant and the absolute temperature, respectively. These two facts cause a huge number of conformations and realizations to be statistically relevant [22–24], and make the system very susceptible to perturbations — in a more general sense the system is soft. Large fluctuations in many observables and the seemingly random Brownian motion, which both are not typical for phenomena in the macroscopic world, are two further consequences [25].

From a physical point of view, the interaction forces between solvent and polymer molecules and surface atoms are due to the chemical properties and electron distributions of these molecules. For all of the most relevant systems the rather fundamental approach solving for these interactions is in principle known. However this *ab initio* approach in which basically the Schrödinger equation is solved is currently only feasible for system in the range of a few hundreds to thousands of atoms [26]. With very few outstanding exceptions, the calculation of dynamic properties is limited to the tens of picoseconds timescale and to systems of less than one hundred atoms [27, 28].

In order to go beyond these limitations, a common approach is to coarse-grain the system and describe it solely by its constituting atoms instead of the full coupled set of nuclei and electrons. The energy of the system is calculated using empirically fitted or *ab initio* based force fields and potentials, the time evolution in these so-called atomistic molecular dynamics (MD) simulations is usually done in a classical Newtonian way [29]. With systems as large as some 10^4 to 10^5 atoms, current computer power can be used to tackle problems in the tens to hundreds of nanoseconds regime.

Considering our interest in the properties of a *solute*, namely the polymer, it is worthwile seeking to simplify the description of the comparably huge number of *solvent* molecules. In a first step, the *solvent* molecules can be taken into account by continuum fields of momentum and mass in the case that the length scale of interest is larger than the typical solvent length scale. The foundation for that is the Navier-Stokes equation which is an application of Newton's equation of motion to the mass and momentum fields of the solvent [30]. At ambient conditions or under perturbations of typically moderate magnitude, the solvent properties are virtually equilibrated and homogeneous. If secondly the dynamics of the problem are slow enough as compared to the propagation speed of a sound wave, we can assume instantaneous solvent rearrangements and thus a quasi-stationary situation for the solute. Hence, the solvent is to a good approximation incompressible, and inertial forces acting on the solvent molecules can be neglected as compared with viscous forces. This is the case for non-turbulent flow or vanishing Reynolds number, which is the ratio of the inertial term and the viscous term. It is given by $\mathrm{Re} = \rho V L/\eta$ where L is a typical length scale of the problem, V a typical solute or flow field velocity, and ρ and η the density and viscosity of the solvent, respectively. Using characteristic values from the area of soft matter and biological physics, $V \sim 1\,\mu\mathrm{m/s}$, $L \sim 1\,\mu\mathrm{m}$, and taking the viscosity and density of water, the Reynolds number amounts to $\mathrm{Re} \sim 10^{-6}$, and the inertial term can indeed be dropped. With these three assumptions we arrive at a linear equation for the solvent flow field at position $\boldsymbol{r}$ in space, the Stokes equation, which reads

$$\boldsymbol{\nabla}_{\boldsymbol{r}} p(\boldsymbol{r}) - \eta \boldsymbol{\nabla}_{\boldsymbol{r}}^2 \boldsymbol{v}(\boldsymbol{r}) = \boldsymbol{f}(\boldsymbol{r}) \,, \tag{1.1}$$

where p is the pressure field, $\boldsymbol{v}$ the fluid velocity field, and $\boldsymbol{f}$ the field containing all external forces, such as gravitational forces on the solvent. Together with the condition of incompressibility of the fluid,

$$\boldsymbol{\nabla}_{\boldsymbol{r}} \cdot \boldsymbol{v}(\boldsymbol{r}) = 0 \,, \tag{1.2}$$

the Stokes equation describes the flow response of the solvent, given that the above three assumptions of a low Reynolds number, fluid incompressibility, and quasi-stationary flow fields apply.

In a similar way, the equation of motion for a *solute* i can be written as [31, 32]

$$m_i \frac{\mathrm{d}^2 \boldsymbol{R}_i}{\mathrm{d}t^2} = -\zeta_i \left[\frac{\mathrm{d}\boldsymbol{R}_i}{\mathrm{d}t} - \boldsymbol{v}(\boldsymbol{R}_i, t) \right] - \boldsymbol{\nabla}_{\boldsymbol{R}_i} U + \boldsymbol{\xi}_i(t)\,, \tag{1.3}$$

which is the Langevin equation that incorporates the particle-solvent interactions via random noise and a friction term into Newton's equation of motion. Here, $\boldsymbol{R}_i$ is the position of particle i, t is the time, m_i the particle mass, U an external potential, and $\boldsymbol{\xi}_i$ the fluctuating random force due to collisions with the solvent whose characteristics are chosen such that the Langevin equation obliges Boltzmann statistics in thermal equilibrium. ζ_i is the friction coefficient or the inverse mobility which for a spherical particle of diameter a_i can be approximated by the Stokes formula $\zeta_i = \mu_i^{-1} = 3\pi\eta a_i$ [30]. If the timescale of the problem is larger than the momentum relaxation time $\tau \sim m_i/\zeta_i \propto m_i/\eta a_i$, the inertial term can be dropped yielding the overdamped version of the Langevin equation,

$$\frac{\mathrm{d}\boldsymbol{R}_i}{\mathrm{d}t} - \boldsymbol{v}(\boldsymbol{R}_i, t) = \mu_i \left[-\boldsymbol{\nabla}_{\boldsymbol{R}_i} U + \boldsymbol{\xi}_i(t) \right]\,. \tag{1.4}$$

By integrating this simplified equation of motion, which is done in so-called Brownian dynamics (BD) simulations, the previous problem of solving the dynamics of the whole solute-solvent system is solved. All further complications due to the solvent molecules are contained in the solvent flow field $\boldsymbol{v}$. As for the derivation of the Stokes equation necessary, we assume an instantaneous solvent relaxation as compared to the particle relaxation timescale. Even so, the flow field depends on the velocities and positions of all solute particles in solution, $\boldsymbol{v}(\boldsymbol{R}, t) = \boldsymbol{v}(\boldsymbol{R}, t, \{\boldsymbol{R}_j, \mathrm{d}\boldsymbol{R}_j/\mathrm{d}t\})$, in addition to any external space and time variation in the flow field caused by *e.g.* an imposed shear flow. In a very limited number of cases, it is possible to calculate the solvent flow profile due to the solutes exactly by solving the Stokes equation (1.1) with the appropriate boundary conditions. On the contrary it is very often a good approximation to completely neglect the flow field perturbation caused by other solutes and hence the hydrodynamic interactions of two or more solute molecules mediated by solvent collisions. This is called the free-draining case which is particularly justified in the vicinity of most solid surfaces. There, the presence of a no-slip boundary interface causes the hydrodynamic interactions between the solutes to decay faster than they do in bulk solution. This can be seen from the Oseen and the Blake tensors which are the solutions of the Stokes equation at a point in space $\boldsymbol{r}_i$ for a unit point force acting at another point $\boldsymbol{r}_j$. The Oseen tensor is the solution for the bulk case and its components read [30, 31]

$$8\pi\eta G^{\mathrm{O}}_{\alpha\beta}(\boldsymbol{r}_i, \boldsymbol{r}_j) = \frac{\delta_{\alpha\beta}}{r} + \frac{r_\alpha r_\beta}{r^3}\,, \tag{1.5}$$

where α and β each denote a component of Cartesian coordinates, and the mutual distance between the points is given by $r = |\boldsymbol{r}_i - \boldsymbol{r}_j|$. The decay is to leading order given by $1/r$, hence the hydrodynamic interaction is of long-ranged nature. Using the method of images, Blake derived the solution to the same problem with a no-slip boundary plane situated at $z = 0$ [33]. For two points in space, which are near the surface such that their mutual distance is greater than that to the surface, $z_i < r > z_j$, the diagonal components of the Blake tensor in the lateral directions are given up to leading order by [34]

$$G^{\mathrm{B}}_{xx}(\boldsymbol{r}_i, \boldsymbol{r}_j) = G^{\mathrm{B}}_{yy}(\boldsymbol{r}_i, \boldsymbol{r}_j) = \frac{2z_i z_j}{r^3_{xy}} + \mathcal{O}\left(r^{-5}_{xy}\right) , \tag{1.6}$$

where $r^2_{xy} = (x_i - x_j)^2 + (y_i - y_j)^2$ is the squared distance of the points projected to the surface. For the perpendicular direction a similar relationship can be derived. Thus, the hydrodynamic interaction of two solute particles at $\boldsymbol{R}_i$ and $\boldsymbol{R}_j$ with a mutual distance of $r_{ij} = |\boldsymbol{R}_j - \boldsymbol{R}_i|$ decays to leading order and within scaling precision as $1/r_{ij}$ in the bulk case and $1/r^2_{ij}$ or $1/r^3_{ij}$ for solutes near a surface. Hence specifically at surfaces free-draining BD simulations capture the essential parts of the physical picture, and we can even to a quantitative level assume the solvent flow field $\boldsymbol{v}(\boldsymbol{R}, t)$ to be *solely* given by the externally applied flow field.

On the side of the solutes, *i.e.* in our case the polymer, another coarse-graining can be employed to simplify the picture. The atomistic chain can be coarse-grained to a discrete chain in which usually spherical beads represent groups of atoms. These beads are often, but not necessarily identical with chemical monomers, cf. Ref. [35]. Of course, further re-parameterization of the interaction potentials is necessary. One commonly used model to describe flexible polymers is the freely jointed chain (FJC) in which the nearest-neighbor monomers are connected by bonds of the same length a, but where the bonds are uncorrelated along the chain [22]. Excluded volume effects and other type of non-nearest neighbor interactions can optionally be taken into account in such 'bead-necklace' strings. Simplified polymer models have found their application both in coarse-grained BD simulations as well as in non-numerical theoretical approaches, *e.g.* in the path integral formulation of polymers [35].

Considering available computer resources, it has become apparent over the last few decades that in order to pursue both equilibrium and dynamic studies in the biological and soft matter context an appropriate compromise must be chosen from the numerical and analytical methods present. Within this work we follow this approach. Besides analytical methods and scaling arguments, three main numerical tools are used, a) *ab initio* quantum chemistry to calculate the realistic equilibrium force response of particular polymers, b) atomistic molecular dynamics to elucidate dynamic processes and friction of a polypeptide molecule on hydrophobic and hydrophilic surfaces, and c) Brownian dynamics simulations for a number of dynamic problems such as polymer friction and non-equilibrium adsorption of polymers. As illustrative examples, we show in Fig. 1.3 three visual representations of these methods. In a) a static *ab initio* calculation of the electrostatic potential on an electron density isosurface of a glycine-cysteine-glycine tripeptide is shown, b) is a simulation snapshot of an atomistic MD simulation of a polypeptide in aqueous solution.

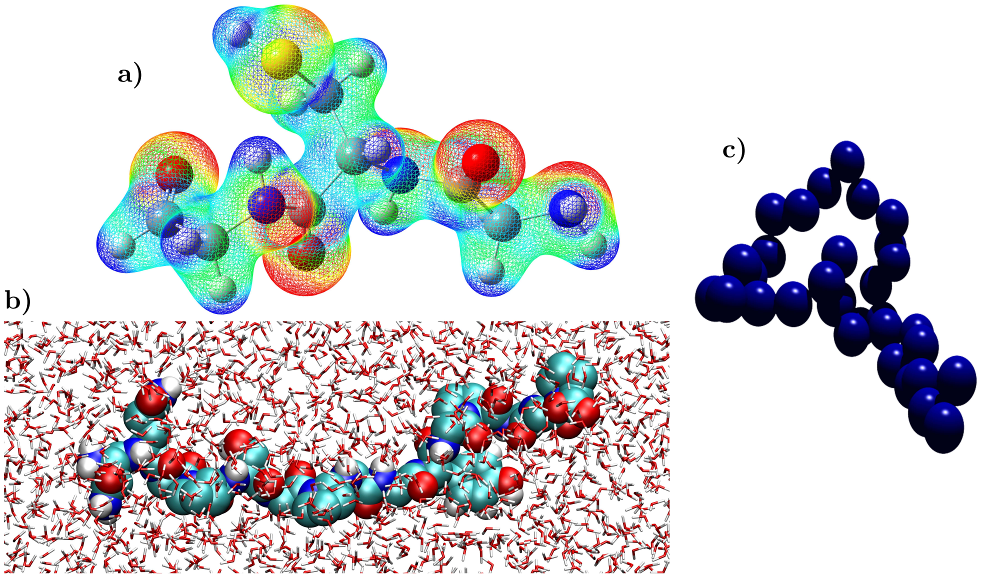

Figure 1.3: Visual representations of polymer models used in this work. **a)** Electrostatic potential on an iso-surface of the electron density of a glycine-cysteine-glycine tripeptide as calculated using an *ab initio* quantum chemistry package. Red denotes low, blue high values of the potential. **b)** Simulation snapshot of an atomistic molecular dynamics (MD) simulation showing a polypeptide consisting of 15 amino acids in aqueous solution. **c)** Coarse-grained polymer chain in which self-avoiding monomer beads are connected to their neighbors by harmonic bonds of equilibrium length a_0. Such models are closely related to analytically treatable bond vector polymer models such as the freely jointed chain (FJC). Pictures throughout this work were generated using GaussView [36], VMD [37], POV-Ray [38], Adobe Illustrator [39], and CorelDRAW [40]. Graphs were produced using Origin [41].

Finally, c) shows the underlying idea of a coarse-grained polymer model as used in Brownian dynamics simulations.

1.3 Thesis outline

This work treats non-equilibrium and equilibrium aspects of polymers in the vicinity of surfaces, *i.e.* polymers attached or adsorbed to surfaces and polymers in motion close to a solid surface. The thesis is divided into chapters according to common subjects rather than methods. Each chapter starts with a short introduction into the general topic, which illustrates how this work is related to other contributions and experiments. At the end of each section its major results are concluded in a brief summary.

In Chapter 2 the equilibrium adsorption of a single polymer to a solid, flat substrate is reviewed, which will be useful in later chapters for the understanding of dynamic, non-equilibrium processes. Two approaches for ideal polymers are described. BD simulations and their application to polymer adsorption are discussed. Special emphasis is put on how simulations of finite duration and system size can give information on the thermodynamic limit of an infinitely long polymer. The chapter ends with some remarks on polymer desorption as applied to AFM single polymer experiments.

The dynamics of adsorption depend on the friction forces that a polymer experiences both in the solvent and on the substrate. The other way around, polymer mobilities on substrates crucially depend on the – usually attractive – polymer-surface interactions. This interplay is the focus of Chapter 3. It starts with a discussion on the two regimes of AFM single molecule experiments: polymers firmly attached to the surface *vs.* freely sliding ones. The intermediate regime of finite polymer friction on a solid substrate is analyzed. It is then shown that a well-known system, the Frenkel-Kontorova model, can serve as a simplified model for the friction of a polymer at a corrugated substrate. Finally, the atomistic details of the dissipative mechanisms in polypeptide motion over solid substrates are studied with MD simulations. Fundamental differences are shown for an important type of substrate classification: hydrophobic *vs.* hydrophilic surfaces.

In Chapter 4 a related non-equilibrium situation is studied, namely the influence of external flow fields on polymer adsorption. Among other methods BD simulations serve as a valuable tool. For the simple case of a pulled polymer close to a flat, homogeneous surface it is shown that pulling enhances adsorption. A similar mechanism comes into play for simple shear flow. Hydrodynamic effects are studied using a hydrodynamic coupling formalism which takes the vicinity of a no-slip boundary caused by the substrate into account. Further it is shown how surface corrugation affects non-equilibrium adsorption.

Many cases considered in this thesis are far from equilibrium, where linear response treatments such as the Gaussian chain approximation usually fail. In a context going beyond linear response theory, the elastic response of polymers to stretching forces is treated in Chapter 5. Existing chain models for the elasticity of polymers are extended by a discrete, but extensible and semi-flexible chain model. Its numerical implementation in a transfer matrix formalism is presented. The transfer matrix method is extended for alternating copolymers and applied to polypeptides. Realistic microscopic parameters are determined from *ab initio* quantum chemistry calculations. The consequences of rotational rigidity on polymer elasticity are discussed and another chain model is proposed to cope with such situations. Its application to polypeptides is shown.

In the summary, Chapter 6, the most important conclusions are presented and possible extensions are briefly discussed.

Chapter 2

Single polymer adsorption in equilibrium

The equilibrium adsorption of polymers on solid substrates is a long-studied phenomenon with diverse applications as discussed in Section 1.1. Experimental and theoretical investigations are numerous, cf. Refs. [1, 35] for references. Important theoretical contributions in the dilute and semi-dilute regimes have been made by de Gennes [42, 43] and Eisenriegler *et al.* [44, 45]. More recent works addressed the adsorption of polyelectrolytes [46, 47], the decomposition of adsorption forces into chemical, electrostatic and hydrophobic contributions [48, 49], dynamics of adsorbed chains [50], and the influence of patterned surfaces [51], just to mention a few. In this chapter two different methods to treat the adsorption of ideal polymers are reviewed, the diffusion equation approach in Section 2.1 and the Poland-Scheraga model in Section 2.2. In Section 2.3 Brownian dynamics (BD) simulations are used to discuss the equilibrium adsorption of flexible polymers of finite length and finite monomer exclusion volume. Finally, Section 2.4 analyzes forced partial desorption as applicable to AFM experiments.

2.1 The diffusion equation approach

In the limit of very long, unperturbed or weakly perturbed chains all coarse-grained polymer models coincide with the ideal Gaussian chain [31]. This polymer model has been used in numerous studies, mainly due to its simplicity often leading to solutions in closed form and due to its generality. Also for the case of polymer adsorption this approach has been used [52–54]. Here we review some aspects of the adsorption of an ideal Gaussian chain.

In an external potential $U(\boldsymbol{R})$ a differential equation for the polymer end-to-end probability distribution function or Green's function can be derived which is called the polymer diffusion equation and which resembles the Schrödinger equation for quantum mechanical systems, but with imaginary time [31, 35, 55],

$$\left(\frac{a^2}{6}\boldsymbol{\nabla}^2 - \frac{U(\boldsymbol{R})}{k_\mathrm{B}T}\right) P_t(\boldsymbol{R};\boldsymbol{R}_0) = \frac{\partial P_t(\boldsymbol{R};\boldsymbol{R}_0)}{\partial t}\,, \tag{2.1}$$

where a is the diameter of one monomer or the so-called Kuhn length, t is the continuous contour variable with $0 < t < N$, and $P_t(\boldsymbol{R};\boldsymbol{R}_0)$ is the probability distribution function for a chain of length t to end at $\boldsymbol{R}$ given that it starts at $\boldsymbol{R}_0$. The boundary condition is given by

$$P_0(\boldsymbol{R};\boldsymbol{R}_0) = \delta(\boldsymbol{R}-\boldsymbol{R}_0)\,. \tag{2.2}$$

After solving the eigenvalue equation independent of the contour length,

$$\left(\frac{a^2}{6}\boldsymbol{\nabla}^2 - \frac{U(\boldsymbol{R})}{k_\mathrm{B}T} - A_k\right) \phi_k(\boldsymbol{R}) = 0\,, \tag{2.3}$$

for the eigenvalues A_k and eigenfunctions $\phi_k(\boldsymbol{R})$, we can now write the probability distribution function for the end-to-end distance of a chain with N monomers starting at $\boldsymbol{R}_0$ and ending at $\boldsymbol{R}_N$ as

$$P_N(\boldsymbol{R}_N;\boldsymbol{R}_0) = \frac{1}{Q}\sum_k \exp\left(-A_k N\right)\phi_k(\boldsymbol{R}_0)\phi_k(\boldsymbol{R}_N)\,, \tag{2.4}$$

where Q is a normalization constant. In the thermodynamic limit $N \to \infty$, ground state dominance (GSD) applies, *i.e.* only the solution with the lowest eigenvalue A_0 contributes. It can be shown that the expectation value of the free energy is within GSD given by $A_0 k_\mathrm{B}T$. Also, Eq. (2.4) can be solved for vanishing external potential yielding the well-known Gaussian distribution function

$$P_N^{U=0}(\boldsymbol{R}_N;\boldsymbol{R}_0) = \left(\frac{3}{2\pi N a^2}\right)^{3/2} \exp\left(-\frac{3(\boldsymbol{R}_N-\boldsymbol{R}_0)^2}{2Na^2}\right). \tag{2.5}$$

In a similar fashion we can expand the equilibrium probability distribution function of finding any monomer of a polymer with N monomers at the position in space $\boldsymbol{R}$, $W_N(\boldsymbol{R})$, in the eigenfunctions as

$$\begin{aligned} W_N(\boldsymbol{R}) = \frac{1}{Q'}\int_0^N \mathrm{d}t \int \mathrm{d}^3\boldsymbol{R}_0 \int \mathrm{d}^3\boldsymbol{R}_N \sum_{k=0}^{\infty} \exp\left(-A_k t\right)\phi_k(\boldsymbol{R})\phi_k(\boldsymbol{R}_0) \\ \times \sum_{l=0}^{\infty} \exp\left(-A_l (N-t)\right)\phi_l(\boldsymbol{R})\phi_l(\boldsymbol{R}_N)\,, \end{aligned} \tag{2.6}$$

where Q' is another normalization constant. Under GSD, this equation simplifies into

$$W_N^{\mathrm{GSD}}(\boldsymbol{R}) = \frac{1}{Q''}\phi_0^2(\boldsymbol{R})\,, \tag{2.7}$$

where Q'' again provides proper normalization. Using formalisms known from standard quantum mechanics, one can now solve Eq. (2.3) for an attractive square well potential at a hard wall with rescaled depth χ and range κ^{-1},

$$U(\boldsymbol{R}) = \begin{cases} \infty & \text{for } Z \leq 0 \text{ (region 0)}, \\ -\chi k_{\mathrm{B}} T & \text{for } 0 < Z < \kappa^{-1}, \text{ (region I) and} \\ 0 & \text{for } \kappa^{-1} \leq Z \text{ (region II)}, \end{cases} \tag{2.8}$$

where Z is the component of $\boldsymbol{R}$ in the direction of the surface normal $\hat{z}$. After imposing proper boundary conditions at $Z = 0$ and $Z = \kappa^{-1}$ for both ϕ_0 and its first spatial derivative $\frac{\mathrm{d}\phi_0}{\mathrm{d}Z}$, we arrive at the standard solution,

$$\begin{aligned} \phi_0^0 &= 0\,, \\ \phi_0^{\mathrm{I}} &= C^{\mathrm{I}} \sin(K^{\mathrm{I}} Z)\,, \quad \text{and} \\ \phi_0^{\mathrm{II}} &= C^{\mathrm{II}} \exp\left(-K^{\mathrm{II}} Z\right), \end{aligned} \tag{2.9}$$

where K^i and C^i are constants to be determined. In all cases the upper indices $i \in \{0, \mathrm{I}, \mathrm{II}\}$ denote the regions defined in Eq. (2.8). Using the boundary conditions the constants K^i are obtained as

$$K^{\mathrm{I}} = \frac{\kappa^{-1}}{a} \sqrt{6(\chi + A_0)}\,, \quad \text{and} \tag{2.10}$$

$$K^{\mathrm{II}} = \frac{\kappa^{-1}}{a} \sqrt{-6A_0}\,. \tag{2.11}$$

Hence, a discrete spectrum or in other words a bound state is only obtained for a negative free energy, $A_0 < 0$. More precisely, the desorption transition is located at a finite value of the adsorption internal energy, namely

$$\chi^* = \frac{\pi^2 a^2}{24\kappa^{-2}}\,, \tag{2.12}$$

as suggested by the boundary conditions. For the adsorbed state we define $\Delta = \chi - \chi^*$ as the rescaled distance from the desorption transition. Expanding Eq. (2.10) for small Δ and using Eq. (2.12) we arrive at

$$\frac{\langle A \rangle}{N k_{\mathrm{B}} T} = A_0 = -\frac{3\kappa^{-2}}{2a^2} \Delta^2\,, \tag{2.13}$$

for the rescaled free energy per monomer in the case of GSD. Close to the desorption transition, ϕ_0 is dominated by conformations far away from the surface, ϕ_0^{II}, and we can write for the expectation value of the adsorption energy per monomer in the asymptotic limits $\Delta \to 0$ and $N \to \infty$

$$-\frac{\langle U \rangle}{N k_{\mathrm{B}} T} \sim \chi \frac{\int_0^{\kappa^{-1}} \mathrm{d}Z\, (\phi_0^{\mathrm{I}})^2}{\int_0^{\infty} \mathrm{d}Z\, (\phi_0^{\mathrm{II}})^2} \sim \frac{3\kappa^{-2}}{a^2} \Delta + \mathcal{O}\left(\Delta^2\right), \tag{2.14}$$

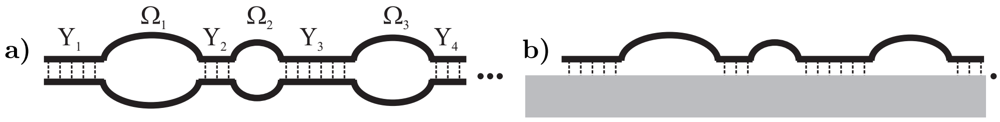

Figure 2.1: The Poland-Scheraga model as applied to **a)** DNA denaturation and **b)** polymer adsorption on a solid surface. The polymer consists of bound, helical parts or trains with Υ_i base pairs or monomers and loops or tails with Ω_i unbound pairs of bases or monomers.

where we used Eqs. (2.13) and (2.9). Similarly, the inverse of the mean height is asymptotically given by

$$\langle Z\rangle^{-1} \sim \left(\frac{\int_0^{\kappa^{-1}} \mathrm{d}Z\, Z(\phi_0^{\mathrm{I}})^2}{\int_0^{\infty} \mathrm{d}Z\, (\phi_0^{\mathrm{II}})^2}\right)^{-1} \sim \left(\frac{\kappa^{-1}a^2}{\Delta} + \mathcal{O}\left(\Delta^2\right)\right)^{-1} . \tag{2.15}$$

Hence, within GSD for both the inverse mean height and the adsorption energy per monomer, linear scaling in $\Delta = \chi - \chi^*$ is obtained.

Summarizing, the diffusion equation approach provides means to calculate the adsorption behavior of Gaussian polymers in the thermodynamic limit. Methods already established in quantum physics can be applied and already provide solutions for simple potentials such as the square well potential, Eq. (2.8).

2.2 The Poland-Scheraga framework

DNA molecules which are the carriers of genetic information consist of phosphate-linked sugar rings to which one of four nucleotides, abbreviated as A, T, C, and G, are bound [12]. Two of these nucleotides can bind to each other, A-T and C-G. These pairs allow two DNA strands of complementary bases to bind and form the typical double helix. A classical description of the denaturation of a double stranded (ds-) DNA molecule which can by parts or entirely unbind into its comprising strands has been formulated by Poland and Scheraga [56]. Considering only complementary strands in their model, the molecule is comprised of loops or unbound parts and of bound or helical parts, see Fig. 2.1a). In the simplest form, all loops are assumed to be symmetric, *i.e.* the number of bases in both parts of one loop is the same. Here we shortly review the basics of the Poland-Scheraga model and its application to the adsorption of a polymer on a solid surface as shown in Fig. 2.1b). The close resemblance in the formulation will be described in more detail later.

The canonical partition function $\mathcal{Z}_N$ for a ds-DNA molecule with k symmetric loops, where one strand of loop i is comprised of Ω_i bases, and k bound parts with Υ_i base pairs is given by

$$\mathcal{Z}_N = \sum_{k=0}^{\infty} \left\{ \prod_{j=1}^{k} \left[\int_0^{\infty} \mathrm{d}\Upsilon_j\, \mathcal{Z}^{\mathrm{b}}_{\Upsilon_j} \int_0^{\infty} \mathrm{d}\Omega_j\, \mathcal{Z}^{\mathrm{u}}_{\Omega_j} \right] \delta\left(N - \sum_{i=1}^{k} (\Upsilon_i + \Omega_i) \right) \right\} , \tag{2.16}$$

where $N = \sum_{i=1}^{k}(\Upsilon_i + \Omega_i)$ is the total number of monomers on one DNA strand, *i.e.* bound or unbound base pairs, $\delta(x)$ is the Dirac delta function, and $\mathcal{Z}_n^{\mathrm{u}}$ and $\mathcal{Z}_n^{\mathrm{b}}$ are the canonical partition functions for loops and bound pieces with n monomers, respectively. The grand-canonical partition function follows as

$$\mathcal{Z}_\lambda = \int_0^\infty \mathrm{d}N\, \lambda^N \mathcal{Z}_N = (1 - \mathcal{Z}^{\mathrm{b}}\mathcal{Z}^{\mathrm{u}})^{-1}\,, \tag{2.17}$$

where the grand-canonical partition functions of a loop and a bound part are given by $\mathcal{Z}^{\mathrm{u}} = \int_0^\infty \mathrm{d}\Omega\, \lambda^\Omega \mathcal{Z}_N^{\mathrm{u}}$ and $\mathcal{Z}^{\mathrm{b}} = \int_0^\infty \mathrm{d}\Upsilon\, \lambda^\Upsilon \mathcal{Z}_\Upsilon^{\mathrm{b}}$. The statistical weight of a bound base pair is given by $w = \exp\chi$ where χ is the absolute value of the binding energy in units of $k_{\mathrm{B}}T$. For simplicity $k_{\mathrm{B}}T \times \chi$ is assumed to be temperature independent and independent of the bound or non-bound status of the neighboring base pairs. Thus we can write

$$\mathcal{Z}^{\mathrm{b}} = \int_0^\infty \mathrm{d}\Upsilon\, (\lambda w)^\Upsilon = -\left[\ln(\lambda w)\right]^{-1}\,, \tag{2.18}$$

which is defined only for $\lambda < w^{-1}$. The form of the canonical loop partition function is taken as

$$\mathcal{Z}_\Omega^{\mathrm{u}} = V\alpha^\Omega/(1+\Omega)^\upsilon\,, \tag{2.19}$$

where V is the fugacity taking into account the loop initiation energy and α is the fugacity of a free segment which is supposed to be independent of the length of the loop. The partition function is inversely weighted by a term proportional to the number of monomers in the loop Ω to the power of υ where υ can be viewed as the return exponent. Consider now a Gaussian chain with Ω monomers with the end-to-end probability distribution given by (2.5). For a loop beginning and ending at the same point in space it follows that $P_\Omega(\boldsymbol{R},\boldsymbol{R}) = \left(\frac{3}{2\pi\Omega a^2}\right)^{3/2} \propto \Omega^{-3/2}$, and hence for an ideal polymer in three dimensions $\upsilon = 3/2$. For non-ideal polymers and other situations the return exponent differs from 3/2, thus we do not limit the discussion to $\upsilon = 3/2$ yet. The grand-canonical partition function of a loop then is

$$\mathcal{Z}^{\mathrm{u}} = V\int_0^\infty \mathrm{d}\Omega\, \frac{(\lambda\alpha)^\Omega}{(1+\Omega)^\upsilon} = \frac{V}{\alpha\lambda}E_\upsilon(\ln[1/\lambda\alpha])\,, \tag{2.20}$$

where the exponential integral function is defined as $E_n(x) = \int_1^\infty \mathrm{d}t\, \exp(-xt)/t^n$. The expectation value of the number of bases in the DNA molecule is given by

$$\langle N\rangle = \lambda\mathcal{Z}_\lambda' = \lambda\frac{\mathcal{Z}^{\mathrm{b}\prime}\mathcal{Z}^{\mathrm{u}} + \mathcal{Z}^{\mathrm{b}}\mathcal{Z}^{\mathrm{u}\prime}}{1-\mathcal{Z}^{\mathrm{b}}\mathcal{Z}^{\mathrm{u}}}\,, \tag{2.21}$$

where dashed functions denote their derivatives with respect to λ, *e.g.* $\mathcal{Z}_\lambda' = \frac{\partial\mathcal{Z}_\lambda}{\partial\lambda}$. For $\lambda < \alpha^{-1}$ which can always be fulfilled, the bound partition function and its derivative are finite, $0 < \mathcal{Z}^{\mathrm{u}}, \mathcal{Z}^{\mathrm{u}\prime} < \infty$. Thus, in the thermodynamic limit, $\langle N\rangle \to \infty$, either due to Eq. (2.21)

$$\mathcal{Z}^{\mathrm{u}}\mathcal{Z}^{\mathrm{b}} = 1 \tag{2.22}$$

or due to Eq. (2.20)

$$\lambda\alpha = 1\,, \tag{2.23}$$

has to hold. The thermodynamic minimization principle states that the phase with the smallest value of the fugacity λ, and accordingly the lowest chemical potential is realized. Inspection of (2.20) shows that we have

$$\text{for } \lambda \to \alpha^{-1}\text{:} \begin{cases} \mathcal{Z}^{\mathrm{u}} \to \infty, \mathcal{Z}^{\mathrm{u}\prime} \to \infty & \text{for } \upsilon \leq 1, \\ \mathcal{Z}^{\mathrm{u}} < \infty, \mathcal{Z}^{\mathrm{u}\prime} \to \infty & \text{for } 1 < \upsilon \leq 2, \text{ and} \\ \mathcal{Z}^{\mathrm{u}} < \infty, \mathcal{Z}^{\mathrm{u}\prime} < \infty & \text{for } 2 < \upsilon. \end{cases} \tag{2.24}$$

Hence, for any υ and large enough w the thermodynamic behavior is determined by Eq. (2.22), but for $\upsilon > 1$ there is a phase transition located at a critical value of w^*, below which ($w < w^*$) Eq. (2.22) can no longer be satisfied and where the thermodynamic limit is obtained by Eq. (2.23). From the expression for the fraction of bound monomers,

$$\frac{\langle \Upsilon \rangle}{\langle N \rangle} = \frac{w}{\langle N \rangle}\frac{\partial \ln \mathcal{Z}_\lambda}{\partial w} = \left(1 + \frac{\mathcal{Z}^{\mathrm{u}\prime}\mathcal{Z}^{\mathrm{b}}}{\mathcal{Z}^{\mathrm{u}}\mathcal{Z}^{\mathrm{b}\prime}}\right)^{-1}\,, \tag{2.25}$$

it is seen that the phase with $w < w^*$ is completely unbound, $\langle \Upsilon \rangle / \langle N \rangle = 0$. In conjunction with Eq. (2.24) we infer that for $\upsilon \leq 1$ the DNA is always bound with a finite fraction of helical segments irrespective of the temperature or conversely the value of w. For $1 < \upsilon \leq 2$ there is a continuous phase transition with the fraction of bound monomers decreasing to zero for $\lambda \to \alpha^{-1}$. For $\upsilon > 2$ the phase transition is of discontinuous type with a jump in the fraction of bound monomers at $\lambda = \alpha^{-1}$ from a finite value to zero.

The binding and unbinding of DNA segments is indeed closely related to polymer adsorption to a flat wall. The height probability distribution function for an ideal polymer in one dimension with a contour length t and starting at height Z_0 reads $P_t(Z; Z_0) = 1/(\sqrt{2\pi t a^2}) \times \exp\left(-[Z - Z_0]^2/2ta^2\right)$, see also Eq. (2.5). This suggests $\upsilon = 1/2$ and an always bound state for an adsorbing polymer in the vicinity of a penetrable wall, *e.g.* a polymer at an interface between immiscible fluids. For the case of an impenetrable wall, as depicted in Fig. 2.1b), the method of images is used to construct the height probability distribution function close to the wall with the boundary condition $P_t^{\mathrm{w}}(Z = 0; Z_0) = 0$, yielding $P_t^{\mathrm{w}}(Z; Z_0) \propto P_t(Z; Z_0) - P_t(Z; -Z_0)$. Expanding for small starting heights Z_0 we get

$$P_t^{\mathrm{w}}(Z; Z_0) = \frac{\sqrt{2} Z Z_0}{\sqrt{\pi t^3} a^3} \exp\left(-\frac{Z^2}{2ta^2}\right)\,, \tag{2.26}$$

confirming the result from Section 2.1 that polymer adsorption to an impenetrable wall is a continuous transition since $1 < \upsilon = 3/2 \leq 2$. The expectation value of the height averaged over all monomers in one loop of length Ω_i starting at $Z_0 = 0$, $\langle Z_{\Omega_i} \rangle$, is given by

$$\langle Z_{\Omega_i} \rangle = \frac{1}{\Omega_i} \int_0^{\Omega_i} \mathrm{d}t\, \frac{\int_0^\infty \mathrm{d}Z\, Z P_t^{\mathrm{w}}(Z;0) P_{\Omega_i - t}^{\mathrm{w}}(Z;0)}{\int_0^\infty \mathrm{d}Z\, P_t^{\mathrm{w}}(Z;0) P_{\Omega_i - t}^{\mathrm{w}}(Z;0)} = \frac{a}{2}\sqrt{\frac{\pi \Omega_i}{2}}\,, \tag{2.27}$$

which shows that the loops perform a rescaled ideal Gaussian random walk in the $\hat{z}$ direction, $\langle Z_{\Omega_i} \rangle \propto \Omega_i^{1/2}$. Thus the mean height of any polymer loop, $\langle Z \rangle$, is obtained via

$$\langle Z \rangle = \frac{a}{2}\sqrt{\frac{\pi}{2}}\frac{\langle \Omega^{1/2} \rangle}{\langle k \rangle} = \frac{a}{2\langle k \rangle}\sqrt{\frac{\pi}{2}}\frac{\mathcal{Z}^{\mathrm{b}}V}{1-\mathcal{Z}^{\mathrm{b}}\mathcal{Z}^{\mathrm{u}}}\int_0^{\infty} \mathrm{d}\Omega\, \frac{(\alpha\lambda)^{\Omega}\,\Omega^{1/2}}{(1+\Omega)^{\upsilon}}\,, \tag{2.28}$$

where the latter expression can be approximately written as $V\int_0^{\infty}\mathrm{d}\Omega\,\frac{(\alpha\lambda)^{\Omega}\Omega^{1/2}}{(1+\Omega)^{\upsilon}} \approx V\int_0^{\infty}\mathrm{d}\Omega\,\frac{(\alpha\lambda)^{\Omega}}{(1+\Omega)^{\upsilon-1/2}} \equiv \mathcal{Z}^{\mathrm{u}}(\upsilon-1/2)$. With the average number of loops,

$$\langle k \rangle = V\frac{\partial \ln \mathcal{Z}_{\lambda}}{\partial V} = \frac{\mathcal{Z}^{\mathrm{b}}\mathcal{Z}^{\mathrm{u}}}{1-\mathcal{Z}^{\mathrm{b}}\mathcal{Z}^{\mathrm{u}}}\,, \tag{2.29}$$

the final result for the average height of the loops is simply

$$\langle Z \rangle = \frac{a}{2}\sqrt{\frac{\pi}{2}}\frac{\mathcal{Z}^{\mathrm{u}}(\upsilon-1/2)}{\mathcal{Z}^{\mathrm{u}}(\upsilon)}\,. \tag{2.30}$$

Other quantities of interest are the mean number of monomers per train, $\langle \Upsilon \rangle/\langle k \rangle$, and the mean number of monomers per loop, $\langle \Omega \rangle/\langle k \rangle$. In the adsorbed regime, we can use Eqs. (2.18) and (2.22) to show that

$$\frac{\langle \Upsilon \rangle}{\langle k \rangle} = \lambda\frac{\mathcal{Z}^{\mathrm{b}\prime}}{\mathcal{Z}^{\mathrm{b}}} = \mathcal{Z}^{\mathrm{b}} = \frac{1}{\mathcal{Z}^{\mathrm{u}}}\,. \tag{2.31}$$

Using the notation introduced for Eq. (2.30), we can write $\lambda\mathcal{Z}^{\mathrm{u}\prime} = V\int_0^{\infty}\mathrm{d}\Omega\,\frac{(\alpha\lambda)^{\Omega}\Omega}{(1+\Omega)^{\upsilon}} \approx V\int_0^{\infty}\mathrm{d}\Omega\,\frac{(\alpha\lambda)^{\Omega}}{(1+\Omega)^{\upsilon-1}} \equiv \mathcal{Z}^{\mathrm{u}}(\upsilon-1)$, and get

$$\frac{\langle \Omega \rangle}{\langle k \rangle} = \lambda\frac{\mathcal{Z}^{\mathrm{u}\prime}}{\mathcal{Z}^{\mathrm{u}}} = \frac{\mathcal{Z}^{\mathrm{u}}(\upsilon-1)}{\mathcal{Z}^{\mathrm{u}}(\upsilon)}\,. \tag{2.32}$$

With the same notation and applying the thermodynamic limit one can simplify Eq. (2.25) and write short-hand for the fraction of adsorbed monomers

$$\frac{\langle \Upsilon \rangle}{\langle N \rangle} = \left(1+\mathcal{Z}^{\mathrm{u}}(\upsilon-1)\right)^{-1}\,. \tag{2.33}$$

As discussed previously, in the adsorbed phase we have $\lambda < \alpha^{-1}$, or in general

$$\lambda = \alpha^{-1}(1-\delta)\,, \tag{2.34}$$

where $0 < \delta < 1$ is a measure for the distance from the phase transition. Using Eq. (2.20) we plot in Fig. 2.2 the rescaled average height of the loops, $\langle Z \rangle/a$ (solid line), the mean number of monomers per loop, $\langle \Omega \rangle/\langle k \rangle$ (dot-dashed line), the mean number of monomers per train, $\langle \Upsilon \rangle/\langle k \rangle$ (dotted line), and the fraction of adsorbed monomers, $\langle \Upsilon \rangle/\langle N \rangle$ (dashed line), in the adsorbed regime as a function of δ. For

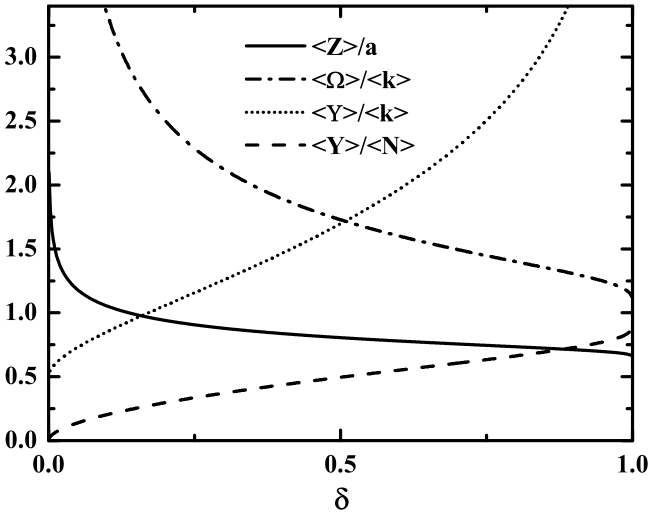

Figure 2.2: Polymer adsorption in the Poland-Scheraga model. Shown is the rescaled average height of the loops, $\langle Z\rangle/a$ (solid line, Eq. (2.30)), the mean number of monomers per loop, $\langle\Omega\rangle/\langle k\rangle$ (dot-dashed line, Eq. (2.32)), the mean number of monomers per train, $\langle\Upsilon\rangle/\langle k\rangle$ (dotted line, Eq. (2.31)), and the fraction of adsorbed monomers, $\langle\Upsilon\rangle/\langle N\rangle$ (dashed line, Eq. (2.33)), in the adsorbed regime. δ measures the distance from the desorption transition ($\delta = 0$) and is defined by Eq. (2.34). For $\langle\Upsilon\rangle/\langle k\rangle$ and $\langle\Upsilon\rangle/\langle N\rangle$ we use $V = 1$ as an exemplary case. $\delta = 0$ corresponds to the adsorption transition where $T = T^*$; $\delta = 1$ corresponds to $T \to 0$; hence only the adsorbed, low-temperature phase is shown.

$\langle\Upsilon\rangle/\langle N\rangle$ and $\langle\Upsilon\rangle/\langle k\rangle$ we use $V = 1$. More intuitively, δ can also be related to the reduced temperature of the system $\tilde{T} = (T - T^*)/T^*$ for a given value of the adsorption energy χ, or conversely to the reduced value of the adsorption energy $\Delta = \chi - \chi^*$ for a given temperature. Again, symbols with asterisks denote their value at the critical adsorption transition. Close to the phase transition in the adsorbed regime we write $w = \exp\chi \approx w^*(1 + \Delta)$ from which follows $\Delta \approx \chi^*\tilde{T}$. Using the thermodynamic limit Eq. (2.22) and an expansion of Eq. (2.20) for small δ, we get for the case of $1 < \upsilon \leq 2$ to leading order in δ

$$\Delta = V\delta^{\upsilon-1}\Gamma(1-\upsilon) + \mathcal{O}(\delta) \,, \tag{2.35}$$

where $\Gamma(x)$ is the Euler Gamma function. As one exemplary case for the adsorption of an ideal polymer at a hard wall ($\upsilon = 3/2$) we mention that via an expansion for small δ the critical exponent for the average fraction of adsorbed monomers turns out to be 1,

$$\langle\Upsilon\rangle / \langle N\rangle \sim \delta^{2-\upsilon} \sim \Delta^{-\frac{\upsilon-2}{\upsilon-1}} = \Delta \,, \tag{2.36}$$

which is strong evidence for the criticality of polymer adsorption and its universality since the result of Section 2.1, Eq. (2.14), is recovered.

Concluding, the Poland-Scheraga model turns out to be a useful method to study Gaussian polymers close to surfaces with a contact adsorption potential as in Eq. (2.18). This makes it possible to unequivocally define tails, trains and loops in a similar fashion as for lattice models [24] and to calculate their properties in the thermodynamic limit.

2.3 Adsorption in Brownian dynamics simulations

There is a long tradition to use BD and Monte Carlo simulations to investigate polymer adsorption. One reason is that exactly treatable models like the Gaussian chain lack certain features of real polymers such as a finite polymer extensibility, excluded volume interactions, semi-flexibility or frozen disorder just to mention a few. Including these properties often means that analytical solutions beyond the mean field level are no longer achievable. Additionally, with BD simulations dynamic properties as well as non-equilibrium effects can be studied. This procedure will be followed in Chapter 4. Here we take a look at the case of equilibrium adsorption in BD simulations.

2.3.1 Brownian dynamics simulation details

The simplified polymer model adopted in our BD simulations consists of N monomer beads interacting with each other via a potential U^{poly} and with a flat wall via a potential U^{surf}, resulting in a total potential of $U = U^{\mathrm{poly}} + U^{\mathrm{surf}}$. For the moment hydrodynamic effects are neglected since close to a solid surface screening makes hydrodynamic interaction short-ranged. Neglecting the inertial term, the position of the ith monomer, $\boldsymbol{R}_i = (X_i, Y_i, Z_i)$, is given by the position Langevin equation

$$\frac{\mathrm{d}\boldsymbol{R}_i}{\mathrm{d}t} = \mu \left[-\boldsymbol{\nabla}_{\boldsymbol{R}_i} U(t) + \boldsymbol{\xi}_i(t)\right] , \tag{2.37}$$

where $\boldsymbol{\xi}_i$ is a vectorial random force satisfying

$$\left\langle \xi_i^p(t) \xi_j^q(t') \right\rangle = 2 k_{\mathrm{B}} T \delta_{ij} \delta_{pq} \delta(t - t')/\mu \, , \tag{2.38}$$

and μ is the bare monomer mobility (p and q denote vector components). A sketch of the model including symbol definitions is shown in Fig. 4.1 on page 62.

The simulations are done via discretizing Eq. (2.37) with a time step Δt and rescaling all length scales by the equilibrium bond length between two monomers, a, leading to $\tilde{\boldsymbol{R}}_i = \boldsymbol{R}_i/a$. The discretized Langevin equation as a function of the discrete time step variable $n = t/\Delta t$ reads

$$\tilde{\boldsymbol{R}}_i(n+1) = \tilde{\boldsymbol{R}}_i(n) + \tilde{\mu} \left[-\boldsymbol{\nabla}_{\tilde{\boldsymbol{R}}_i} \tilde{U}(n) + \sqrt{2/\tilde{\mu}}\, \tilde{\boldsymbol{\xi}}_i(n)\right] , \tag{2.39}$$

where we used the dimensionless potential, $\tilde{U} = U/k_{\mathrm{B}}T$, and the rescaled random force with unity variance, $\langle \tilde{\xi}_i^p(n) \tilde{\xi}_j^q(n') \rangle = \delta_{ij} \delta_{pq} \delta_{nn'}$. The rescaled mobility $\tilde{\mu} = \mu k_{\mathrm{B}} T \Delta t / a^2$ is the diffusion constant in units of the bond length a and time step Δt.

The intramolecular potential $\tilde{U}^{\mathrm{poly}}$ contains two terms,

$$\tilde{U}^{\mathrm{poly}} = \tilde{k}/2 \sum_i \left(\tilde{r}_i - 1\right)^2 + \epsilon \sum_{i<j} \left(\tilde{r}_{ij}^{-12} - 2\tilde{r}_{ij}^{-6}\right) , \tag{2.40}$$

where $\tilde{r}_{ij} = \left|\tilde{\boldsymbol{R}}_j - \tilde{\boldsymbol{R}}_i\right|$ is the rescaled monomer distance and $\tilde{r}_i = \tilde{r}_{i,i+1}$ the distance of nearest neighbors. The first term ensures the chain connectivity by harmonic bonds around the equilibrium length a with a rescaled spring constant $\tilde{k} = 200$, the second is a truncated Lennard-Jones potential with a rescaled parameter $\epsilon = 2$ which is only used for $\tilde{r}_{ij} < 1$ to avoid self-intersection of the chain. Since the spring constant is rather large, our model of a flexible polymer is very closely related to a FJC taking excluded volume into account.

The attractive monomer-surface interaction potential decays exponentially with the distance from the surface,

$$\tilde{U}^{\mathrm{surf}} = -\chi \sum_i \exp\left(-\tilde{\kappa}\tilde{Z}_i\right) , \tag{2.41}$$

where $\tilde{\kappa}^{-1} = \kappa^{-1}/a$ and χ are the rescaled decay length and the rescaled interaction parameter, respectively. For electrostatically driven adsorption, the interaction parameter χ can be written as $\chi = 2\pi\sigma_{\mathrm{surf}}\sigma_{\mathrm{poly}}\ell_{\mathrm{B}}/\kappa a^2 = \sigma_{\mathrm{surf}}\sigma_{\mathrm{poly}}e^2/2\epsilon k_{\mathrm{B}}T\kappa a^2$, where we used the surface charge density measured in units of the elementary charge e per unit area a^2, σ_{surf}, the polymer line charge density measured in units of e and a, σ_{poly}, and the decay length κ^{-1} as the screening length. ℓ_{B} is the Bjerrum length $\ell_{\mathrm{B}} = e^2/4\pi\epsilon k_{\mathrm{B}}T$ where ϵ is the dielectric constant of water. However, in this work we use the exponential potential as a generic form to study short-ranged surface attraction and have in mind also hydrophobic or van-der-Waals interactions. To make it very short-ranged, we use $\tilde{\kappa}^{-1} = 1/2$. We also include a hard wall interaction of the monomers at the wall-liquid boundary, *i.e.* $\tilde{U}^{\mathrm{surf}}(\tilde{Z}_i < 0) = \infty$.

We use a rescaled time step of $\tilde{\mu} = 10^{-4}$ and simulate for at least $n \geq 10^8$ simulation steps. The first 20 % of these steps are disregarded for equilibration. Every 1000 steps the configuration is recorded. Data are obtained by block averaging, statistical errors are obtained from the standard deviation of the block means and are only shown when larger than the symbol size. Simulations are performed for polymers of different length ($1 \leq N \leq 512$) and for different values of the adsorption strength ($10^{-4} \leq \chi \leq 100$).

2.3.2 Finite size effects and timescales in the adsorption transition

The simulations are started with an adsorbed ($\tilde{Z}_i = 0$, for all $i \in \{1 \ldots N\}$) and linearly aligned polymer. In thermodynamic equilibrium, *any* polymer of *finite* length will due to entropic reasons be driven into the semi-infinite half-space, no matter how strong the adsorption strength is. On the other hand, a dynamic simulation of necessarily finite duration only probes a small part of the configurational space. It turns out that by carefully choosing the polymer length and the simulation duration, information about polymer adsorption in the asymptotic limit of an infinitely long polymer can be gained, as we discuss now. On the scaling level we approximate the adsorption kinetics of a polymer consisting of N monomers in the surface potential Eq. (2.41) by a Kramers escape problem [57] from a simplified potential characterized by a constant force $-N\chi\tilde{\kappa}$ and finite range $\tilde{\kappa}^{-1}$. In this simplified case, the Kramers escape time turns out to be $\tau_{\mathrm{K}} = 2\tau_{\mathrm{D}}(\exp(\alpha) - \alpha - 1)/\alpha^2$, where $\tau_{\mathrm{D}} = N\kappa^{-2}/2\mu k_{\mathrm{B}}T$ is the time needed for diffusing a distance κ^{-1} assuming Rouse dynamics and $\alpha = N\chi$ the dimensionless work along the escape coordinate. The ratio of $\tau_{\mathrm{K}}/\tau_{\mathrm{D}}$ increases exponentially with the number of monomers and the potential strength, which means that escape from the adsorption potential requires exponentially long simulation time. This opens up a finite time window in the domain $\tau_{\mathrm{D}} < t < \tau_{\mathrm{K}}$ within which a polymer of finite length has enough time to diffuse over the relevant length scale set by the potential range κ^{-1}, but at the same time stays adsorbed in the potential. Clearly, this time window widens with increasing monomer number N, or, conversely, shrinks for too short polymers; in the simulations we made sure to stay inside this window. Note that this calculation neglects the conformational polymer entropy since we model the escape barrier by the internal energy and not the free energy, and thus the argument only serves as a rough guide. Another important timescale is the relaxation time of the longest normal mode, which in the free-draining case or Rouse dynamics is given by $\tau_{\mathrm{R}} = N^2a^2/3\pi^2\mu k_{\mathrm{B}}T$. The duration t of our simulations satisfies the more stringent condition $t > \tau_{\mathrm{R}}$ for all polymer lengths, though we stress that the actual relaxation time in the adsorbed state, τ_{D}, is much shorter than τ_{R}.

The transition between the adsorbed and desorbed state can be quantified with different observables, *e.g.* the adsorption potential energy [44], the polymer mean height [47], the number of adsorbed monomers [50], or the radius of gyration perpendicular to the surface [51]. In Fig. 2.3 we plot the mean adsorption potential per monomer, $\langle -\tilde{U}^{\mathrm{surf}}\rangle/N$, calculated from Eq. (2.41), and the mean inverse height of the polymer from the surface, $\langle \tilde{h}^{-1}\rangle = \langle 1/(\sum_{i=1}^{N} \tilde{Z}_i/N)\rangle$, for a 128mer as a function of χ. The number of simulation steps is $n = t/\Delta t = 10^8$. In the thermodynamic limit $N \to \infty$ both observables are expected to go to zero in a continuous fashion at the adsorption transition χ^*, as predicted in Sections 2.1 and 2.2, cf. Eqs. (2.14), (2.12), and (2.15). However, as rationalized above, it is impossible to pinpoint the adsorption transition with a finite-duration simulation of a finite-length polymer. We illustrate this in Fig. 2.4 where we plot the time evolution of $-\tilde{U}^{\mathrm{surf}}/N$ for an extended simulation consisting of $n = t/\Delta t = 6 \times 10^8$ simulation steps for $\chi = 0.94$ which is close to the estimated critical adsorption strength. During a process of "equilibration" within $0 < t < \tau_{\mathrm{R}}$ the average adsorption energy decreases and reaches a mean value of about $-\langle\tilde{U}^{\mathrm{surf}}\rangle/N \approx 0.08$ for an intermittent time range. After $t \approx 70\tau_{\mathrm{R}}$ the polymer desorbs from the surface and freely diffuses in the half space. This shows the general problem in determining the critical adsorption strength *unequivocally* since irreversible desorption from the surface will happen eventually in the long-time limit for any adsorption strength.

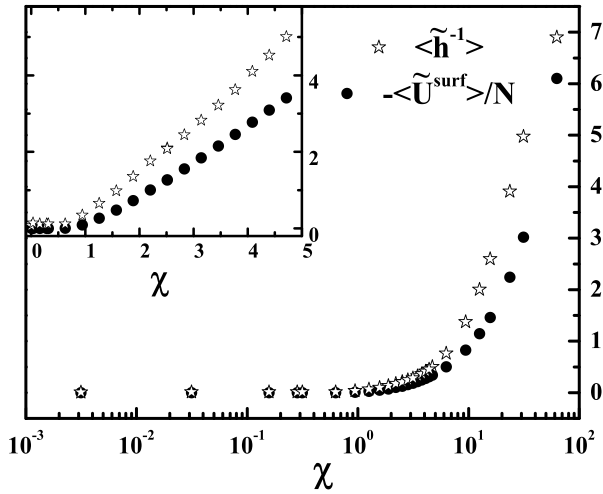

Figure 2.3: Mean inverse height $\langle\tilde{h}^{-1}\rangle$ (stars) and mean adsorption potential $\langle-\tilde{U}^{\rm surf}\rangle/N$ (filled circles) for a 128mer as functions of the surface interaction parameter χ without pulling force. Inset shows an excerpt on a linear scaled axis.

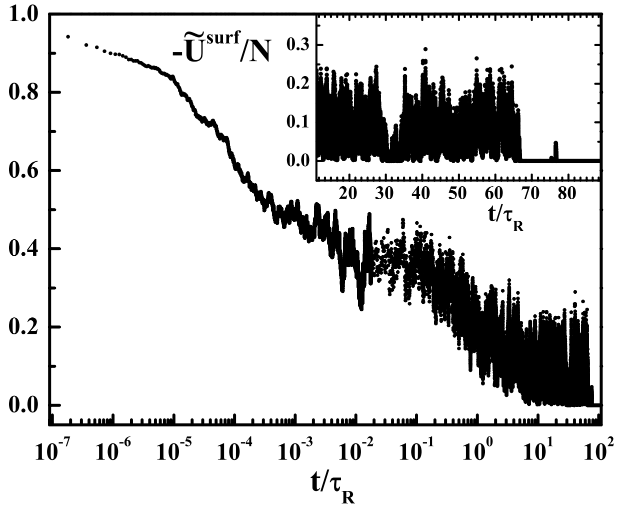

Figure 2.4: Adsorption potential $-\tilde{U}^{\rm surf}/N$ for a 128mer close to the desorption transition (at $\chi = 0.94$) as a function of time in units of the Rouse relaxation time $t/\tau_{\rm R}$. Inset shows the late desorption event on a linear scaled axis.

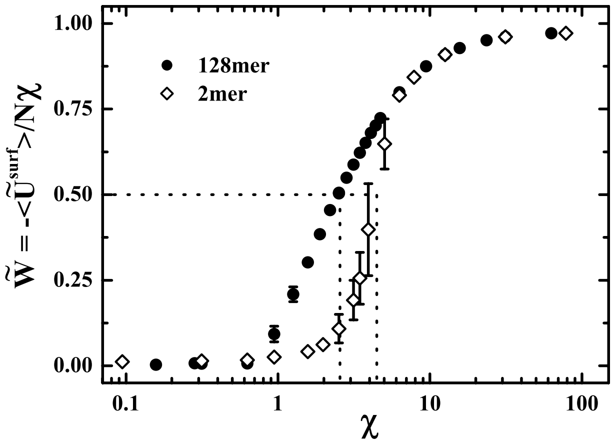

Figure 2.5: Mean normalized adsorption energy $\tilde{W} = -\langle \tilde{U}^{\mathrm{surf}} \rangle / N\chi$ for a dimer (diamonds) and a 128mer (circles) as a function of the surface interaction parameter χ. The simulation time is $t/\tau_{\mathrm{R}} \approx 7.4 \cdot 10^5$ and 18.1, respectively. The lines depict the definition of the overcritical adsorption strength, $\chi^{\mathrm{ocrit}} \equiv \chi(\tilde{W} = 1/2)$, which is found to be $\chi^{\mathrm{ocrit}} = 4.46$ and 2.55 for $N = 2$ and 128, respectively.

In Fig. 2.5 we plot the mean adsorption potential per monomer normalized by the adsorption strength, $\tilde{W} = -\langle \tilde{U}^{\mathrm{surf}} \rangle / N\chi$, for a 128mer and a dimer, obtained from simulations over $n = t/\Delta t = 10^8$ (128mer) and $n = 10^9$ (dimer) iteration steps. This is a function between 0 (desorbed regime) and 1 (zero temperature adsorbed ground state). Close to the desorption transition at χ^*, $\tilde{W}$ scales linear in $\log(\chi - \chi^*)$, *i.e.* for small $\Delta = \chi - \chi^*$ the results for a Gaussian polymer, Eqs. (2.14) and (2.36) are recovered.

To circumvent the problem of irreversible polymer desorption close to the critical transition, we define as an 'overcritical' adsorption strength the value of χ, at which the mean normalized adsorption potential is half its maximum value, *i.e.* $\chi^{\mathrm{ocrit}} \equiv \chi(\tilde{W} = 1/2)$. This quantity can be determined with high precision since the escape time τ_K at these rather elevated adsorption strengths is much higher than the relaxation time τ_D and it is easy to perform a simulation in the intermediate time window $\tau_D < t < \tau_K$. We carefully checked that the use of this heuristic overcritical parameter does not influence our main conclusion in an essential way. The overcritical values of the adsorption strength are presented in Fig. 2.6 for polymers of different length. The results can be fitted linearly in $1/N$ and give the asymptotic result $\chi^{\mathrm{ocrit}}(N \to \infty) = 2.5 \pm 0.15$. For the longest polymers a fit linear in $1/N^{1/2}$ works equally well (shown in the inset of Fig. 2.6), yielding the equivalent result $\chi^{\mathrm{ocrit}}(N \to \infty) = 2.4 \pm 0.1$, in agreement with previous arguments [58]. The precise finite-length scaling behavior is disputed in the literature, cf. Ref. [59] and references therein, but is relevant to our results neither in the equilibrium nor the non-equilibrium case.

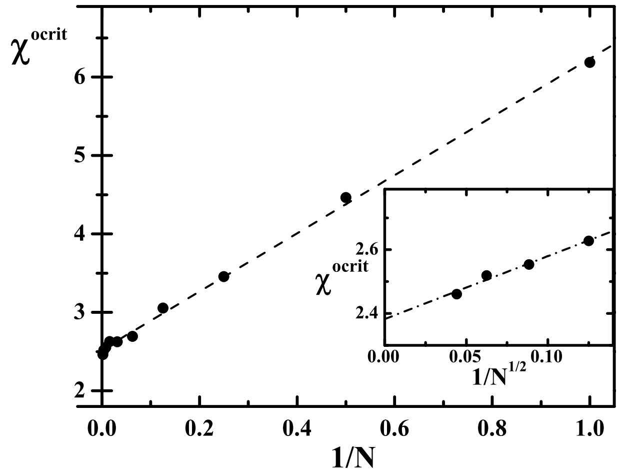

Figure 2.6: Overcritical adsorption parameter $\chi^{\text{ocrit}} \equiv \chi(\tilde{W} = 1/2)$ as a function of the inverse length $1/N$. A linear fit to the data is also shown and gives $\chi^{\text{ocrit}}(N \to \infty) = 2.5{\pm}0.15$. The inset shows the overcritical adsorption parameter as a function of $N^{-1/2}$ where the fit gives $\chi^{\text{ocrit}}(N \to \infty) = 2.4 \pm 0.1$.

Summarizing, we have demonstrated that the careful use of BD simulations of necessarily finite polymer length and simulation time *does* provide information on the adsorption transition which itself is only well-defined in the thermodynamic limit of infinite polymer length. The scaling behavior of some observables is preserved as compared to predictions of Gaussian chain models, see Sections 2.1 and 2.2.

2.4 Strong and weak adsorption limits of ideal and non-ideal polymers

As described in Section 1.1, AFM technology can be used to partly desorb a polymer from a surface and measure the force needed to do that, cf. Fig. 1.2. The conformation of a partly adsorbed polymer which is being held with one end at some height D in solution depends on the adsorption strength with which the polymer is (reversibly) bound to the surface and on its intrinsic stiffness. In the case of strong adsorption the force needed to desorb the polymer is large compared to thermal forces. For weak enough adsorption, thermal fluctuations of the free chain need to be taken into consideration.

For simplicity we assume that the polymer consists of a single train with Υ monomers adsorbed to the surface at $Z = 0$ and a polymer part in solution having Ω monomers, see also Fig. 2.7. The total number of monomers is given by $N = \Upsilon + \Omega$. The position of the free end of the polymer is assumed to be perfectly controlled and given by the vertical distance $Z = D$ of the ‘first’ monomer with respect to surface. The stretching free energy A_{stretch} of a polymer made of Ω monomers and

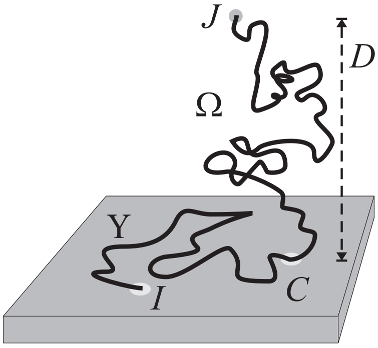

Figure 2.7: Schematic geometry of a single polymer adsorbed with a single train to a surface. The number of monomers in the train (from the end of the chain I to the contact point C) is Υ, the number of monomers in the tail (between C and the start of the chain J) is $\Omega = N - \Upsilon$. The height of the first monomer is denoted by D.

fixed with its end points to a distance D can in general be written as an integral over a stretching force, F_{stretch},

$$A_{\text{stretch}}(\Omega, D) = \int_0^D \mathrm{d}Z\, F_{\text{stretch}}(\Omega, Z)\,. \tag{2.42}$$

Similarly, one can define a free energy of adsorption A_{ads} which in general is a function of all monomer positions. When the attractive interaction is short ranged, *e.g.* by screening of electrostatic attraction between monomers and the surface, the free energy of adsorption can be written as a contact potential,

$$A_{\text{ads}}(\Upsilon) = -\omega a k_{\text{B}} T \Upsilon\,, \tag{2.43}$$

where ω is the adsorption free energy per unit length and $k_{\text{B}}T$. The total free energy of the system is given by the sum of the terms, $A_{\text{tot}} = A_{\text{stretch}}(\Omega, D) + A_{\text{ads}}(N - \Omega)$. The equilibrium number of monomers in the desorbed part, Ω^*, is determined by

$$\left.\frac{\partial A_{\text{tot}}(\Omega, D)}{\partial \Omega}\right|_{\Omega=\Omega^*} \overset{!}{=} 0\,, \tag{2.44}$$

which in the case of the contact potential (2.43) gives $\omega a k_{\text{B}} T + \int_0^D \mathrm{d}Z\, F_{\text{ads}}(\Omega^*, Z) = 0$. The total force needed for desorbing Ω monomers, F_{tot}, is given by

$$\begin{aligned} F_{\text{tot}}(D) &= \left.\frac{\mathrm{d}A_{\text{tot}}(\Omega, D')}{\mathrm{d}D'}\right|_{\Omega=\Omega^*, D'=D} \\ &= \left(\frac{\partial A_{\text{tot}}(\Omega, D')}{\partial D'} + \frac{\partial A_{\text{tot}}(\Omega, D')}{\partial \Omega}\frac{\partial \Omega}{\partial D'}\right)_{\Omega=\Omega^*, D'=D}\,, \end{aligned} \tag{2.45}$$

where the second term vanishes by definition, see Eq. (2.44). For a contact potential, *i.e.* if and only if $\partial A_{\mathrm{ads}}/\partial D = 0$, the total desorption force is solely given by the force needed for stretching a polymer of Ω^* monomers to length D,

$$F_{\mathrm{tot}}(D) = \left. \frac{\partial A_{\mathrm{stretch}}(\Omega^*, D')}{\partial D'} \right|_{D'=D} . \tag{2.46}$$

In all other cases one has possibly other contributions in addition to the stretching term. These additional terms can be relevant for long-ranged attractive or repulsive interactions between the surface and the monomers or for inhomogeneous solvent properties due to the presence of the wall such as ion distributions at a wall. In the following we assume Eqs. (2.43) and (2.46) to be valid. Eq. (2.46) suggests that for low adsorption energy, *i.e.* $\omega a < k_{\mathrm{B}}T$, an ideal elastic response of the desorbed polymer strand can be assumed since this is the elastic behavior of any polymer chain in the small force limit. Using the free energy of an ideal Gaussian chain, $A_{\mathrm{stretch}}(\Omega, D) = 3k_{\mathrm{B}}TD^2/2\Omega a^2$, the equilibrium number of monomers of the desorbed chain becomes $\Omega^* = \sqrt{3/2\omega a}\, D/a$. Thus the desorption force is independent of the height D and proportional to the square root of the adsorption energy,

$$F_{\mathrm{tot}}/k_{\mathrm{B}}T = \sqrt{6\omega/a}\,, \tag{2.47}$$

as suggested earlier [52]. In the opposite limit of a very stiff chain, a rod, the number of monomers in the desorbed strand is fixed as $\Omega^* = \Omega = D/a$, and hence the force is again independent of D and shows a plateau value equal to the adsorption free energy per unit length,

$$F_{\mathrm{tot}}/k_{\mathrm{B}}T = \omega\,. \tag{2.48}$$

This result is obtained for stiff rods, *e.g.* due to the electrostatic stiffness of polyelectrolytes [21, 60], but also for strong adsorption, $\omega a \gg 1$, in which high forces are necessary to desorb the polymer. As an exemplary case, this is demonstrated using the mean extension of a freely jointed chain (FJC) stretched by a large force, and valid for $D \to a\Omega$. Here, the mean extension reads $D = a\Omega\,(1 - k_{\mathrm{B}}T/aF_{\mathrm{stretch}})$. Integration yields the stretching free energy, and the equilibrium condition on the number of desorbed monomers is obtained as

$$0 \overset{!}{=} \omega - \frac{D/a}{\Omega^* - D/a} - \ln\left(1 - D/a\Omega^*\right) . \tag{2.49}$$

In the limit of $D \to a\Omega^*$ we get $\Omega^* = (1/\omega a + 1)\, D/a$. Reinserting this expression into the stretching law yields

$$F_{\mathrm{tot}}/k_{\mathrm{B}}T = (1 + 1/\omega a)\,\omega\,, \tag{2.50}$$

which is the previously known result with a small thermal correction. Higher order correction terms can be obtained by expanding $q = (\omega a - \ln(1 - D/a\Omega^*))\,(1 - D/a\Omega^*)$ in $0 \overset{!}{=} q - D/a\Omega^*$ around its minimum with respect to Ω^*. To put in some numbers, for AFM experiments desorption forces between tens and hundreds of piconewtons, say 40 pN, are reported [61], which is also close to the detection limit of this technique [62]. For synthetic polymers and also many of the more flexible biopolymers the monomer diameter or Kuhn length is in the range of $a = 1\,\mathrm{nm}$. This implies adsorption free energies of the order of $\omega a k_{\mathrm{B}} T \approx 40\,\mathrm{pN\,nm} \approx 10\,k_{\mathrm{B}}T$. Hence, for AFM experiments one is typically in the high-force regime and Eq. (2.48) is valid within 10 %. The opposite regime with $\omega a \lesssim 1$ which can be realized *e.g.* in the case of electrostatically driven adsorption with surfaces of sufficiently low charge density, currently cannot be probed using AFM force spectroscopy. However, the better resolution limit of optical and magnetic tweezers would in principal allow this regime to be investigated.

Chapter 3

Friction of single polymers on solid surfaces

Under non-equilibrium conditions it is often crucial to understand the dissipative mechanisms governing the energy fluxes in the system. Numerous studies exist on the rheology of polymers, ranging from dilute solutions over melts to polymer networks [63–66]. In the area of tribology, *i.e.* friction at solid surfaces, theoretical studies conducted during the last fifty years involving polymers or low molecular weight substances have mainly focused on hydrodynamic and elasto-hydrodynamic lubrication, boundary lubrication, and friction of small adsorbates on surfaces [67–69]. Extensive progress has also been achieved in the understanding of thin polymer films and polymer brushes [10, 69]. On the contrary, much less is known about the sliding friction of polymers on solid surfaces in the dilute or single polymer regime. Both experimental [70–77] and theoretical studies [50, 78–86] are rare. Related topics such as the friction of polymers embedded in membranes [87] and of polymers driven on surfaces with geometric obstacles, cf. references in Ref. [76], are not covered here.

In this chapter we extend these studies by proposing a model how to measure single polymer friction by AFM force spectroscopy, Section 3.1, by a discussion of a microscopic Frenkel-Kontorova type model on the origin of polymer friction, Section 3.2, and by a molecular dynamics (MD) study pointing out fundamental differences between polymer friction on hydrophobic and hydrophilic surfaces, Section 3.3.

3.1 Pulling on adsorbed polymers with the AFM

As mentioned in the previous chapters, single polymer experiments using AFM force spectroscopy have nowadays become a reliable tool to probe polymer-surface interactions, cf. Ref. [61] for a recent review, and Refs. [88, 89].

Depending on the adsorption strength between the polymer and the substrate, AFM single polymer studies split into two classes: In the first, the applied forces are relatively weak so that the attachment on the cantilever tip and on the substrate is irreversible up to a certain maximal force and over the typical experimental timescales; in this case the measured distance-force traces contain information on the polymer that is being stretched and can be used to extract the polymer elasticity by comparison with molecular models [90, 91]. In the second class, the applied force is strong enough to detach the polymer from the substrate. In this case, the measured force-distance relation contains information about the strength of the surface-polymer interaction and about the nanoscopic friction effects at the substrate. In fact, assuming that the polymer glides very easily over the surface and surface friction can be neglected, plateau forces are measured the heights of which correspond to the adsorption free energy per unit length, cf. Section 2.4 and Ref. [61]. In the presence of finite surface-polymer friction, the force-distance curves exhibit more complex behavior.

In the interpretation of force-distance curves it is often implicitly assumed that the polymer is vertically attached between the cantilever tip and the surface. This is not necessarily true, and here we point out the consequences of a non-zero attachment angle ϕ as defined schematically in Fig. 3.1. In the case of *irreversible* attachment between the polymer and the substrate, where the polymer-substrate contact point is immobile, the angle ϕ is fixed for a given vertical distance between the polymer-substrate and polymer-cantilever contact points and determined by their lateral distance. This distance is typically not controlled in experiments, but the resulting force-distance curve decisively depends on this angle. In the case of *reversible* attachment between the polymer and the substrate, the resultant behavior depends crucially on the surface friction coefficient of the polymer: For very large friction coefficient, the polymer is peeled off from the substrate segment by segment but does not slide; here the angle is dictated by geometric considerations and changes as the polymer is peeled from the surface. Force-distance curves in this case depend sensitively on the lateral surface configuration of the polymer. For small friction coefficient or, equivalently, for small pulling rates, on the other hand, the polymer portion in contact with the surface is sliding over the surface and the angle adjusts according to a balance of friction and adsorption forces at the contact point. All these geometric considerations have a bearing on the force-distance curves. Proper analysis of the non-equilibrium features of the force curves allows to extract friction coefficients of single polymers on surfaces and thus an important parameter characterizing the nano-tribology of adsorbed polymers.

3.1.1 Fixed contact point

We first consider a polymer attached to the surface at some fixed contact point along the polymer contour length. Experimentally, this can be achieved by covalent bonding between reactive surface groups and polymer monomers [91]. The schematic geometry is given in Fig. 3.1a), where the extension of the polymer stretched between the contact point C and the cantilever tip is denoted by R, and its lateral and vertical components by R_x and R_z, respectively. Clearly, $R^2 = R_x^2 + R_z^2$. We denote the elastic free energy of the polymer in units of $k_\mathrm{B}T$ by $\tilde{A}_\mathrm{stretch}(R)$, which

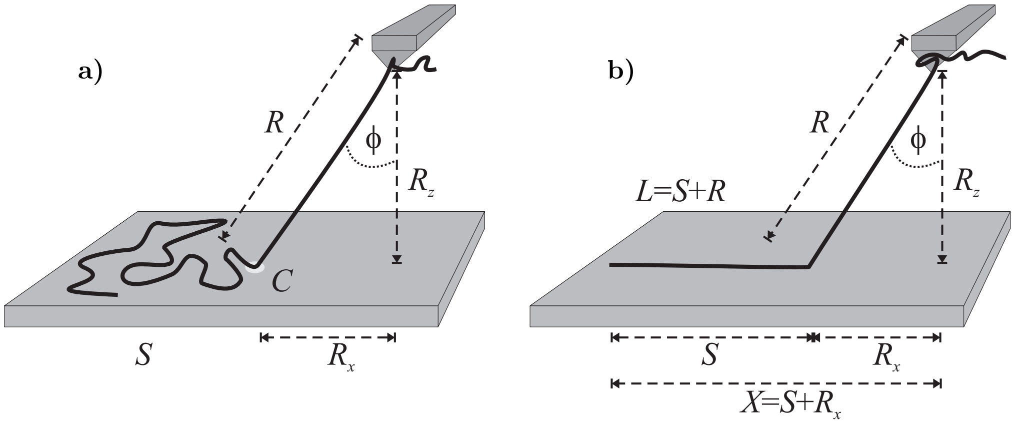

Figure 3.1: Schematic geometry of a single polymer experiment with the AFM. The polymer is bound between a planar surface and the cantilever tip. **a)** Tilted geometry with the adsorbed polymer strand exhibiting a self-similar, crumpled conformation, **b)** idealized geometry where the adsorbed polymer strand is linearly stretched and aligned in parallel with the detached polymer section.

contains entropic as well as energetic contributions due to the deformation of bonds. We neglect the coupling to the probing device, as is justified for sufficiently stiff cantilevers or optical traps [92]. In the presence of an external force F_z acting along the vertical direction, the total free energy in units of k_BT, $\tilde{A}_{\text{tot}}$ becomes

$$\tilde{A}_{\text{tot}} = \tilde{A}_{\text{stretch}}(R) - R_z F_z/k_BT = \tilde{A}_{\text{stretch}}(\sqrt{R_x^2 + R_z^2}) - R_z F_z/k_BT\,. \tag{3.1}$$

The equilibrium extension of the polymer follows from the minimization of the free energy, $\partial\tilde{A}_{\text{tot}}/\partial R_z = 0$, leading to

$$\frac{F_z}{k_BT} = \frac{\tilde{A}'_{\text{stretch}}(R_z\alpha)}{\alpha}\,, \tag{3.2}$$

where $\tilde{A}'_{\text{stretch}}(x) = \partial\tilde{A}_{\text{stretch}}(x)/\partial x$ is the derivative of the elastic polymer energy. As a measure of the chain orientation we define the geometric factor

$$\alpha = 1/\cos\phi = \sqrt{1 + R_x^2/R_z^2} = (1 - R_x^2/R^2)^{-1/2}\,. \tag{3.3}$$

For perfect vertical alignment one has $\alpha = 1$, for a slanted chain one finds $\alpha > 1$. For small stretching forces, any polymer behaves like a Gaussian polymer, *i.e.* like a harmonic entropic spring with a spring constant of

$$K = 3k_BT/R_0^2\,, \tag{3.4}$$

where R_0^2 is the mean-squared end-to-end radius of the unperturbed chain. The elastic free energy reads $\tilde{A}_{\text{stretch}}(x) = Kx^2/2$ and thus $\tilde{A}'_{\text{stretch}}(x) = Kx$. In this case, the geometric factors in Eq. (3.2) exactly cancel and the force-distance relation becomes independent of the chain orientation, $F_z/k_\mathrm{B}T = KR_z$. This cancellation only occurs for a harmonic elastic free energy; in general, a non-trivial dependence arises. For the case of a FJC, characterized by a bond length a and contour length R_L, the elastic force at large stretching reads $\tilde{A}'_\mathrm{stretch}(x) = (1/a)(1 - x/R_L)^{-1}$ [93]. Insertion into Eq. (3.2) yields $\alpha a F_z/k_\mathrm{B}T = (1 - \alpha R_z/R_L)^{-1}$. For a worm-like chain characterized by a persistence length $\ell \approx a/2$, the force in the large-stretching limit is given by $\tilde{A}'_\mathrm{stretch}(x) = 1/(4\ell)(1 - x/R_L)^{-2}$ [93]. The force-distance relation becomes $4\alpha\ell F_z/k_\mathrm{B}T = (1 - \alpha R_z/R_L)^{-2}$. In both cases, the geometric factor α can be interpreted as renormalizing either the bond length a or persistence length ℓ, and the chain contour length R_L. To get an estimate for the typical values of α, we assume the chain to perform a random walk on the surface prior to pick-up by the cantilever, characterized by a swelling exponent ν. Further assuming that the chain extension R approximately equals the contour length R_L of the stretched segment, $R \approx R_L$, we can write $R_x \simeq a(R/a)^\nu$ and thus obtain $\alpha = (1 - (a/R)^{2-2\nu})^{-1/2} \approx 1 + (a/R)^{2-2\nu}/2$. For a self-avoiding walk on the surface, one has $\nu = 3/4$ and thus $\alpha \approx 1 + (a/R)^{1/2}/2$. For a ds-DNA chain with Kuhn length $a = 100\,\mathrm{nm}$ and total length $R = 10\,\mu\mathrm{m}$, the geometric factor evaluates to $\alpha \approx 1.05$, and thus leads to a substantial variation in fitted values for the persistence length and the chain length. The effect drops with increasing polymer length and decreasing Kuhn length and is in fact negligible in many practical cases. On the other hand, the renormalized force-distance relation Eq. (3.2) can be directly checked by AFM experiments with lateral position resolution.

3.1.2 The sticky case

We now turn to the case where the adsorption of the polymer on the substrate is reversible and thus the contact point can move via de- or adsorption. For simplicity, we assume that the adsorption free energy per monomer satisfies $\omega a \gg 1$ where ω is the adsorption free energy per $k_\mathrm{B}T$ and unit length. This implies that we are in the strong adsorption regime and the polymer forms a flat quasi-two-dimensional layer on the surface [35]. The total free energy of the adsorbed polymer strand of contour length S is

$$\tilde{A} = -\omega S\,. \tag{3.5}$$

As rationalized in Section 2.4 we neglect elastic deformations of the desorbed polymer strand which is assumed to be fully stretched to its contour length, *i.e.* $R = R_L$, thus preventing monomer-monomer contacts. To highlight connections to Chapter 2, note that for the inextensible, stretched polymer considered here we have $L = Na$, $S = \Upsilon a$, and $R = \Omega a$. Note also the resemblance between the adsorption free energy for a monomer, ωa, and the adsorption (internal) energy per monomer χ.

We first consider infinite friction of the polymer at the surface: the polymer will thus stick on the surface and a sufficiently strong force will peel the polymer off from the surface. As the contact point moves over the surface, what is the resultant vertical force on the cantilever? The initial geometry is specified by arbitrary values

S_0, R_0, R_{z0}, and R_{x0}. We define the polymer contour length that has been peeled off as $P \equiv S_0 - S = R - R_0$, and parameterize all other variables by P. Again assuming that the adsorbed polymer shows a self-similar lateral distribution function, we find

$$R_x^2(P) \simeq R_{x0}^2 + a^2(P/a)^{2\nu} \,. \tag{3.6}$$

The vertical force acting on the cantilever tip can be calculated from Eq. (3.5) as

$$\frac{F_z}{k_\mathrm{B}T} = \frac{\partial \tilde{A}}{\partial R_z} = \frac{\partial \tilde{A}}{\partial P}\frac{\partial P}{\partial R_z} = \omega \frac{\partial P}{\partial R_z} \,, \tag{3.7}$$

where we used $S = S_0 - P$. From Eq. (3.6) and $R^2(P) = R_x^2(P) + R_z^2(P)$ it follows that

$$\frac{\partial R_z(P)}{\partial P} = \frac{R_0 + P - \nu a(P/a)^{2\nu-1}}{R_z} = \frac{R_0 + P - \nu a(P/a)^{2\nu-1}}{\sqrt{(R_0+P)^2 - R_{x0}^2 - a^2(P/a)^{2\nu}}} \,. \tag{3.8}$$

For a crumpled polymer, characterized by $\nu < 1$, and for a large peeling length $P \to \infty$, the above relation crosses over to $\partial R_z/\partial P \simeq 1$. The vertical force thus reaches a finite plateau value $F_z/k_\mathrm{B}T = \omega$. On the contrary, for a polymer which is adsorbed straight on the substrate, characterized by $\nu = 1$, one has $\partial R_z(P)/\partial P = R_0/R_z$, and thus

$$F_z/k_\mathrm{B}T = \omega R_z/R_0 \tag{3.9}$$

implying that in this case the force increases linearly with the vertical distance.

3.1.3 The slippery case

We now assume a finite polymer-surface friction coefficient so that sliding of the polymer on the substrate is possible when the cantilever is moved either vertically or horizontally. On the cantilever tip the polymer is supposed to stick. When the polymer follows the cantilever motion and glides over the surface, friction forces lead to partial alignment; we therefore simplify the discussion by assuming the polymer to be completely stretched on the surface, as shown in Fig. 3.1b. In experiments, this can be achieved by prior lateral AFM pulling. We define S and R as the contour lengths of the adsorbed and desorbed polymer parts, while $L = S + R$ is the total contour length. The end-point position of the polymer relative to the tip is denoted as $X = S + R_x$. The geometry is fully determined by two length scales, which we choose to be the end-point position X and the cantilever height R_z. The total friction force is supposed to be proportional to the sliding velocity, $\dot{X} = dX/dt$, and the length of the adsorbed part S, and acts parallel to the sliding direction,

$$\frac{F_x^\mathrm{fric}}{k_\mathrm{B}T} = \dot{X} S \zeta = \dot{X} \frac{L^2 - X^2 - R_z^2}{2(L-X)} \zeta \,. \tag{3.10}$$

Here, ζ is the sliding friction coefficient per unit length and $k_\mathrm{B}T$. It depends on all polymer and surface characteristics and is in addition influenced by pH, ionic strength, etc. Throughout Section 3.1 it is assumed to be independent of the adsorption strength ω and the pulling velocity. The friction force is balanced by the horizontal component of the adsorption force, which we associate with the spatial derivative of the adsorption energy Eq. (3.5). We neglect any dependence of the adsorption energy on the gliding velocity and note that Eq. (3.5) in the present non-equilibrium context is not a free energy but rather corresponds to the non-dissipative contribution to the work of desorption. It follows that

$$\frac{F_x^{\mathrm{ads}}}{k_{\mathrm{B}}T} = -\left(\frac{\partial \tilde{A}}{\partial X}\right)_{R_z} = \frac{\omega}{2}\frac{L^2 + X^2 - 2LX - R_z^2}{(L-X)^2} = \omega\frac{R_x}{R_x - R}\,. \tag{3.11}$$

Equating the friction and the adsorption force yields a differential equation for the polymer geometry

$$\dot{\tilde{X}} = \frac{d\tilde{X}}{d\tilde{t}} = \tilde{\omega}\frac{1 + \tilde{X}^2 - 2\tilde{X} - \tilde{R}_z^2}{(1-\tilde{X})(1-\tilde{X}^2-\tilde{R}_z^2)}\,, \tag{3.12}$$

where we have rescaled all lengths by the total contour length according to $\tilde{R}_z = R_z/L$ and $\tilde{X} = X/L$, and introduced the characteristic timescale $\tilde{t} = t/(L^3\zeta)$ and adsorption energy $\tilde{\omega} = \omega L$. In deriving Eq. (3.12) we implicitly assume microscopic relaxation processes such as molecular bending or stretching, as considered in Ref. [94], to equilibrate on much faster timescales than the global polymer geometry. The two poles in Eq. (3.12) correspond to the asymptotic limits of complete adsorption ($X = L$) and complete desorption ($L^2 = X^2 + R_z^2$). The force acting in the vertical direction, which is the force measured by the AFM, is

$$\frac{F_z}{k_{\mathrm{B}}T} = \left(\frac{\partial \tilde{A}}{\partial R_z}\right)_X = \omega\frac{\tilde{R}_z}{1-\tilde{X}} = \omega\frac{R_z}{R-R_x} = -\frac{R_z}{R_x}\frac{F_x}{k_{\mathrm{B}}T}\,, \tag{3.13}$$

where the latter relation is equivalent to the observation that a flexible string can only support a force along the string contour.

In a typical single molecule force spectroscopic experiment the AFM $\hat{z}$ piezo element is moved with a constant velocity V_z. The temporal change in the tip displacement is given by $V_z\,(k_{\mathrm{c}}/F_z'(R_z)+1)^{-1}$ where k_{c} is the cantilever bending constant, and $F_z'(x) = \partial F(x)/\partial x$ the curvature of the polymer interaction potential. For typical potential landscapes and typical cantilever bending constants, $(k_{\mathrm{c}}/F_z'(R_z)+1)^{-1} \ll 1$. We therefore can consider the velocity of the cantilever tip to be constant and equal to the cantilever driving velocity, and hence write

$$R_z = V_z t + R_{z0}\,. \tag{3.14}$$

The differential equation derived from the balance between the friction and the adsorption force, Eq. (3.12), is still valid if Eq. (3.14) is inserted. It proves useful to rewrite the differential equation slightly,

$$\frac{\mathrm{d}\tilde{X}}{\mathrm{d}\tilde{R}_z} = \frac{\mathrm{d}X}{\mathrm{d}t}\frac{\mathrm{d}t}{\mathrm{d}R_z} = \frac{\dot{X}}{V_z} = \gamma_z^{-1}\frac{1 + \tilde{X}^2 - 2\tilde{X} - \tilde{R}_z^2}{(1-\tilde{X})(1-\tilde{X}^2-\tilde{R}_z^2)}\,, \tag{3.15}$$

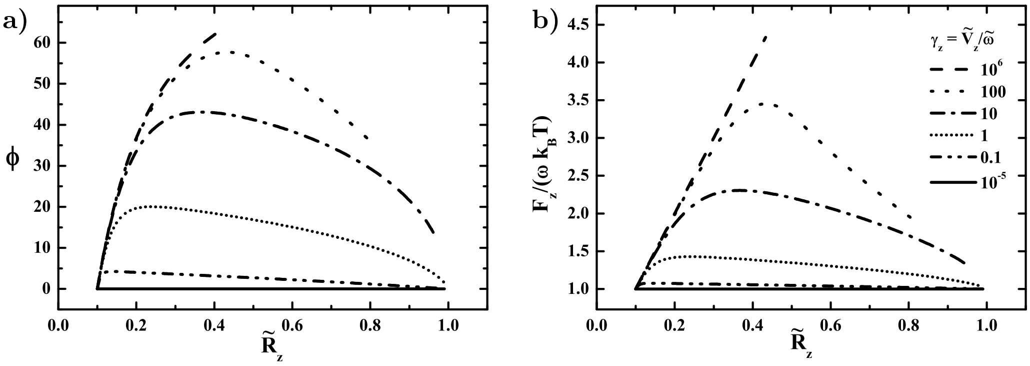

Figure 3.2: Vertical pulling: Evolution of **a)** the polymer angle ϕ and **b)** the vertical force in units of the adsorption energy per unit length $F_z/(\omega k_\mathrm{B}T)$ as functions of the normalized tip height $\tilde{R}_z = R_z/L$ and as obtained from the piecewise rod model Eq. (3.15). Results are shown for different values of the rescaled friction coefficient $\gamma_z = V_z\zeta L/\omega$, including the limiting cases of pure slip ($\gamma_z = 10^{-5}$, solid line) and pure stick ($\gamma_z = 10^6$, broken line).

where $\gamma_z = \tilde{V}_z/\tilde{\omega} = V_z\zeta L/\omega$ is the only material parameter remaining, measuring the ratio of friction versus adsorption strength. The differential equation is solved using standard finite difference techniques [95]. In Fig. 3.2 we show results a) for the polymer angle ϕ and b) for the vertical force F_z as a function of the cantilever height for different values of γ_z. In the very slippery case (solid line, $\gamma_z = 10^{-5}$) the desorbed polymer stays vertical and thus $\phi \simeq 0$ since the polymer can freely glide over the surface; the force shows a perfect plateau. In the very sticky case (upper broken line, $\gamma_z = 10^6$), the force grows linearly with the distance, as predicted by Eq. (3.9). In the intermediate case, the angle shows non-monotonic behavior: initially, the constantly moving cantilever exerts a growing force on the polymer, but as more polymer is desorbed the friction force decreases. Likewise, the vertical forces are much higher than the plateau force observed in the quasistatic limit which is due to a combination of dissipative and geometric effects.

Friction effects are most clearly exhibited when a surface-adsorbed molecule is moved laterally over the surface which is realizable using standard AFM technology [75]. With a finite lateral cantilever velocity V_x, the differential equation for the lateral polymer extension X, Eq. (3.12), is slightly modified

$$\dot{\tilde{X}} = \tilde{\omega}\frac{1 + \tilde{X}^2 - 2\tilde{X} - \tilde{R}_z^2}{(1-\tilde{X})(1-\tilde{X}^2-\tilde{R}_z^2)} + \tilde{V}_x\,, \tag{3.16}$$

where $\tilde{V}_x = V_x\zeta L^2$. The stationary geometry for horizontal pulling is achieved for long enough pulling times $t \to \infty$ and can be derived from the above equation by setting $\dot{\tilde{X}} = 0$. For a given pulling height, $\tilde{R}_z$, this fully determines the geometry of the adsorbed polymer and thus the force that is acting on the cantilever tip.

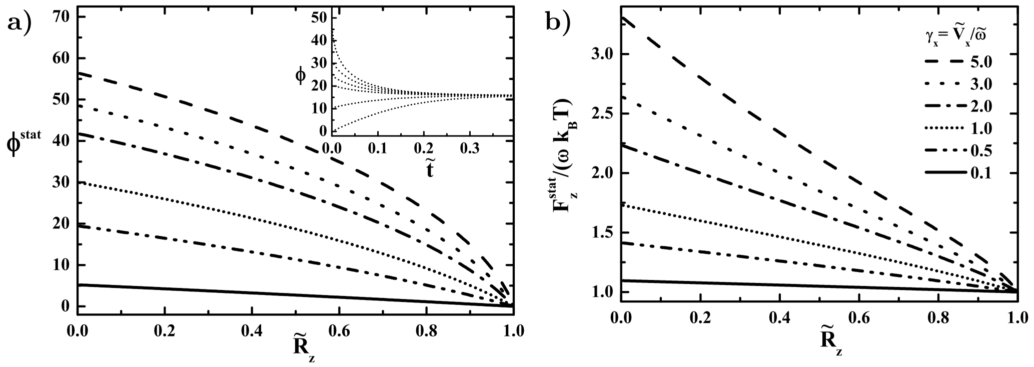

Figure 3.3: Results for horizontally moving cantilever as obtained from the piecewise rod model Eq. (3.16). **a)** Stationary polymer angle ϕ^{stat} and **b)** stationary vertical force in units of the adsorption energy per unit length, $F_z^{\text{stat}}/\omega k_{\text{B}}T$ as functions of the constant, normalized pulling height $\tilde{R}_z = R_z/L$. Results are shown for a set of different values of the friction parameter $\gamma_x = V_x\zeta L/\omega$, *i.e.* for different pulling speeds V_x, polymer lengths L or sliding friction coefficients ζ. The inset shows the time evolution of the angle ϕ for fixed $\gamma_x = 1$ and $\tilde{R}_z = 0.6$ for starting geometries with different angles as a function of the rescaled time $\tilde{t} = tL^3/\zeta$.

In Fig. 3.3 a) the angle and b) the (vertical) force acting on the cantilever in the stationary state, ϕ^{stat} and F_z^{stat} respectively, are shown as functions of varying height R_z for different friction to adsorption energy parameters $\gamma_x = \tilde{V}_x/\tilde{\omega} = V_x\zeta L/\omega$. Both decrease with increasing pulling height because the alignment becomes more vertical, and increase with increasing friction parameter γ_x in a monotonic but non-trivial way. The time evolution of the angle for different starting geometries is shown in the inset of Fig. 3.3a). From measurements of the stationary force acting at different pulling velocities or heights, the frictional coefficient can be inferred, once ω has been determined in sufficiently slowly performed vertical desorption experiments carried out under the same conditions. L can be determined in the same experiments as final height before complete desorption. By this procedure, measurements of frictional coefficients of single molecules on solid surface could be conducted, allowing for mapping out the dependence on parameters such as pH or added salt concentration. In AFM experiments where the maximal speed V is of the order of µm/s there is reason to believe that for many polymer-substrate combinations the friction parameter is quite small, *i.e.* $\gamma_x = \tilde{V}_x/\tilde{\omega} \ll 1$. In a small-$\gamma_x$ expansion we obtain for the stationary vertical force

$$
\begin{aligned}
\frac{F_z^{\text{stat}}}{\omega k_{\text{B}}T} &= 1 + \gamma_x(1 - \tilde{R}_z) + \mathcal{O}\left(\gamma_x^2\right) \\
&= 1 + (V_x L\zeta/\omega)(1 - R_z/L) + \mathcal{O}\left(\gamma_x^2\right) .
\end{aligned}
\tag{3.17}
$$

Similarly, the lateral force becomes

$$\frac{F_x^{\mathrm{stat}}}{\omega k_{\mathrm{B}}T} = \gamma_x(1-\tilde{R}_z) + \mathcal{O}\left(\gamma_x^3\right) . \tag{3.18}$$

These limiting laws allow for straightforward fitting of experimental data. Note that even in the case when the friction coefficient ζ is small, the effective friction parameter $\gamma_x = V_x L\zeta/\omega$ can be made sufficiently large by choosing very long polymers or increasing the pulling velocity. Thus there is hope that indeed AFM data can be used to extract friction coefficients of adsorbed single polymers, which is an important parameter in the context of adsorption and desorption kinetics. What remains to be elucidated is the microscopic mechanism behind the friction of adsorbed polymers, *i.e.* the dependence on the range of the surface-monomer interaction, the surface shape, and the distribution and density of interacting surface groups. Some of these questions will be approached in the following sections.

Note that in contrast to AFM or SFA studies on the nano-friction between two solid surfaces [68, 96], in our case the normal force is self-adjusted by the surface-polymer attraction forces and not a free parameter. There is an intimate coupling between the adsorption strength ω and the friction coefficient ζ, and it is the interplay embodied in the effective friction parameters $\gamma_{x,z}$, which determines the resulting behavior. Interesting physics is expected as $\omega a \to 1$ when polymer conformational fluctuations are modified due to the forced surface sliding; AFM methods, however, cannot probe this regime.

3.1.4 A minimal model for polymer friction at a flat wall

To test some of the conclusions of the simplistic analytical model, we propose a discrete model for polymer friction at a flat wall, similar to the BD model introduced in Section 2.3.1. Eq. (2.37) is adapted neglecting the thermal random term which is called the zero-temperature limit. In this context neglecting the thermal random noise term is used to obtain a discrete analog of the mechanistic, piecewise rod model used in the preceding sections. However, more generally, dropping the random force is also justified for strong external fields, *i.e.* strong adsorption and friction. In addition, the mechanistic nature allows us to use very long polymers because time consuming sampling is avoided; in this study we use $N = 500$. The equation of motion for the position of the ith monomer, $\boldsymbol{R}_i = (X_i, Y_i, Z_i)$, becomes

$$\frac{\mathrm{d}\boldsymbol{R}_i}{\mathrm{d}t} = -\mu(\boldsymbol{R}_i)\boldsymbol{\nabla}_{\boldsymbol{R}_i}U(t)\,, \tag{3.19}$$

where $\mu(\boldsymbol{R}_i)$ is the bare monomer mobility depending on the monomer position $\boldsymbol{R}_i$. The potential energy is modeled in the same way as before, *i.e.* the intramolecular term Eq. (2.40) ensures chain connectivity but prevents self-intersection, the interaction with an attractive, hard wall is taken into account using Eq. (2.41). Analogously to the exponentially decaying adsorption potential, the increased polymer friction close to the wall is incorporated into the bare monomer mobility also assuming an exponential form and lateral homogeneity,

$$\mu(\boldsymbol{R}_i) = \mu_\mathrm{b} + (\mu_\mathrm{s} - \mu_\mathrm{b}) \exp\left(-\kappa_\mu Z_i\right), \tag{3.20}$$

where μ_b and μ_s are the bulk ($Z_i \to \infty$) and surface ($Z_i = 0$) bare mobilities, and κ_μ is the mobility decay constant. The decay constant is chosen to be the same as that of the adsorption potential, in rescaled units $\tilde{\kappa}_\mu = \tilde{\kappa} = 2$. After rescaling, the bulk mobility can be arbitrarily chosen as an effective integration time step, where we use $\tilde{\mu}_\mathrm{b} = 10^{-4}$. The simulations are done for different values of the effective surface mobility ($0.01 \leq \mu_\mathrm{s}/\mu_\mathrm{b} \leq 1.0$) which is the second new parameter. The first monomer is moved either normal or parallel to the surface with a constant rescaled velocity $\tilde{V}_x = V_x a / k_\mathrm{B} T \mu = 0.1$ and 1 or $\tilde{V}_z = 1$, respectively. Other parameters are chosen as described in Section 2.3.1, except for $\chi = 100$ and $\tilde{k} = 5000$.

In Fig. 3.4 we show the angle ϕ defined in Fig. 3.1 as a function of the rescaled height of the first monomer, $\tilde{R}_z = R_z/L \approx \tilde{Z}_1/N$. The pulling velocity is $\tilde{V}_z = 1$; the starting geometry is the same as for Fig. 3.2, *i.e.* a linearly aligned polymer with the free part normal to the surface and ending at $\tilde{R}_z = 0.1$. The effective surface mobility is changed from rather sticky conditions ($\mu_\mathrm{s}/\mu_\mathrm{b} = 0.01$, broken line) to no additional surface friction ($\mu_\mathrm{s}/\mu_\mathrm{b} = 1$, dotted line). Even in the case of vanishing surface effect and homogeneous mobility, $\mu = \mu_\mathrm{b} = \mu_\mathrm{s}$, the angle does not stay zero as it does in the rod model. This is due to a combination of a geometric effect, see Fig. 3.1, and the homogeneous, but necessarily non-zero friction experienced by the polymer. Accordingly, in this BD model even for $\mu_\mathrm{s} = \mu_\mathrm{b}$, the vertical force is larger than its equilibrium value (not shown) as opposed to the rod model. Overall, a very similar picture is obtained as compared with the rod model of the preceding sections.

A similar result is obtained for horizontal pulling. In Fig. 3.5 we plot the time evolution of the angle ϕ for pulling with a constant lateral velocity $\tilde{V}_x = 0.1$. The rescaled time in simulation units reads $\tilde{t} = n\tilde{\mu} = t\mu k_\mathrm{B} T/a^2$ where n is the number of simulation steps. The ratio of surface *vs.* bulk mobility is changed in the simulations in the same regime as for vertical pulling, cf. the legends. The pulling height is in all cases fixed to $\tilde{R}_z/L \approx Z_1/N = 0.4$, whereas other parameters are kept unchanged. The starting configuration is in all cases with the free strand vertically upright from the surface. Summarizing, we again find good qualitative agreement with the results from the analytical, piecewise rod-model. We expect the discrete simulation model to be of further use for more complicated geometries than the simplified stretched out geometry considered here. In a similar fashion, a related Monte Carlo model has been used for studying the adsorption dynamics of flexible polymers [81, 82].

3.2 Polymer friction in a Frenkel-Kontorova type model

A simplistic model for the plastic deformation of solids has been introduced by Frenkel and Kontorova as early as 1938. Their model consists of a string of particles

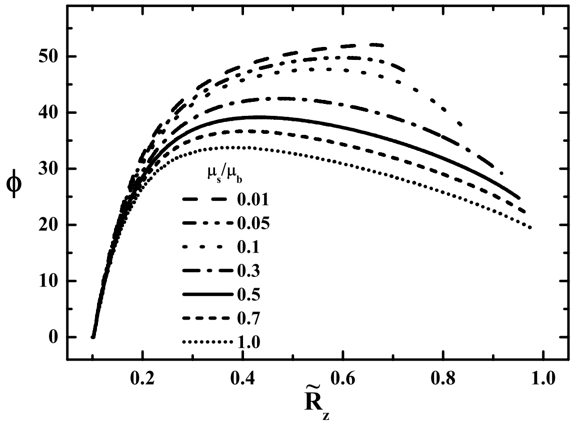

Figure 3.4: Vertical pulling: Evolution of the polymer angle ϕ as a function of the normalized tip height $\tilde{R}_z \approx \tilde{Z}_1/N$ and as obtained from mechanistic simulations. Results are shown for different values of the ratio between the surface and bulk mobilities, $\mu_\mathrm{s}/\mu_\mathrm{b}$, see also the legend. Here, $\chi = 100$, $\tilde{\kappa}^{-1} = \tilde{\kappa}_\mu^{-1} = 0.5$, and $\tilde{V}_z = V_z a/k_\mathrm{B}T\mu = 1$, for other parameters see text. The simulation results compare qualitatively well with the analytical model, cf. Fig. 3.2.

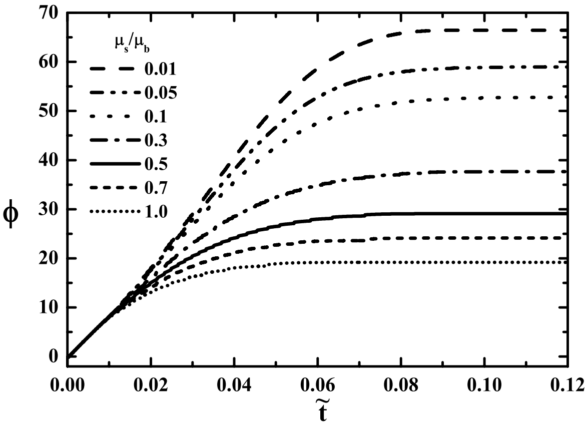

Figure 3.5: Evolution of the polymer angle ϕ as a function of the rescaled time variable $\tilde{t} = t\mu k_\mathrm{B}T/a^2$ for horizontal pulling and as obtained from mechanistic simulations. Results are shown for different values of the ratio between the surface and bulk mobilities, $\mu_\mathrm{s}/\mu_\mathrm{b}$, see also the legend. In the simulations we employ $\chi = 100$, $\tilde{R}_z/L \approx Z_1/N = 0.4$, and $\tilde{V}_x = V_x a/k_\mathrm{B}T\mu = 0.1$, for other parameters see text. The simulation results compare qualitatively well with the analytical model, cf. Fig. 3.3.

interconnected by harmonic springs which is situated in a one-dimensional sinusoidal potential. One of the particles is driven by an external force, see also Fig. 3.6. Despite its simplicity this model has also been applied among others for the dry friction between two solids [32, 69, 97, 98]. In this case the string of particles represents the interfacial atoms of one of the two surfaces, and the periodic potential constitutes a minimal description of the interfacial atoms of the other surface. For monomer i which here is supposed to be the one driven by the external force F the equation of motion reads

$$m_i \frac{\mathrm{d}^2 X_i}{\mathrm{d}t^2} = -\frac{1}{\mu_i} \frac{\mathrm{d}X_i}{\mathrm{d}t} - \frac{\partial U}{\partial X_i} + \xi_i(t) + F \,, \tag{3.21}$$

where X_i is the particle position, m_i its mass, and μ_i its intrinsic mobility. $\xi_i(t)$ is a random thermal force, U the total potential, and F the external pulling force. As discussed in Section 1.2 the inertial term can be neglected in solution giving the overdamped equation of motion analogous to Eq. (2.37),

$$\frac{\mathrm{d}X_i}{\mathrm{d}t} = \mu_i \left[-\frac{\partial U}{\partial X_i} + \xi_i(t) + F \right] . \tag{3.22}$$

Here, $\xi_i(t)$ again fulfills Eq. (2.38). The total potential is the sum of the external potential exerted by the second surface and the intramolecular potential, $U = U^{\mathrm{surf}} + U^{\mathrm{poly}}$. The latter is constructed by intramolecular harmonic bonds between nearest neighbors with a force constant k around the equilibrium value of the bond length a, see also Eq. (2.40). For a string of N particles, the spatially and temporally fixed external potential stemming from the second surface is given by

$$U^{\mathrm{surf}} = \sum_{i=1}^{N} \left[U_0 - U_0 \cos\left(2\pi X_i / l\right) \right] , \tag{3.23}$$

where U_0 is the potential corrugation and l the lattice spacing of the surface. Again, a rescaling by $k_{\mathrm{B}}T$ and l is done as introduced in Section 2.3 yielding rescaled values $\tilde{U} = U/k_{\mathrm{B}}T$, $\tilde{X}_i = X_i/l$, $\tilde{F} = Fl/k_{\mathrm{B}}T$ *etc.* As easily seen from the discussion in the previous chapter, this model can also be used to describe the situation of a polymer driven over a surface. The commensurability or incommensurability of the system is known to have a great impact on the friction [69, 97]. Commensurability is defined as a/l being a rational number; incommensurability occurs when this quotient is an irrational number. For two and three dimensional systems the angular arrangement of the lattices also plays a role. Here, we only consider commensurable systems, and mostly restrict the discussion to the simplest case with $l = a$.

The physics of the Frenkel-Kontorova model is quite well understood in terms of mechanic instabilities or pops which add to the intrinsic damping stemming from *e.g.* solvent friction. The mean normalized mobility is defined as

$$\bar{\mu} = \frac{N \langle \mu \rangle}{\mu} = \frac{N \left\langle \dot{X}_1 \right\rangle}{F \mu} \,, \tag{3.24}$$

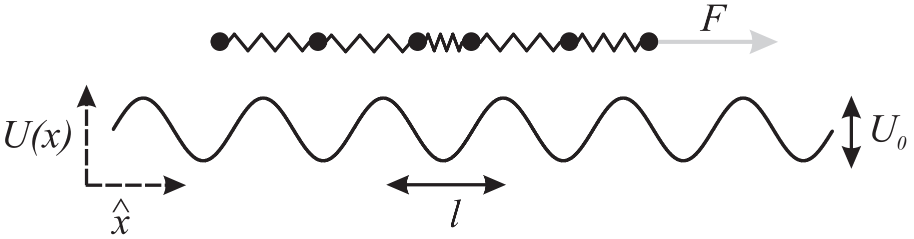

Figure 3.6: The Frenkel-Kontorova model as used for the friction of a single polymer on a corrugated surface. The model is one-dimensional and incorporates a sinusoidal potential energy landscape with depth U_0 and lattice constant l. Nearest neighboring monomers are connected via harmonic springs with a spring constant k and a equilibrium distance a. An external force F acts on the first monomer.

where $\langle\mu\rangle = \langle\dot{X}_1\rangle/F$ is the average polymer mobility and $\dot{X}_1$ is the velocity of the first particle on which the external force F is exerted. For exemplary parameter values $l = a$, $\tilde{U}_0 = 5$, $\tilde{k} = 4000$, and $N = 10$ we show in Fig. 3.7 the average normalized mobility as a function of the rescaled pulling force $\tilde{F}/N$ (crosses). In the same graph the mobility of a single particle ($N = 1$) is also presented (circles).

Crudely summarizing the interpretation of the Frenkel-Kontorova model, the particle or the particle string is trapped and sticks to favorable potential sites, and the relatively large velocities generated by sudden partial or concerted movements over the potential barriers is quickly damped by exciting faster degrees of freedom which are implicitly incorporated in the intrinsic friction coefficient, μ^{-1}. Thus, the motion is largely characterized by a stick-slip nature where virtual bonds to the substrate, *i.e.* trapping in potential minima, are broken and re-formed. Hence the solvent friction is increased. In the limit of zero velocity or vanishing external pulling force, the effective mobility is solely determined by thermally activated diffusion processes. With increasing external forces the mean mobility approaches its intrinsic value μ/N, since the corrugation of the external potential becomes negligible as compared with the potential tilt introduced by the pulling force. The motion gradually switches from a stick-slip nature to a continuous, smooth motion.

The virtually static friction with an exponentially small rescaled mobility is overcome at values of $\tilde{F}/N$ which are smaller for the monomer than for the decamer, see Fig. 3.7. For pulling forces larger than the intersection point at about $\tilde{F}/N \approx 25$, the rescaled mobility of the decamer is larger than for the monomer and reaches unity at smaller values of the pulling force. These observations are in correspondence with the idea of concerted motion in the case of the decamer. For purely thermal motion, *i.e.* in the low-force limit, the necessarily concerted motion of the decamer is suppressed and the mobility is reduced. In the high-force limit, pops of chain segments can act as promoters of motion. This effect strongly depends on the ratio of the force constant and the potential strength, l^2k/U_0, but also on the com-

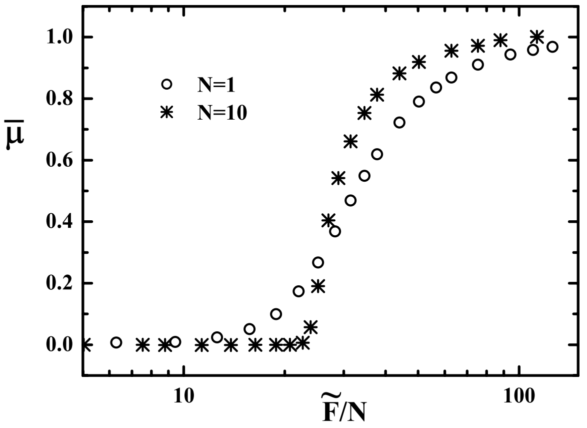

Figure 3.7: Average normalized mobility $\bar{\mu} = N\langle\mu\rangle/\mu$ as a function of the rescaled pulling force $\tilde{F}/N = Fl/Nk_{\rm B}T$ for a monomer (circles) and a 10mer (crosses). The potential depth is the same for both cases, $\tilde{U}_0 = 5$. Additional parameters in the decamer case are $a = l$, $\tilde{k} = 4000$.

mensurability of the lattices a and l as already discussed in the literature [69, 97]. The simple rationale described here is only true for the commensurable case $a = l$.

To demonstrate the impact of the lattice structure we show in Fig. 3.8 the rescaled mobility of the decamer on lattices with $a = n \times l$, where $n = 1, 2, 4$, and on a lattice with $a = l/2$. While the polymers with a bond length that is an integer multiple of the lattice constant have identical mobilities, the mobilities for the polymer with $a = l/2$ approach unity much faster, *i.e.* for much smaller values of the external force. Also, in the latter case the fluctuations are comparably large. Note that it is hard to approach the true incommensurable case in simulations due to their finite numerical precision. Also, proper scaling behavior of incommensurable systems is only found for $N \to \infty$. However, the simpler *commensurable* case with $a = l/2$ indeed shows greatly reduced friction due to out-of-phase monomer positions as in contrast to an all-in-phase motion when the bond length is an integer multiple of the potential lattice constant. Similar trends are expected for incommensurable lattices for large enough N [69].

As demonstrated in Fig. 3.7 a relative mismatch of the normalized mobility as a function of the normalized force $\tilde{F}/N$ for chains of different length persists even in the simplest commensurable case with $a = l$. This suggests non-trivial and non-universal scaling of the mobility with the length of the polymer for all but the high-force regime where the intrinsic mobility is reached and thus the mobility scales as $\langle\mu\rangle \approx \mu/N \propto N^{-1}$ in consistency with a Rouse model. To test the hypothesis of non-universal scaling, the scaling dependence is checked for a pre-selected value of the force and for the lattices with $l = a$ and $l = 2a$ as shown in Fig. 3.9. The force for the case with $l = 2a$ is chosen as $\tilde{F} = 188$. Indeed, we observe the high-force regime with linear scaling $\langle\mu\rangle \propto N^{-1.00}$. For the simple commensurable case,

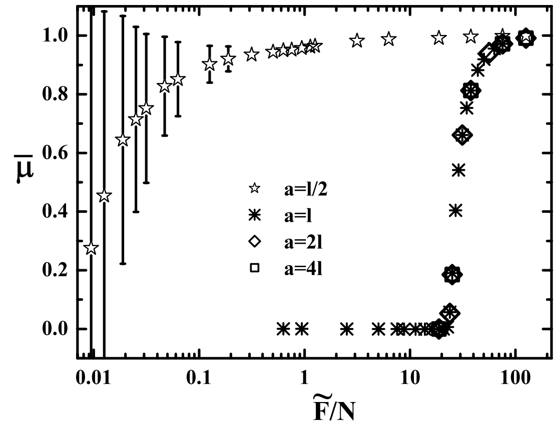

Figure 3.8: Average normalized mobility $\bar{\mu} = N\langle\mu\rangle/\mu$ as a function of the rescaled pulling force $\tilde{F}/N = Fl/Nk_\mathrm{B}T$ for a 10mer on lattices with $a = l$ (crosses), $a = 2l$ (diamonds), $a = 4l$ (squares), and $a = l/2$ (stars). Other parameters are the same, $\tilde{k} = 4000$ and $\tilde{U}_0 = 5$. Error bars are shown when larger than the symbol size. The mobilities of polymers with a bond length that is a multiple integer of the lattice constant superimpose to the same curve for the decamer presented in Fig. 3.7. For $a = l/2$, the mobilities are comparably large at already small values of the external force and fluctuate extensively.

$l = a$, the force is $\tilde{F} = 628$, and hence covers both the high- and the medium-force regime over the polymer length investigated here. Still, the scaling found here only marginally differs from linear scaling, we find $\langle\mu\rangle \propto N^{-1.07}$. Obviously this result depends on both the range of polymer lengths and the pulling force, in addition to the parameters describing the polymer-surface interaction, *i.e.* the potential depth and the ratio of the polymer and surface lattice constants. Nonetheless, we conclude that for small polymers with $N < 100$ the assumption of inverse linear scaling of the average polymer mobility in the polymer length is well justified. This will be of further use in Section 3.3.

Following Persson [67, 99] we now discuss the low- and high-force limit of the overdamped motion of a single particle in the periodic potential Eq. (3.23) defined by Eq. (3.22). For small pulling forces $Fl \ll k_\mathrm{B}T \ll U_0$, the motion is solely controlled by thermally activated diffusion and can be described by a Kramers rate process where the normalized mobility of the particle is given by [32, 57]

$$\bar{\mu} = \frac{\langle\mu\rangle}{\mu} = \frac{2\pi\tilde{U}_0}{\tilde{F}} \exp\left(-2\tilde{U}_0\right) \left[\exp\left(\tilde{F}/2\right) - \exp\left(-\tilde{F}/2\right)\right] . \qquad (3.25)$$

Hence, the motion is exponentially damped. In the high-force regime, *i.e.* for $Fl \gg U_0$, we rewrite the particle motion as

$$X = vt + u\,, \qquad (3.26)$$

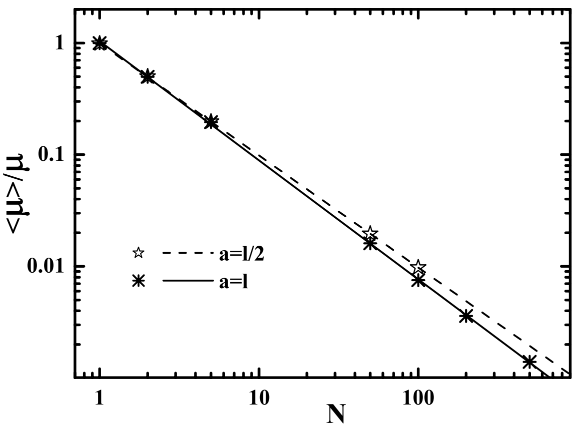

Figure 3.9: Average normalized mobility $\langle\mu\rangle/\mu$ as a function of the polymer length N for the simplest commensurable lattice with $l = a$ (crosses, solid line) and a lattice with $l = 2a$ (stars, broken line). In both cases, $\tilde{U}_0 = 5$ and $\tilde{k} = 4000$. For $a = l$, the external force is $\tilde{F} = 628$, *i.e.* it covers both the high- and medium-force regime over the polymer length considered here; for $a = l/2$, $\tilde{F} = 188$ which is in the high-force regime throughout the polymer length checked here. Also shown are linear fits on the log-log scale leading in both cases to approximately linear scaling, *i.e.* $\langle\mu\rangle \propto N^{-1.07}$ for $a = l$ and $\langle\mu\rangle \propto N^{-1}$ for $a = l/2$.

where $v = \langle\dot{X}\rangle$ is the *average* velocity of the particle, and $u = u(t)$ is a time-dependent contribution due to the thermal noise and the substrate potential. With that, Eq. (3.22) becomes

$$\mu^{-1}\frac{\mathrm{d}X}{\mathrm{d}t} = \mu^{-1}\left[v + \frac{\mathrm{d}u}{\mathrm{d}t}\right] = -\frac{2\pi U_0}{l}\sin\left([vt+u]2\pi/l\right) + \xi(t) + F\,. \tag{3.27}$$

Using $\langle\mu\rangle = v/F$ and expanding to first order in u we get

$$\mu^{-1}\frac{\mathrm{d}u}{\mathrm{d}t} = -\frac{2\pi U_0}{l}\sin(2\pi vt/l) - \frac{4\pi^2 U_0 u}{l^2}\cos(2\pi vt/l) + \xi(t) + v(\langle\mu\rangle^{-1} - \mu^{-1})\,. \tag{3.28}$$

Choosing $u(t=0) = 0$ gives $\langle u\rangle = 0$ since $\langle \mathrm{d}u/\mathrm{d}t\rangle = 0$. Time averaging of Eq. (3.28) and rearranging terms yields

$$v(\langle\mu\rangle^{-1} - \mu^{-1}) = \frac{4\pi^2 U_0}{l^2}\left\langle u\cos(2\pi vt/l)\right\rangle\,. \tag{3.29}$$

The leading contribution of Eq. (3.28) is given by $\mu^{-1}\frac{\mathrm{d}u}{\mathrm{d}t} = -(2\pi U_0/l)\sin(2\pi vt/l) + \xi(t)$, integration of which yields

$$u = u_{\mathrm{T}} + \frac{U_0\mu}{v}\left[\cos(2\pi vt/l) - 1\right]\,. \tag{3.30}$$

where we split u into a thermal contribution u_T due to ξ (with $u_\mathrm{T}(t=0) \equiv 0$), and a substrate contribution. Substitution of Eq. (3.30) into Eq. (3.29) and subsequent time averaging and rearranging gives

$$\frac{\mu}{\langle \mu \rangle} = 1 + 2 \left(\frac{\pi \mu U_0}{vl} \right)^2 . \tag{3.31}$$

For the high-force limit we again use $\langle \mu \rangle \to \mu$ on the right-hand side of the equation and rearrange to

$$\bar{\mu} = \frac{\langle \mu \rangle}{\mu} \approx \left(1 + 2\pi^2 \frac{\tilde{U}_0^2}{\tilde{F}^2} \right)^{-1} . \tag{3.32}$$

Hence, for the overdamped motion of a single particle we find the effective mobility to asymptotically approach the intrinsic mobility as $\langle \mu \rangle / \mu \sim 1 - 2\pi^2 U_0^2 / F^2 l^2$. This is in contrast to the case of a particle with finite mass m where a similar procedure gives $\langle \mu \rangle / \mu \sim 1 - U_0^2 / 2F^4 \mu^4 m^2$ to leading order [67]. In Fig. 3.10 we plot BD simulation data for $\tilde{U}_0 = 5$ (circles) together with the asymptotic limits of the low-force regime (Eq. (3.25), broken line) and of the high-force regime (Eq. (3.32), dotted line) as well as the full solution (solid line) which is given by [32]

$$\bar{\mu} = \frac{\langle \mu \rangle}{\mu} = 1 + \frac{2\pi \tilde{U}_0}{\tilde{F}} \Im \left(\frac{I_{1+i\tilde{F}/2\pi}(\tilde{U}_0)}{I_{i\tilde{F}/2\pi}(\tilde{U}_0)} \right) , \tag{3.33}$$

where $I_n(x)$ are modified Bessel functions of the first kind. The simulation data are in excellent agreement with the analytic predictions. However, given the complexity of realistic potential energy landscapes and timescales of particle interactions and motions in solution, such simplified models can only grasp very basic concepts of friction. In the following section we will illustrate this with a microscopic model in which both the polymer and the solid-liquid interface are taken into account with atomistic resolution.

3.3 Polypeptide friction on a hydrophobic and a hydrophilic surface

Up to now, little is known about the microscopic origin of single polymer friction on an atomistic level of detail. In experiments, usually diffusion coefficients are determined which are defined as

$$D = \lim_{t \to \infty} \left\langle \left(\boldsymbol{R}(0) - \boldsymbol{R}(t) \right)^2 \right\rangle / 2dt \, , \tag{3.34}$$

where d is the dimensionality and $\boldsymbol{R}(t)$ the center of mass position of the molecule at time t. Using simulations it is often difficult to determine small diffusion coefficients due to long simulation times. In many cases it is more convenient to apply a force

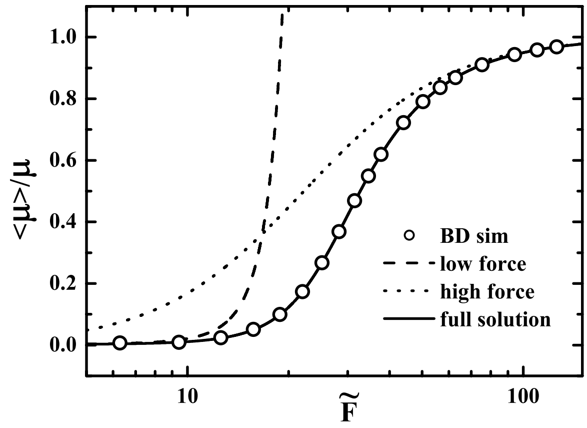

Figure 3.10: Average normalized mobility $\langle\mu\rangle/\mu$ in a sinusoidal potential as a function of the rescaled pulling force $\tilde{F} = Fl/k_{\mathrm{B}}T$. The rescaled potential depth is $\tilde{U}_0 = U_0/k_{\mathrm{B}}T = 5$. Shown are BD simulation results (circles), the low-force regime asymptotics Eq. (3.25) (broken line), the high-force regime asymptotics Eq. (3.32) (dotted line), and the full solution Eq. (3.33) (solid line).

and to look at the polymer mobility μ. Interconversion can be done via the Einstein relation,

$$D = \mu k_{\mathrm{B}} T\,. \tag{3.35}$$

In the following it will be shown how atomistic MD studies in which an external force is applied to a polymer molecule can help understanding its friction on a solid-water interface.

One class of experimentally as well as theoretically attractive polymers are peptides which are the main constituents of proteins [12]. Proteins then again represent one of the classic examples in the soft matter area where the interplay between covalent bonds, partial and ionic charges, and hydrophobic interaction plays a decisive role, *e.g.* in protein folding or adsorption [100, 101]. A well-defined model system due to its high degree of monodispersity and comparably large polymerization index is the mildly hydrophobic polypeptide C16 derived from the silk protein ADF-4 of the garden spider *Araneus diadematus*. The polypeptide chain consists of 16 repeat units each of which is 35 amino acids long. It has recently been achieved to measure single polymer adsorption forces of C16 on hydrophobic, H-terminated diamond surfaces, and on hydrophilic, OH-terminated diamond substrates [102]. At the same time, MD simulations can serve as a theoretical tool to probe the adsorption and friction forces acting on the peptide molecule. The differences between the hydrophobic and hydrophilic surfaces play an important role in this context. Readers unfamiliar with the concept of hydrophobicity and hydrophobic interactions are referred to the literature [101, 103, 104], since a detailed introduction into this field is out of the scope of this work.

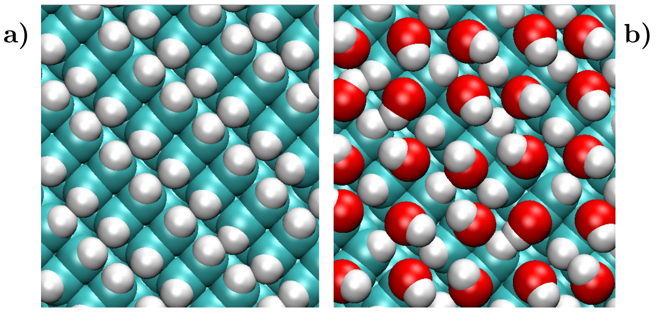

Figure 3.11: Snapshots of atomistic models for **a)** hydrophobic and **b)** hydrophilic diamond surfaces as used in MD simulations. The hydrophobic surface is 100 % terminated with H atoms, for the hydrophilic surface half of the H atoms are substituted by OH groups. See text for details.

3.3.1 Molecular dynamics simulation details

The Gromos96 force field parameterization [105] is used to model a diamond slab of approximate dimensions $d_x \times d_y \times d_z = 6\,\text{nm} \times 3\,\text{nm} \times 1.8\,\text{nm}$ whose (100) surface is fully terminated with hydrogen atoms. In the case of a hydrophilic surface, half of the hydrogen atoms are replaced by hydroxyl groups, using the Gromos96 bond and partial charge parameterization of the COH group as defined in a serine residue. The partial charges for COH hence are $0.266\,e$ for C, $-0.674\,e$ for O, and $0.408\,e$ for H; all other partial charges in the diamond are set to zero. Note that in both the CH groups in the case of the hydrophobic diamond surface and in the COH groups for the hydrophilic surface each atom is modeled by the full Gromos96 potential which in addition to partial charges includes Lennard-Jones interactions and potentials for bond stretching, as well as bond angle and dihedral angle deformation. The wetting properties of the surfaces have been determined by simulations [102]; the hydrophobic surface gives a contact angle of 106° with water, the hydrophilic surface is completely wet by water. Top views of the two surface types are shown in Fig. 3.11. About 3000 SPC water molecules [106] are added above and below the diamond slab filling the simulation box of approximate size $b_x \times b_y \times b_z = 6\,\text{nm} \times 3\,\text{nm} \times 7\,\text{nm}$.

One repetitive unit of the C16 motif of spider silk contains 35 amino acids which is too long for an efficient simulation with explicit solvent. Therefore we consider only the terminal part containing the residues 21-35, NQGPSGPGGYGPGGP; for amino acid abbreviations see Ref. [107]. This mildly hydrophobic peptide part is in the following referred to as 'the polypeptide'. The force field parameters for the polypeptide atoms are taken from the Gromos96 force field, version 53A6 [108]. Initially, the peptide is placed in the simulation cell above the surface before the cell is filled with water.

Our standard MD procedure consists of NPT simulations using the Gromacs package [109, 110], *i.e.* MD simulations performed at constant particle number N, pressure $P = 1\,\text{bar}$ and temperature $T = 300\,\text{K}$ using a time step of 2 fs. To equilibrate the system, we first carry out an energy minimization of the simulation system, followed by a 50 ps $N\mathcal{V}T$ relaxation and a 500 ps $NP_z\mathcal{A}T$ relaxation. Here, $\mathcal{V}$, $\mathcal{A}$, and P_z denote the total volume of the simulation box, the area of the slab, and the pressure along the direction of the surface normal $\hat{z}$, respectively, which are held constant. During this initial relaxation, the polypeptide adsorbs readily onto the surface. For data acquisition NPT simulations under periodic boundary conditions and with a duration between $t = 5\,\mathrm{ns}$ and 20 ns are performed using Berendsen's schemes for temperature and semi-isotropic pressure coupling [111]. The compressibilities are adjusted to the bulk diamond and bulk water values, $\kappa_{xy} = 2.5 \times 10^{-8}\,\mathrm{bar}^{-1}$ and $\kappa_z = 4.5 \times 10^{-5}\,\mathrm{bar}^{-1}$, respectively. The particle-mesh Ewald method [112] is used for the periodic treatment of Coulombic interactions, the LINCS algorithm [113] for constraining covalent bonds involving hydrogen atoms. The center of mass translation and the rotation around the center of mass are removed.

A virtual cantilever is attached to the center of mass of the first amino acid via a harmonic spring with a force constant between $50\,\mathrm{kJ/(mol\,nm^2)} \approx 20\,\mathrm{k_BT/nm^2}$ and $3000\,\mathrm{kJ/(mol\,nm^2)} \approx 1200\,\mathrm{k_BT/nm^2}$ and moved with velocities between $V = 0.1\,\mathrm{m/s}$ and 250 m/s in the $\hat{x}$ direction. The spring potential is independent of the polymer height and only acts in the plane parallel to the surface, *i.e.* the $\hat{x}$ and $\hat{y}$ directions. For the case of bulk water, simulations are conducted in a $b_x \times b_y \times b_z = 10\,\mathrm{nm} \times 4\,\mathrm{nm} \times 4\,\mathrm{nm}$ simulation box filled with about 5400 water molecules. Average mobilities $\langle \mu \rangle$ are calculated from the displacement of the first amino acid, ΔX, and the force measured by the spring extension, F_x, according to

$$\langle \mu \rangle = \frac{\Delta X}{\langle F_x \rangle \, \Delta t} \,. \tag{3.36}$$

The dissipated power $\mathcal{P}^i$ is calculated in an analogous fashion,

$$\mathcal{P}^i = \frac{\Delta X \, \langle F_x^i \rangle}{\Delta t} \,, \tag{3.37}$$

where in this approach the forces F_x^i are the forces exerted by all atoms of a group i on all peptide atoms. These forces are calculated explicitly from the force field using either all atoms of the diamond slab ($\mathcal{P}^{\mathrm{surf}}$ and F_x^{surf}) or all atoms belonging to water molecules ($\mathcal{P}^{\mathrm{H_2O}}$ and $F_x^{\mathrm{H_2O}}$). Necessarily, after reaching a steady state and then time averaging, the sum of these forces equals the external pulling force in magnitude but points in the opposite direction. For convenience we define the dissipative force contribution by group i as *positive* values of F_x^i, and hence $\langle F_x \rangle = \sum_i \langle F_x^i \rangle$.

For all time averaged quantities error estimates are obtained via block averaging, where the block size typically is $\Delta t = 3.8\,\mathrm{ns}$ and for which the first ns of the simulation is disregarded for equilibration. Error bars are only shown when larger than the symbol size. The number of hydrogen bonds, n_{HB}, is analyzed in terms of a distance criterion between donor and acceptor atoms as defined elsewhere [114].

3.3.2 Peptide mobilities on surfaces and in bulk water

The laterally driven polypeptide shows distinctly different behavior on the hydrophilic surface as compared with the hydrophobic diamond. In Fig. 3.12 we show two exemplary force traces, one for pulling with $V = 10\,\text{m/s}$ over the hydrophobic H-terminated diamond surface (grey data points), the other for the hydrophilic 50 % OH-terminated surface and a pulling speed of $V = 0.5\,\text{m/s}$ (black). Although the pulling velocity on the hydrophobic surface is larger by a factor of 20, we observe a mean force on the hydrophobic substrate of about $\langle F_x \rangle = 170\,\text{pN}$, while the averaged force on the hydrophilic substrate is as large as $\langle F_x \rangle = 600\,\text{pN}$. Also the type of motion is entirely different. On time and length scales investigated here, the force on the polymer adsorbed to the hydrophobic substrate varies only little. On the hydrophilic surface pronounced stick-slip behavior is found, with force peaks of up to $F_x = 1.5\,\text{nN}$. The same features, smooth movement on the hydrophobic surface and stick-slip motion on the hydrophilic substrate, are observed in the displacement of the first amino acid which we plot for both cases in Fig. 3.13 using the same color coding. From analogous force and displacement traces the average mobilities are calculated for different pulling speeds and are shown in Fig. 3.14. The black circles correspond to simulations with the hydrophilic surface, the grey diamonds denote values for the hydrophobic diamond, and the crosses represent measurements in bulk water. Overall, the presence of the hydrophobic surface leads to slightly *larger* mobilities at high pulling velocities than in bulk water and up to threefold increased friction or lower mobilities at low pulling rates. For these two cases extrapolation to the linear response limit, $V \to 0$, is possible and yields $\mu_{\text{bulk}} = (6 \pm 1) \times 10^{10}\,\text{s/kg}$ and $\mu_{\text{phob}} = (2 \pm 1) \times 10^{10}\,\text{s/kg}$ for bulk water and the hydrophobic surface, respectively. On the hydrophilic surface only an upper bound of about $\mu_{\text{phil}} < 6 \times 10^{8}\,\text{s/kg}$ can be established assuming that μ monotonically decreases to its value in the linear response limit as $V \to 0$.

The precise length scaling of the mobilities or diffusion coefficients for polymers adsorbed to surfaces is disputed in the literature. Rouse type $\mu \propto N^{-1}$ [70], sublinear $\mu \propto N^{-3/4}$ [86] as well as superlinear scaling $\mu \propto N^{-3/2}$ [72] have been found. For short enough chains such as ours we expect Rouse type behavior on the surfaces as also discussed in Section 3.2, and only marginal deviations even in the bulk case, if at all. For a comparison with literature values we therefore rescale all mobilities with the number of amino acids in the polypeptide to get the monomer mobility, $\mu_{\text{mono}} = N\mu$, with $N = 15$. Hence we also neglect slight differences in the types of amino acids. In Table 3.1 we compare our results to values published in the literature. The data are grouped in mobilities measured in bulk water, mobilities of polymers adsorbed to a hydrophobic surface but measured in solution, and mobilities measured at the water-hydrophilic substrate interface. All literature values are converted into monomer mobilities using the linear Rouse scaling, with the following exceptions: For the data on peptides in bulk water by Danielsson *et al.* [115] we use the scaling presented there and the molar mass of the polypeptide in our simulations; for the data on ds-DNA in bulk water by Nkodo *et al.* [116] the authors' scaling as $N^{-0.57}$ is employed. For PEG polymers, which were adsorbed to silica hydrophobized with a self-assembled monolayer (SAM), the data by Sukhishvili *et al.* [72, 73] is converted using the $N^{-3/2}$ scaling proposed by the authors due to reptation. Again, the use of different scaling functions also for the data in bulk water is justified due to the much longer polymers used in the experimental studies than in our simulations. Summarizing, our mobility compares astonishingly well for the bulk water case. Also the mobilities on surfaces are within reasonable agreement considering that experimental data is only available for other types of polymers.

Using our mobility values, the friction force for pulling the polypeptide ($N = 15$) over a surface at a speed of $V = 0.1\,\mathrm{m/s}$ is given by $F_x \approx 5\,\mathrm{pN}$ for a hydrophobic and $F_x \approx 170\,\mathrm{pN}$ for a hydrophilic surface. Even for velocities as high as that, in the hydrophobic case friction is smaller than the typical desorption force of $F = 55\,\mathrm{pN}$ which has been determined by AFM experiments and complementary MD simulations [102] in which the polymer was vertically pulled off from the substrate. This fact allows reaching equilibrium on typical MD simulation timescales. In the hydrophilic case friction dominates and prevents equilibration in simulations. The situation is much more favorable in AFM experiments, since there the pulling speeds are smaller by five orders of magnitude. The estimated friction forces in a typical AFM experiment with $V = 1\,\mathrm{\mu m/s}$ for a complete C16 polypeptide, which is approximately comprised of 16×2.3 units of the polypeptide considered here, would be $2\,\mathrm{fN}$ on the hydrophobic diamond and $60\,\mathrm{fN}$ on the hydrophilic surface. Compared to the desorption force of $F = 55\,\mathrm{pN}$ or to the typical AFM force resolution of about one piconewton, the friction forces are irrelevant.

Note that for both surfaces the mobilities obtained here can only serve as upper bounds since surface heterogeneity, impurity, and roughness on all length scales are expected to increase polymer friction. In the following section the mobility data is rationalized in more depth and the dissipative mechanisms are analyzed in detail. For that we start with the hydrophobic substrate and later turn to the hydrophilic surface.

3.3.3 Dissipation mechanisms on hydrophobic and hydrophilic surfaces

In the case of the hydrophobic surface and of bulk water the large uncertainties in the mobilities obtained for pulling velocities of $V \leq 1\,\mathrm{m/s}$ are due to relatively small friction forces as compared to entropic stretching forces and hence large fluctuations of the chain geometry. For a crude estimate the regime of strong deformation for a Gaussian chain with a harmonic spring constant given by Eq. (3.4) is reached when the extension in the direction of the force $x_{N1} = X_1 - X_N$ is of the order of the unperturbed end-to-end distance, $x_{N1} \approx R_{\mathrm{ee}} = \sqrt{N}a$. Hence, the force needs to exceed $F_x \geq 3k_{\mathrm{B}}T/R_{\mathrm{ee}} \approx 40\,\mathrm{pN}$ using $N = 15$ and $a = 0.8\,\mathrm{nm}$. This rough estimate is in agreement with the more rigorous treatment in Section 4.1. In the above-mentioned cases the friction forces are smaller or just about this threshold which suggests only weak perturbations of the peptide random coil configuration and

Table 3.1: Linear response ($V \rightarrow 0$) monomer mobilities of polymers in bulk water and adsorbed onto hydrophobic and hydrophilic substrates.

polymer	bulk water or surface type	$\mu_{\mathrm{mono}}/$ 10^{10} (s/kg)	Ref.
peptide[a]	bulk water	94	[115]
peptide	bulk water	90	this work
ds-DNA[b]	bulk water	4.7	[116]
peptide	on hydrophobic diamond	30	this work
PEG[c]	on hydrophobized silica (SAM)	8.0	[72, 73]
ds-DNA	on cationic lipid bilayer	1.2	[70, 71]
peptide	on hydrophilic diamond	< 0.9	this work
ds-DNA	on mica	0.17	[74]

[a] mobility of 15mer is calculated using the scaling law given in Ref. [115] with the molar mass of the polypeptide used here, $M_{\mathrm{r}} = 1298\,\mathrm{g/mol}$; scaling from polymer to monomer mobility is in all cases done via $\mu_{\mathrm{mono}} = N\mu$ except for [b] $\mu_{\mathrm{mono}} = N^{0.57}\mu$ and [c] $\mu_{\mathrm{mono}} = N^{3/2}\mu$

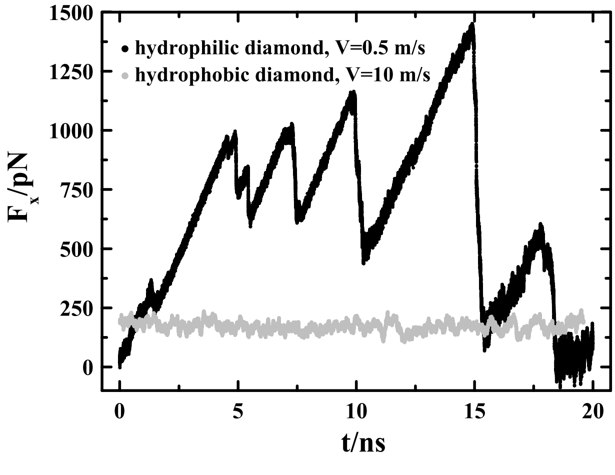

Figure 3.12: Time evolution of the friction forces F_x on a polypeptide pulled laterally over a hydrophobic H-terminated diamond surface (grey) and over a hydrophilic 50 % OH-terminated diamond surface (black) as obtained from MD simulations. Pulling speeds are $V = 10\,\mathrm{m/s}$ and $V = 0.5\,\mathrm{m/s}$, respectively.

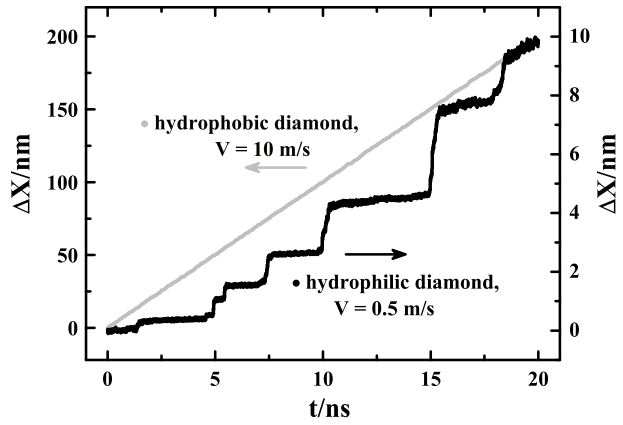

Figure 3.13: Time evolution of the displacement of the first amino acid center of mass ΔX where the polypeptide is pulled laterally over a hydrophobic H-terminated diamond surface (grey, left axis) and over a hydrophilic 50 % OH-terminated diamond surface (black, right axis). Pulling speeds are $V = 10\,\mathrm{m/s}$ and $V = 0.5\,\mathrm{m/s}$, respectively. Traces correspond to those shown in Fig. 3.12. On time and length scales smaller than presented here or for smaller velocities, the motion over the hydrophobic substrate is still smooth and in strong contrast to the observed stick-slip motion over the hydrophilic surface.

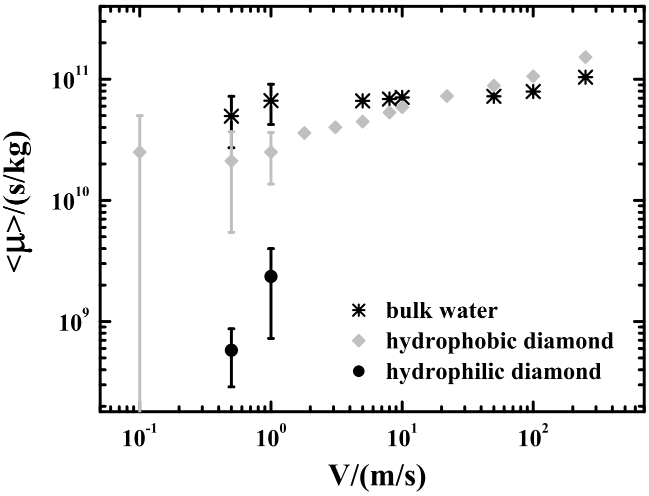

Figure 3.14: Average polypeptide (15mer) mobilities $\langle \mu \rangle$ as obtained by MD simulations for different pulling speeds V. Data are taken in bulk water (crosses), on a hydrophobic diamond surface (grey diamonds), and on a hydrophilic diamond surface (black circles). Error estimates are only shown when larger than the symbol size.

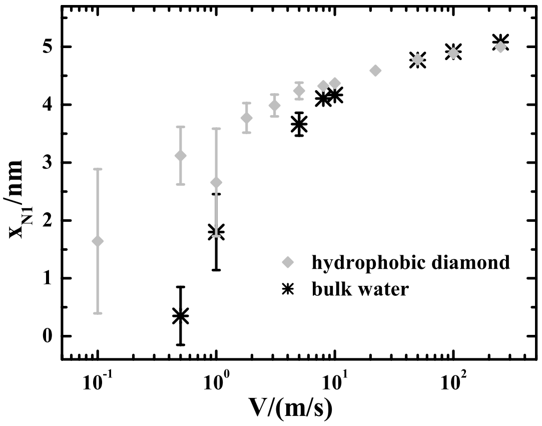

Figure 3.15: Average polypeptide (15mer) end-to-end extension x_{N1} as obtained by MD simulations for different pulling speeds V. Data are taken in bulk water (crosses) or on a hydrophobic diamond surface (grey diamonds). Error estimates are only shown when larger than the symbol size.

hence large conformational fluctuations. This is confirmed by the observation that the extension x_{N1} increases sharply and shows much smaller fluctuations at about $V > 1\,\mathrm{m/s}$ as depicted for the bulk case (crosses) and the hydrophobic surface (grey diamonds) in Fig. 3.15. Similarly, both the fluctuations and the value of the radius of gyration perpendicular to both the pulling direction and the surface normal, $R_g^y = [\frac{1}{N}\sum_{i=1}^{N}(Y_i - \langle Y \rangle)^2]^{1/2}$, decrease at $V \approx 1\,\mathrm{m/s}$ for pulling in bulk water, and at $V \approx 10\,\mathrm{m/s}$ for the hydrophobic surface as can be seen in Fig. 3.16, coded using the same symbols. In all cases, the monomer positions $\boldsymbol{R}_i = (X_i, Y_i, Z_i)$ are represented by the position vectors of the C_α atom of each of the $N = 15$ amino acids. The change in preferred conformations is reflected in simulation snapshots shown in Fig. 3.17 with a representative surface conformation each for $V = 1\,\mathrm{m/s}$ and $V = 10\,\mathrm{m/s}$. Note that irrespective of the pulling speed, the polymer is strongly adsorbed to the surface in a flat configuration with water molecules completely replaced in that surface region by the peptide. The time- and number-averaged height of the C_α atoms as measured by their distance from the first peak in the diamond C atom density profile is given by $\langle Z \rangle_{\mathrm{phob}} = (0.45 \pm 0.02)\,\mathrm{nm}$ and does *not* considerably depend on the pulling speed in the range investigated here.

The dissipation mechanism on the hydrophobic surface is analyzed in more detail by splitting the total force on the polypeptide into solvent and surface contributions as described above. For low pulling speeds $V \leq 1\,\mathrm{m/s}$, insufficient statistics prohibit a more detailed analysis. Limiting our considerations to velocities $V \geq 1.8\,\mathrm{m/s}$, it is seen that both the hydrophobic surface as well as the solvent molecules contribute in a dissipative way. The relative contribution of the surface (left axis) and the water molecules (right-hand side axis) is shown in Fig. 3.18. With increasing velocity the surface contribution to friction decreases from about 50 % at $V = 1.8\,\mathrm{m/s}$

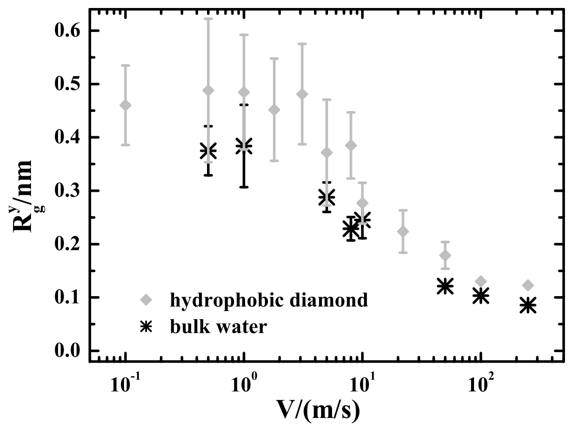

Figure 3.16: Average polypeptide (15mer) radius of gyration in $\hat{y}$ direction, R_g^y, as obtained by MD simulations for different pulling speeds V. The $\hat{y}$ direction is normal to both the pulling direction $\hat{x}$ and the surface normal $\hat{z}$. Data are taken in bulk water (crosses) or on a hydrophobic diamond surface (grey diamonds). Error estimates are only shown when larger than the symbol size.

down to 5 % at $V = 250\,\mathrm{m/s}$. Considering the only small change in the mobility for even smaller pulling velocities, $V \leq 1.8\,\mathrm{m/s}$, we anticipate the friction in the linear response regime on a hydrophobic surface to originate about half from direct interactions with the surface, and half from peptide-solvent interactions. Despite the fact that in the linear response regime the mobility on the hydrophobic substrate is only reduced by a factor of three with respect to the bulk water case we conclude that the surface *directly* adds to friction effects on the peptide. Interestingly, the friction of the adsorbed peptide mediated by water molecules decreases at high velocities as compared with the bulk water case. For $V = 50\,\mathrm{m/s}$ we get a dissipative power by the surrounding water molecules of $\mathcal{P}_{\mathrm{phob}}^{\mathrm{H_2O}} = 26\,\mathrm{nW}$ on the hydrophobic surface and $\mathcal{P}_{\mathrm{bulk}}^{\mathrm{H_2O}} = 33\,\mathrm{nW}$ in bulk water. For $V = 250\,\mathrm{m/s}$ we find $\mathcal{P}_{\mathrm{phob}}^{\mathrm{H_2O}} = 370\,\mathrm{nW}$ and $\mathcal{P}_{\mathrm{bulk}}^{\mathrm{H_2O}} = 560\,\mathrm{nW}$. Hence the water contribution to friction on a hydrophobic surface drops from 79 % to 68 % of the friction in bulk water for $V = 50\,\mathrm{m/s}$ and $V = 250\,\mathrm{m/s}$, respectively. This decrease is possibly due to geometric effects reflecting a decrease of the contact area between the polypeptide and the water at larger pulling speeds and thus an effective lubrication layer brought about by the presence of the hydrophobic surface.

At the hydrophilic surface the situation is quite different as the peptide is strongly stretched and its extension amounts to $R_x \geq 4\,\mathrm{nm}$ even for pulling speeds as low as $V = 0.5\,\mathrm{m/s}$ and $1\,\mathrm{m/s}$. The pronounced fluctuations and hence relative uncertainties in the mobility are based firstly on the stick-slip nature of the motion and secondly on the desorption and adsorption of small parts of the peptide. This is demonstrated in Fig. 3.19a) where the time evolution of the average height of the peptide C_α atoms, $\langle Z \rangle_{\mathrm{phil}}$, as measured by their distance from the O atom peak in

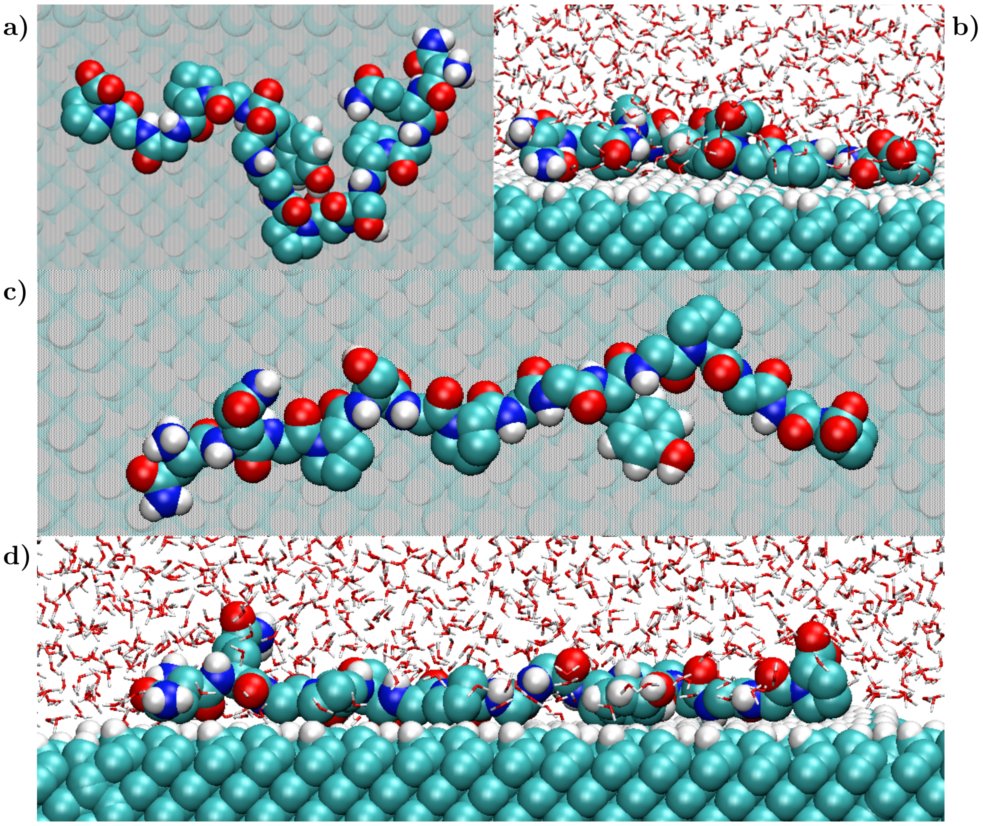

Figure 3.17: Representative conformations of a polypeptide chain adsorbed onto a hydrophobic diamond surface for two different lateral pulling speeds; **a)** and **b)** top and side view at $V = 1\,\mathrm{m/s}$, **c)** and **d)** top and side view at $V = 10\,\mathrm{m/s}$. At low pulling speeds $V \leq 1\,\mathrm{m/s}$, the 15mer coils up, see **a)** and also Figs. 3.15 and 3.16; at higher pulling speeds it adopts a stretched configuration, see **c)** and **d)**. Note that in all cases the polymer effectively replaces water molecules directly bound to or located at the surface and is hence tightly bound to the surface at a distance of about $\langle Z \rangle_{\mathrm{phob}} = 0.45\,\mathrm{nm}$, see text for details.

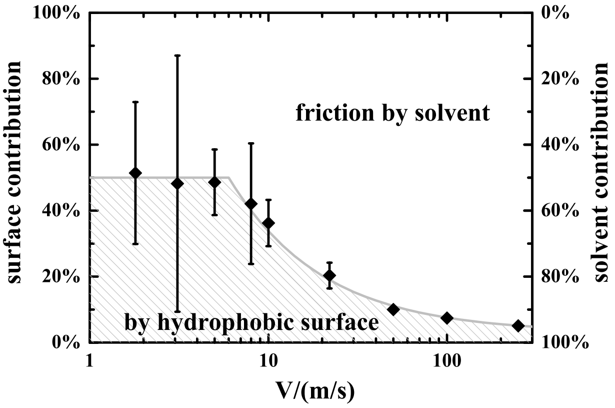

Figure 3.18: Separation of the frictional forces and the dissipative power into surface and solvent contributions for a polypeptide dragged over a hydrophobic diamond surface as a function of the pulling velocity V. Relative contribution of the surface is shaded and indicated on the left axis, for solvent contribution see axis on the right-hand side. The shading and the line are drawn to guide the eye. For velocities $V \leq 1\,\mathrm{m/s}$, poor statistics prevent a splitting of the contributions.

the substrate density profile, (black data points, left axis) is plotted together with the corresponding displacement trace (grey, right-hand side axis) for $V = 0.5\,\mathrm{m/s}$. In equilibrium and during the beginning of pulling, any water is driven away from the interface and the polypeptide is adsorbed flat onto the surface with a mean height of about $\langle Z \rangle_{\mathrm{phil}} \approx 0.34\,\mathrm{nm}$. When pulling, partial desorption events coincide with slip instabilities and point to the rupture of adhesive bonds. This interpretation is confirmed by the time evolution of the number of hydrogen bonds between the surface hydroxyl groups and the polypeptide, n_{HB}, as shown in Fig. 3.19b). Again, also the displacement trace is shown. On the other hand, the number of hydrogen bonds between peptide and water molecules stays rather constant over time at 55±3. The decline in the number of hydrogen bonds with the surface atoms confirms our interpretation that neither a steady state nor the linear response regime have been reached for the hydrophilic substrate simulations and only an upper bound of the mobility can be given. Note that partial de- and subsequent adsorption of the polymer is probable even in the linear response limit, $V \to 0$, but does not lead to total desorption, especially for long enough polymers as will be discussed in Section 4.5. Finally, we present the force and displacement traces for the hydrophilic substrate and $V = 0.5\,\mathrm{m/s}$ already shown in Figs. 3.12 and 3.13 together in Fig. 3.19c), again emphasizing the mutual timewise cross-correlation of force peaks, the stick-slip motion, hydrogen bond breaking, and partial desorption, see Fig. 3.19a)-c).

An analysis of the total forces exerted on the peptide molecule by atoms belonging either to the surface, F_x^{surf}, or to water molecules, $F_x^{\mathrm{H_2O}}$, shows that these forces are approximately Gaussian distributed. For pulling the peptide with a speed of $V = 0.5\,\mathrm{m/s}$ over the hydrophilic surface, these forces average to $\langle F_x^{\mathrm{surf}} \rangle = 620\,\mathrm{pN}$

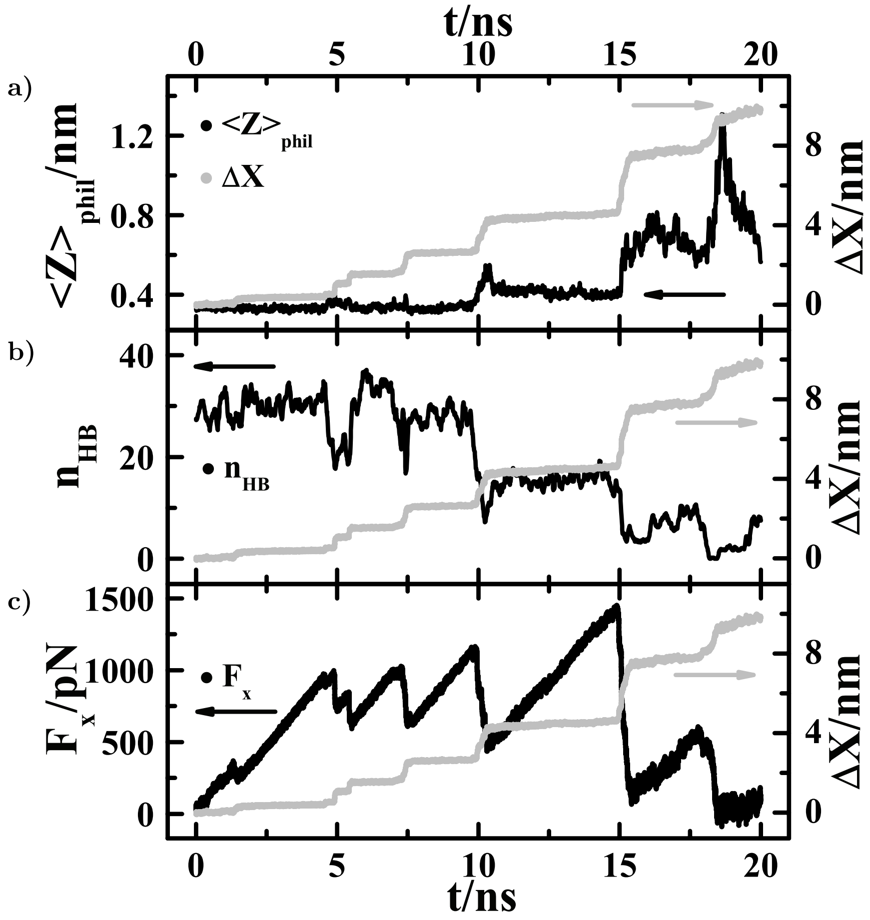

Figure 3.19: Mutual time cross-correlation between the average polymer height, the number of hydrogen bonds with the substrate, the friction force peaks and the stick-slip nature of motion for a polypeptide dragged over a hydrophilic diamond surface. In all cases, the displacement of the center of mass of the first amino acid, ΔX, is shown in grey and on the right-hand side axis as a function of time. The left axis denotes **a)** the number averaged height of the C$_\alpha$ atoms, $\langle Z \rangle_{\text{phil}}$, **b)** the number of hydrogen bonds between the polypeptide and the surface hydroxyl groups, n_{HB}, and **c)** the total frictional force exerted by the cantilever spring, F_x, which in each case is shown in black. The number of hydrogen bonds is smoothed using a moving average method over ten adjacent data points. Abrupt changes, *i.e.* partial desorption events noted by a height increase or a decrease in the number of hydrogen bonds, by force peaks or slip events occur in a concerted fashion.

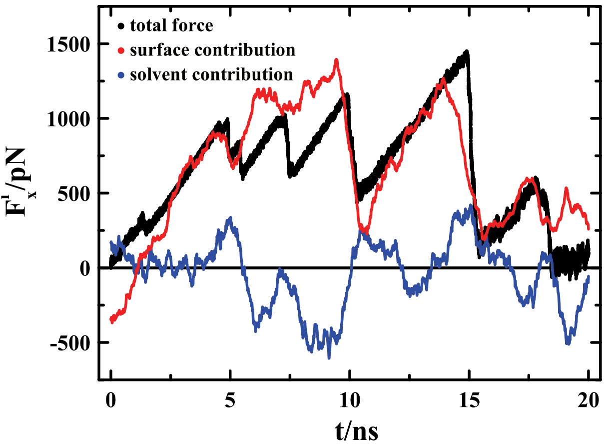

Figure 3.20: Separation of the total frictional force, F_x, (black) into surface F_x^{surf} (red) and solvent $F_x^{\mathrm{H_2O}}$ (blue) contribution for a polypeptide dragged over a hydrophilic diamond surface as a function of the simulation time t. The pulling velocity is $V = 0.5\,\mathrm{m/s}$. The contributions of the surface and the water are smoothed using a moving average method over 100 adjacent data points.

and $\langle F_x^{\mathrm{H_2O}}\rangle = -34\,\mathrm{pN}$. However, the force contributions are governed by enormous fluctuations with standard deviations of $\sigma(F_x^{\mathrm{surf}}) = 1.6\,\mathrm{nN}$ and $\sigma(F_x^{\mathrm{H_2O}}) = 2.5\,\mathrm{nN}$. Using a moving average method over 100 adjacent data points for $\langle F_x^{\mathrm{surf}}\rangle$ and $\langle F_x^{\mathrm{H_2O}}\rangle$ reveals that the major dissipative contribution indeed stems from peptide-surface interactions. The solvent contribution rarely makes up more than 30 % of the total interaction force F_x, and, more interestingly, mostly acts in a non-dissipative, ‘pushing’ way, as can be seen in more detail in Fig. 3.20. There we plot the total dissipative force F_x in black, the surface contribution, F_x^{surf}, in red, and the solvent contribution, $F_x^{\mathrm{H_2O}}$, in blue. Note that the contributions $F_x^{\mathrm{H_2O}}$ and F_x^{surf} only add to the total force F_x after time averaging which is due to inertial effects. A qualitatively similar picture is obtained for the simulation at $V = 1\,\mathrm{m/s}$. At even higher velocities the peptide desorbs irreversibly a possible cause of which will be discussed in more detail in Section 4.5. The interpretation of hydrogen bond ruptures as the main source of friction is supported by simulation movies and snapshots. In Fig. 3.21 we present snapshots of the peptide pulled at $V = 0.5\,\mathrm{m/s}$ taken at simulation times of $t = 7.0\,\mathrm{ns}$ and $t = 17.7\,\mathrm{ns}$. It is seen that hydrogen bond donor and acceptor atoms both in the backbone of the peptide and the side chains participate in hydrogen bonding.

Summarizing our results, polypeptides experience high lubricity on hydrophobic surfaces with mobilities close to those in bulk water. Even so, friction is generated by interactions of the peptide molecule with both the solvent and the surface atoms. In contrast, for a hydrophilic surface hydrogen bonds transiently lock the peptide leading to a stick-slip type of motion and to mobility coefficients orders of magnitude lower than in the bulk water and the hydrophobic surface cases. With current

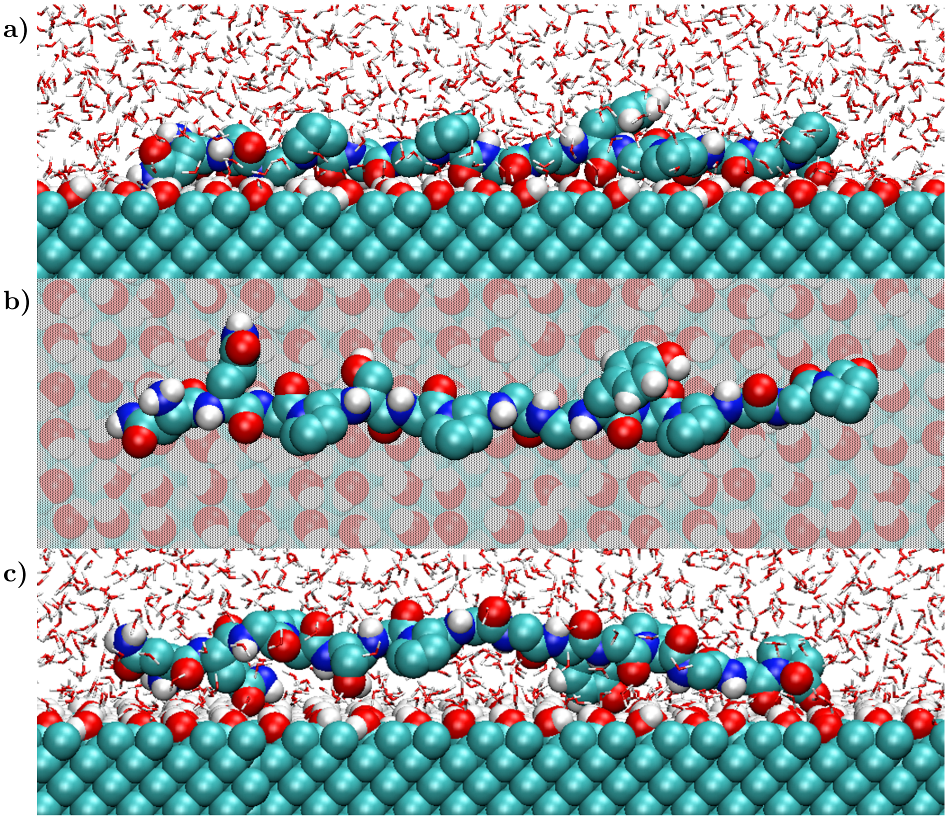

Figure 3.21: Representative conformations of a polypeptide chain adsorbed onto a hydrophilic diamond surface and laterally pulled at $V = 0.5\,\mathrm{m/s}$ at simulation time $t = 7.0\,\mathrm{ns}$ (**a)** side and **b)** top view), and **c)** at time $t = 17.7\,\mathrm{ns}$ (side view). Hydrogen bonds are formed between surface hydroxyl groups and hydrogen bond acceptors or donors in both the polypeptide backbone and the side chains. For lateral pulling on the hydrophilic substrate the pulling velocities are comparably large and beyond the linear response regime. Hence a stationary state is not reached but instead partial desorption occurs, see also Fig. 3.19.

computational resources, hydrophilic friction can be probed in atomistic simulations including solvent molecules only in the non-linear regime. As opposed to peptides adsorbed on hydrophobic diamond surfaces, simulations cannot reach the linear response regime or equilibration. The difference in polymer surface friction between hydrophobic and hydrophilic substrates has numerous consequences for the dynamics of polymer adsorption, but also for the interior dynamics of peptides. Specifically, one can speculate that the kinetics of the initial stage of protein collapse, which is driven by hydrophobic attraction, is accelerated because of the small friction forces involved.

Chapter 4

Non-equilibrium adsorption of single polymers

Non-equilibrium adsorption of polymers is characterized by the behavior of a polymer close to an adsorbing surface when either very long timescales in *e.g.* diffusion or binding and unbinding processes prohibit a full equilibration of the system on typical experimental or simulation timescales or when energy dissipation occurs by some external force or field. In contrast to equilibrium adsorption as discussed in Chapter 2 and the references given there, non-equilibrium adsorption of polymers is by far less well studied, even in the dilute or single polymer regime. This is rather surprising since many technological applications of polymer adsorption are in some way accompanied with dissipative processes, such as strong stirring of solutions or convection as outlined in Section 1.1. A very important aspect of non-equilibrium adsorption is given by the adsorption under shear flow which at the same time is the best studied case both from the experimental [117–126] and the theoretical point of view [127–133].

To point out the importance of far-from-equilibrium effects we investigate a simple and educative case in Section 4.2, namely a single polymer that is pulled laterally over an adsorbing surface by a force exerted at one end. Experimentally this scenario is accessible through the use of the AFM and tweezers techniques [61, 134] by which also pulling polymers parallel to a surface has been achieved [75]. Using the conclusions from lateral pulling, the adsorption in simple shear flow is studied in Section 4.3, which is a generic situation for adsorbing surfaces in sheared solutions as found in *e.g.* processing of colloidal solutions. A related scenario is a laterally moving, dilute polymer brush that is pushed against a solid substrate [10]. The influence of hydrodynamic interactions, which are excluded in the parts before for systematic reasons, is examined in Section 4.4. Finally, the adsorption of a single particle on a corrugated surface under a lateral force is analyzed and its implications on the polymer case are discussed in Section 4.5. The chapter starts with an analysis of conformational changes of polymers under external flow fields, Section 4.1. The polymer model used in this chapter is the same as that introduced for BD simula-

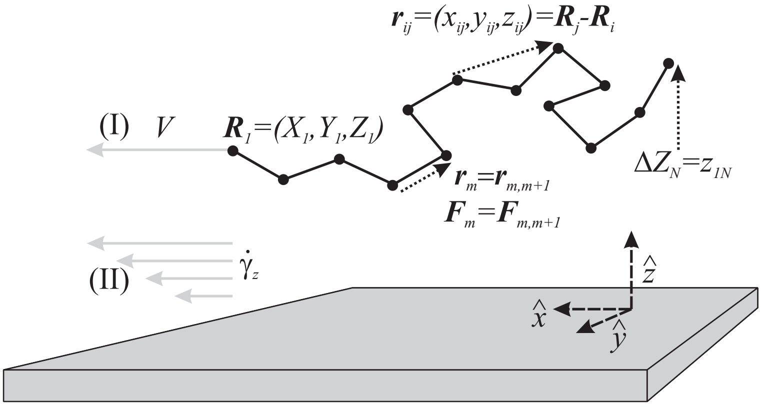

Figure 4.1: The coarse-grained polymer model as used for (non)equilibrium adsorption and bulk flow deformation. For polymer adsorption, the $\hat{z}$ axis always coincides with the surface normal. The position of monomer i is denoted as $\boldsymbol{R}_i = (X_i, Y_i, Z_i)$, the distance between two monomers i and j as $\boldsymbol{r}_{ij} = (x_{ij}, y_{ij}, z_{ij}) = \boldsymbol{R}_j - \boldsymbol{R}_i$. Nearest neighbor bond vectors are abbreviated as $\boldsymbol{r}_m = \boldsymbol{r}_{m,m+1}$. Similarly, the force acting on the mth bond is defined as $\boldsymbol{F}_m = \boldsymbol{F}_{m,m+1}$ where $\boldsymbol{F}_{m,m+1}$ is the force exerted by monomer $m+1$ on monomer m. The end-to-end height difference is $\Delta Z_N = z_{1N}$. Also shown are two cases of non-equilibrium adsorption, Case (I) in which a polymer is pulled at one end in $\hat{x}$ direction through solution and Case (II) in which a simple shear flow in $\hat{x}$ direction acts with a velocity gradient in $\hat{z}$ direction of $\dot{\gamma}_z$.

tions of equilibrium adsorption, cf. Section 2.3. The definition of symbols is shown in Fig. 4.1.

4.1 Polymer response to flow fields in bulk solution

In this section we develop some simple arguments for the response of a polymer to simple flow fields in bulk solution. The results are later applied to the situation of a polymer close to an adsorbing surface. The deformation of polymers in flows has gained much interest both from the experimental and the theoretical side [63, 64, 135, 136]. Even in the absence of turbulence and in the zero Reynolds number limit many studies employing simulations as well as continuum theories have been used to tackle this issue for all kinds of flows, *e.g.* purely elongational and purely rotational flows or combinations thereof as in simple shear flow, or plug flows just to mention a few. Focusing solely on observables that will later turn out to be important for polymer adsorption we extend these studies by the treatment of a polymer in the flow field caused (I) by applying a unidirectional force on one end of a polymer and pulling it through solution, and (II) by exerting a simple shear flow with a constant shear rate in one direction, see also Fig. 4.1. Here we assume the polymer to be located in bulk solution and hence at the moment neglect the effects of a surface.

In addition excluded volume interactions are neglected in the analytical treatment. This formulation is even appropriate for the case of more realistic polymer models with excluded volume interactions if the flow field perturbations are strong enough. In that case the polymer is mostly stretched and monomer interactions between non-nearest neighbors occur rarely.

Starting point for the more general Case (II) of a polymer consisting of N monomers in shear flow, is the overdamped Langevin equation for the position of monomer bead i, $\boldsymbol{R}_i$,

$$\vec{0} = \boldsymbol{\zeta}_i + \boldsymbol{F}_{\text{fric}} + \boldsymbol{F}_{i,i-1} + \boldsymbol{F}_{i,i+1} \,, \tag{4.1}$$

where $\boldsymbol{F}_{\text{fric}} = (\dot{\boldsymbol{R}}_i - \boldsymbol{v}(\boldsymbol{R}_i))/\mu$ is the friction force on monomer i against the solvent fluid field with velocity $\boldsymbol{v}(\boldsymbol{R}) = \dot{\boldsymbol{\gamma}} \cdot \boldsymbol{R}$ at position $\boldsymbol{R}$. As in Rouse dynamics, μ is the bulk mobility of the monomer which is supposed to be constant over space and monomer index and, in particular, independent of the other monomer positions and velocities (cf. Section 1.2), and $\dot{\boldsymbol{\gamma}}$ is the shear field tensor. The last two terms are the vectorial forces of monomers $i-1$ and $i+1$ on monomer i. Rearranging we obtain

$$\dot{\boldsymbol{R}}_i/\mu = \boldsymbol{\zeta}_i + \dot{\boldsymbol{\gamma}}'\boldsymbol{R}_i + \boldsymbol{F}_{i,i-1} + \boldsymbol{F}_{i,i+1} \,, \tag{4.2}$$

where in the dashed shear tensor all components are divided by μ. In the case of simple shear flow we write

$$\boldsymbol{v}(\boldsymbol{R}_i) = \dot{\boldsymbol{\gamma}}\boldsymbol{R}_i = (\dot{\gamma}_z Z_i, 0, 0) \,. \tag{4.3}$$

By time averaging the random contribution in Eq. (4.2) vanishes. The surviving terms in the $\hat{x}$ direction are given by

$$\left\langle \dot{X}_1 \right\rangle/\mu = \dot{\gamma}_z \left\langle Z_1 \right\rangle/\mu + F_1 \,, \tag{4.4}$$

$$\left\langle \dot{X}_i \right\rangle/\mu = \dot{\gamma}_z \left\langle Z_i \right\rangle/\mu - F_{i-1} + F_i \quad \text{for } 2 \le i \le N-1\text{, and} \tag{4.5}$$

$$\left\langle \dot{X}_N \right\rangle/\mu = \dot{\gamma}_z \left\langle Z_N \right\rangle/\mu - F_{N-1} \,. \tag{4.6}$$

Here F_j is the short-hand notation of the averaged force in $\hat{x}$ direction exerted by monomer $j+1$ on monomer j, $F_j \equiv \langle (\boldsymbol{F}_j)^x \rangle = \langle (\boldsymbol{F}_{j,j+1})^x \rangle$. By using the fact that after averaging over a long enough time period the monomer velocities must be equal, $\langle \dot{X}_i \rangle = \langle \dot{X}_j \rangle$, we get a set of $N-1$ equations each of which is the right-hand side of Eqs. (4.5), (4.4), or (4.6). Hence we can rearrange each equation to solve for an unknown force. To give two examples, using the equations for $i=1$ and $i=2$, and solving for F_2 yields $F_2 = 2F_1 + \dot{\gamma}_z \langle Z_1 - Z_2 \rangle/\mu$. Similarly we obtain for the third bond, $F_3 = 2F_2 - F_1 + \dot{\gamma}_z \langle Z_2 - Z_3 \rangle/\mu = 3F_1 + \dot{\gamma}_z \langle 2Z_1 - Z_2 - Z_3 \rangle/\mu$. The general equation for $1 \le i \le N-1$ turns out to be

$$F_i = iF_1 - \frac{\dot{\gamma}_z}{\mu} \sum_{j=1}^{i} \langle \Delta Z_j \rangle \,, \tag{4.7}$$

where we defined $\Delta Z_j = Z_j - Z_1$. Using Eqs. (4.7), (4.6), and (4.5) for bond $N-2$ we can now eliminate F_1 and obtain for the force on bond i with $1 \leq i \leq N-1$

$$F_i = \frac{\dot{\gamma}_z}{\mu} \left(\frac{i}{N} \sum_{j=1}^{N} \langle \Delta Z_j \rangle - \sum_{j=1}^{i} \langle \Delta Z_j \rangle \right) . \tag{4.8}$$

To check consistency, the mean polymer velocity can be calculated by *e.g.* Eq. (4.4) and yields the expected result $V \equiv \langle \dot{X}_1 \rangle = \frac{\dot{\gamma}_z}{\mu N} \sum_{j=1}^{N} \langle Z_j \rangle$.

For pulling a polymer at its first monomer through bulk solution, Case (I), we can simply set the shear rate to zero, $\dot{\gamma}_z = 0$, or equivalently the solvent flow field, $\boldsymbol{v}(\boldsymbol{R}_i) = 0$. Also the equation of motion for the first monomer is modified to take the pulling force F which acts in $\hat{x}$ direction into account such that Eq. (4.4) becomes

$$\left\langle \dot{X}_1 \right\rangle / \mu = F_1 + F \, . \tag{4.9}$$

A similar approach as described above and elimination of the force on the last bond $N-1$ yields the force on any bond i as

$$F_i = (N-i) F_{N-1} = -\frac{N-i}{N} F \, . \tag{4.10}$$

Hence, the mean force on the bonds linearly decays from $F(N-1)/N$ at the pulled end down to F/N at the other end. The average velocity of the polymer is given by $V = \mu F/N$ consistent with a Rouse picture.

In the following we calculate the roughness of the polymer perpendicular to the direction of the external forces which are caused by either pulling or shearing. For simplicity, we switch from the general discussion in the previous paragraphs to a FJC polymer model. To further proceed we assume the mean forces calculated above, $\langle \boldsymbol{F}_j \rangle = (F_j, 0, 0)$, as the variable of control. By neglecting fluctuations in any direction $\hat{x}$, $\hat{y}$, and $\hat{z}$, the Gibbs ensemble, for which the force extension relations are simple, becomes the relevant ensemble. Setting forces in the $\hat{z}$ direction identical zero is an approximation for the shear case since torsional components and tumbling do arise. For both the shear and the pulling case another approximation is later given by the neglect of the adsorbing surface which breaks the symmetry between the lateral $\hat{y}$ and $\hat{z}$ directions. Nevertheless the results later turn out to be of appealing simplicity, and excellently describe the simulation data. Note that a more detailed description and introduction into polymer models and specifically the FJC can be found in Section 5.1.

For a FJC under force control, *i.e.* in a Gibbs ensemble [92], the polymer partition function factorizes into $N-1$ partition functions of single FJC bonds, $\mathcal{Z}$, each evaluating to [93]

$$\mathcal{Z}(\tilde{F}_i) = \tilde{F}_i^{-1} \sinh \tilde{F}_i \, , \tag{4.11}$$

where we introduced rescaled forces $\tilde{F}_i = F_i a / k_\mathrm{B} T$. The standard result for the mean extension along the pulling direction is obtained by taking the logarithmic derivative, $\langle \tilde{x}_i \rangle \equiv \langle \tilde{X}_{i+1} - \tilde{X}_i \rangle = \partial \ln \mathcal{Z} / \partial \tilde{F}_i = \mathcal{L}(\tilde{F}_i)$ where $\mathcal{L}(x) = \coth x - x^{-1}$ is the Langevin function. The second moment is given by a double derivative, $\langle \tilde{x}_i^2 \rangle = \mathcal{Z}^{-1} \partial^2 \mathcal{Z} / \partial \tilde{F}_i^2 = 1 - 2\mathcal{L}(\tilde{F}_i)/\tilde{F}_i$. The two perpendicular directions, $\hat{y}$ and $\hat{z}$, are equivalent and the mean squared extension perpendicular to the pulling direction is

$$\left\langle \tilde{z}_i^2 \right\rangle = \left(1 - \left\langle \tilde{x}_i^2 \right\rangle\right)/2 = (\coth \tilde{F}_i - \tilde{F}_i^{-1})/\tilde{F}_i = \tilde{\mathcal{L}}(\tilde{F}_i)\,, \tag{4.12}$$

where we have defined a new function $\tilde{\mathcal{L}}(x) = \mathcal{L}(x)/x$. We are particularly interested in the height difference between the pulled end of the chain and monomer i, $\Delta \tilde{Z}_i \equiv \tilde{Z}_i - \tilde{Z}_1 = \sum_{j=1}^{i-1} \tilde{z}_j$. Since all bonds are decorrelated from each other we obtain for its second moment

$$\left\langle \Delta \tilde{Z}_i^2 \right\rangle = \left\langle \left(\sum_{j=1}^{i-1} \tilde{z}_j \right)^2 \right\rangle = \sum_{j=1}^{i-1} \left\langle \tilde{z}_j^2 \right\rangle = \sum_{j=1}^{i-1} \tilde{\mathcal{L}}(\tilde{F}_j) \approx \int_{1/2}^{i-1/2} \mathrm{d}j\, \tilde{\mathcal{L}}(\tilde{F}_j)\,. \tag{4.13}$$

Let us examine the two limits of very strong and weak pulling in more detail. For weak pulling, $\tilde{F}_i = \tilde{F}(N-i)/N \le \tilde{F}_1 < 1$, we can use the asymptotic limit $\tilde{\mathcal{L}}(x) \xrightarrow{x \ll 1} 1/3$. On the other hand, for very strong pulling, $1 < \tilde{F}_i \le \tilde{F}_1$, we have $\tilde{\mathcal{L}}(x) \xrightarrow{x \gg 1} 1/x$. In summary we get

$$\left\langle \Delta \tilde{Z}_i^2 \right\rangle \longrightarrow \begin{cases} (i-1)/3 & \text{for } \tilde{F}_1 < 1 \text{ and} \\ \frac{N}{\tilde{F}} \ln \frac{N-1/2}{N-i+1/2} \xrightarrow[1 \ll N]{i \ll N} (i-1)/\tilde{F} & \text{for } 1 < \tilde{F}_i \le \tilde{F}_1. \end{cases} \tag{4.14}$$

Hence, for weak pulling we recover the standard random walk result and the mean squared extension scales linearly with the number of bonds $i-1$. For strong pulling, on the other hand, the mean squared extension is still linear in $i-1$ but proportional to the inverse force. This can be interpreted as an effective renormalized Kuhn length in $\hat{z}$ direction given by $a_{\text{eff}} = (3/\tilde{F})^{1/2} a$. For intermediate pulling forces, $\tilde{F}_i < 1 < \tilde{F}_1$, the situation is more complex with trumpet and stem-flower regimes as discussed in the literature [136]. It is useful to define the mean, renormalized Kuhn length as

$$a_{\text{eff}} = \left(\frac{3 \left\langle \Delta \tilde{Z}_N^2 \right\rangle}{N-1} \right)^{1/2} a\,, \tag{4.15}$$

where $\langle \Delta \tilde{Z}_N^2 \rangle$ is defined by Eq. (4.13).

For illustration we show in Fig. 4.2 characteristic simulation snapshots of a 32mer pulled in bulk with rescaled velocities of $\tilde{V} = Va/k_{\mathrm{B}}T\mu = 0$, 0.1, and 1. In Fig. 4.3 we show simulation data for the rescaled mean squared perpendicular extension, $3\langle \Delta \tilde{Z}_N^2 \rangle/(N-1)$, as a function of the pulling speed $\tilde{V}$ for a 64mer both with (black circles) and without excluded volume (grey diamonds, Lennard-Jones parameter $\epsilon = 0$). The numerical solution to Eq. (4.13) is shown as a solid line. For pulling with $\tilde{V} \ge 1$ both polymer models coincide due to alignment of the chain. At lower pulling rates excluded-volume interactions become relevant and the self-avoiding

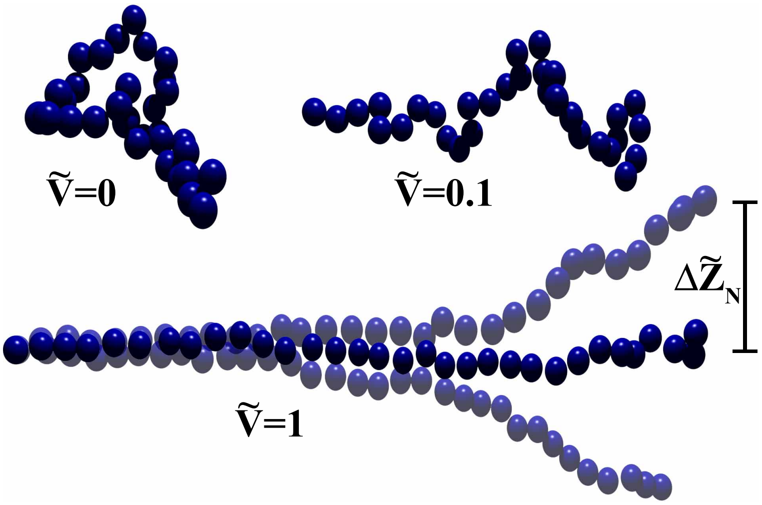

Figure 4.2: Simulation snapshots for pulling a 32mer through bulk solution to the left with increasing velocity $\tilde{V} = Va/k_\mathrm{B}T\mu$. Also shown is the definition of $\Delta\tilde{Z}_N$.

polymer is more swollen than the phantom chain. It transpires that Eq. (4.13) is accurate for large enough pulling forces.

In the following sections the non-equilibrium adsorption of a single, non-grafted pulled or sheared polymer will be discussed. We start with the simpler problem (I) in which the polymer is pulled with a constant velocity at one end.

4.2 Laterally pulled polymers

For the situation (I) where the first monomer of the polymer is pulled with a constant velocity $\dot{X}_1 = V$ parallel to the surface, we determine the overcritical adsorption potential as described for the equilibrium case in Section 2.3. In the $\hat{z}$ direction, *i.e.* normal to the surface, the first monomer is moving without constraints according to Eq. (2.37). We use rescaled velocities in the range of $10^{-4} \leq \tilde{V} = Va/k_\mathrm{B}T\mu \leq 100$. For higher pulling velocities and larger polymers, $N\tilde{V} \geq 100$, the spring constant $\tilde{k}$ is increased sufficiently so that all bond lengths are well below $1.15\,a$. The other parameters such as the time step and the number of simulation steps are adjusted accordingly.

For pulled polymers, we observe stronger attachment of the chains to the surface. This is demonstrated for a 128mer in Fig. 4.4 where we plot the mean normalized adsorption potential $\tilde{W} = -\langle\tilde{U}^\mathrm{surf}\rangle/N\chi$ as a function of the interaction parameter χ and compare the equilibrium case (filled circles) with pulling at $\tilde{V} = 1$ (open diamonds). Clearly, the (over)critical adsorption strength is decreased by pulling. We associate this enhanced adsorption with the flattening of the chain in the $\hat{z}$ direc-

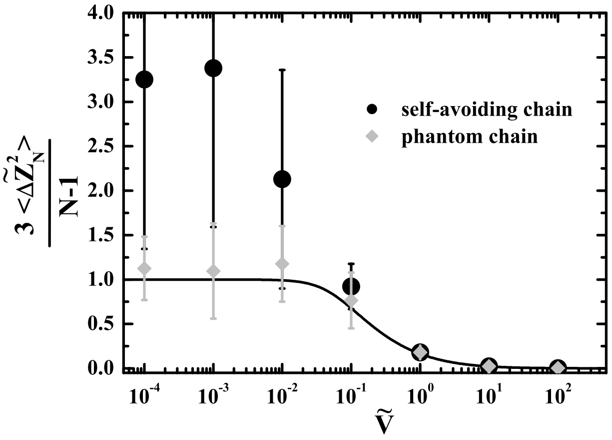

Figure 4.3: Rescaled mean squared perpendicular extension $3\langle\Delta\tilde{Z}_N^2\rangle/(N-1)$ for pulling a self-avoiding polymer (black circles) and a phantom chain (no excluded volume, grey diamonds) with $N = 64$ at different velocities $\tilde{V} = Va/k_\mathrm{B}T\mu$ through bulk solution. For $\tilde{V} \geq 1$ the results for the two models coincide, for $\tilde{V} \leq 0.1$ the self-avoiding chain swells strongly. Also shown is the numerical solution to (4.13).

tion perpendicular to the surface. To test this hypothesis we conduct simulations at different velocities and extract the overcritical adsorption strength. In Fig. 4.5 we show the overcritical adsorption strengths normalized by the values at equilibrium $\chi^\mathrm{ocrit}(\tilde{V})/\chi^\mathrm{ocrit}_\mathrm{eq}$ as a function of the pulling speed. Presented are three models of 64mers: (i) the self-avoiding polymer as described in the simulation details, (ii) the phantom chain, *i.e.* without excluded volume ($\epsilon = 0$), and (iii) a Gaussian chain without excluded volume and with ideal chain elasticity $\tilde{U}^\mathrm{poly} = 3/2\sum_i \tilde{r}_i^2$. The results presented in Fig. 4.5 show no influence of the pulling force on the Gaussian chain; this is easily understood since the chain conformations in the pulling direction $\hat{x}$ are decoupled from the polymer fluctuations in the $\hat{z}$ direction perpendicular to the surface, clearly an artifact of the ideal chain model. In contrast, we observe stronger adsorption for the FJC model, where the orthogonal bond directions are coupled as in a real polymer chain. It turns out that there is hardly any effect by excluded volume interaction. For the non-rescaled values of the critical adsorption strength, we find in the equilibrium case $\chi^\mathrm{ocrit}_\mathrm{eq} = 2.63 \pm 0.15$ for the self-avoiding chain and $\chi^\mathrm{ocrit}_\mathrm{eq} = 2.45 \pm 0.15$ for the phantom chain. This small difference vanishes for higher pulling speeds due to increasing chain stretching.

The general dependence of the critical adsorption strength on the potential range κ^{-1} and Kuhn length a for a polymer in equilibrium is $\chi^* \propto a^2\kappa^2$, as can be shown by scaling analysis [35, 42] or by explicit solution of the polymer path integral, cf. Section 2.1 and Eq. (2.12). As shown in the previous section, pulling on one end of a polymer reduces its effective Kuhn length perpendicular to the pulling direction.

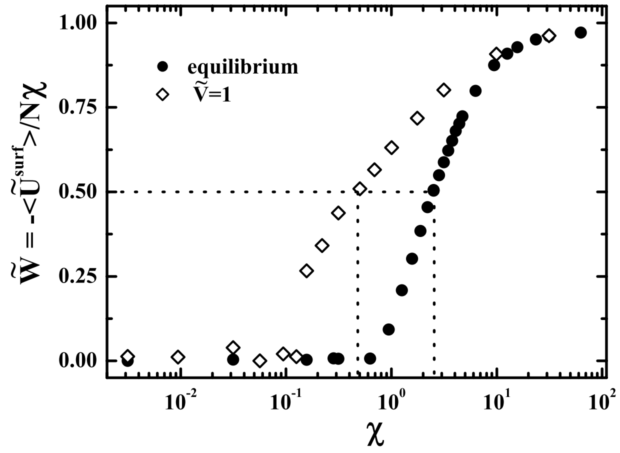

Figure 4.4: Mean normalized adsorption potential $\tilde{W} = -\langle \tilde{U}^{\rm surf} \rangle / N\chi$ for a 128mer as a function of the surface interaction parameter χ in equilibrium (filled circles) and being pulled with $\tilde{V} = Va/k_{\rm B}T\mu = 1$ (open diamonds). For pulling the curve is shifted to lower adsorption energies. The overcritical adsorption strengths are $\chi^{\rm ocrit} = 2.55$ and 0.48 for the equilibrium case and $\tilde{V} = 1$, respectively.

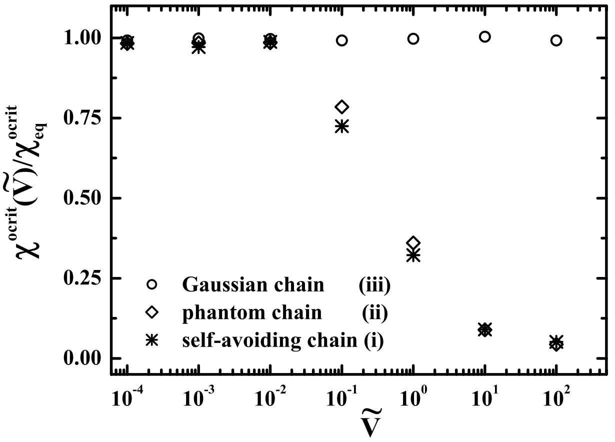

Figure 4.5: Overcritical adsorption parameter $\chi^{\rm ocrit}$ normalized by its equilibrium value as a function of the pulling velocity $\tilde{V} = Va/k_{\rm B}T\mu$ for different types of 64mer models: (i) self-avoiding polymer (crosses), (ii) phantom chain (no excluded volume, diamonds), and (iii) Gaussian chain (circles) which shows no effect due to decoupling of the pulling direction from other directions.

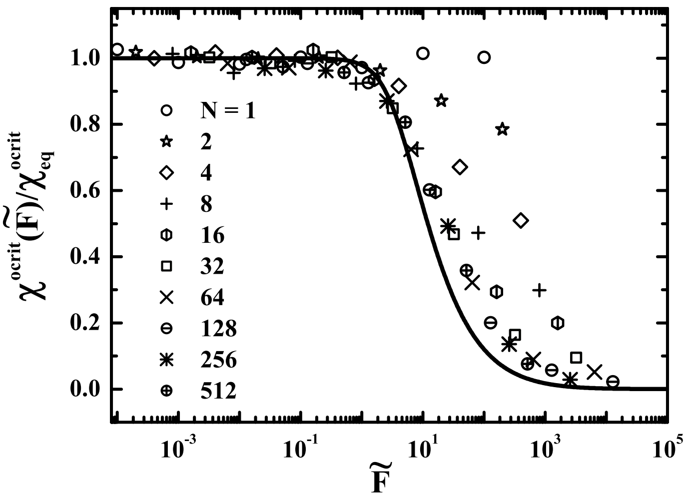

Figure 4.6: Overcritical adsorption parameter χ^{ocrit} normalized by its equilibrium value as a function of the pulling force $\tilde{F} = N\tilde{V} = NVa/k_{\text{B}}T\mu$ for a monomer up to a 512mer. Also shown is the scaling argument Eq. (4.16) for $N \to \infty$.

On the scaling level, the decrease of the critical adsorption potential depends on the pulling force solely via the renormalized Kuhn length according to

$$\chi^*(\tilde{F})/\chi^*_{\text{eq}} \approx \chi^{\text{ocrit}}(\tilde{F})/\chi^{\text{ocrit}}_{\text{eq}} \approx a^2_{\text{eff}}/a^2\,, \tag{4.16}$$

where a_{eff} is available through Eq. (4.15) using the mean pulling force on the first monomer, $\tilde{F} = N\tilde{V}$. In Fig. 4.6, where we plot the normalized overcritical adsorption energy $\chi^{\text{ocrit}}(\tilde{F})/\chi^{\text{ocrit}}_{\text{eq}}$ as a function of the mean pulling force $\tilde{F}$, the simulation data are compared with Eq. (4.16) for $N \to \infty$. Note that the dependence of the scaling prediction on N is rather small and therefore not shown in the figure. As expected, for a single monomer pulling has no effect on the adsorption transition. Polymers consisting of more than 64 monomers display limiting behavior that is very well predicted by our scaling theory. Deviations are expected due to the disregard of the surface and the idealization by an FJC model in deriving the polymer pulling response. More seriously, the flattening of the chain along its contour is inhomogeneous, and it is not clear how this affects the overall desorption threshold.

The adsorption-enhancement effect described here does *not* result from enhanced friction of the polymer close to the surface; in fact, a possible variation of the polymer mobility close to the surface (which occurs in reality) is not considered in our simplified model. However, in a constant velocity experiment a smaller mobility of the polymer close to the surface leads to an increase in the forces needed to pull with the same velocity and therefore shifts the critical adsorption strength to even smaller values.

Note that the enhancement effect is already quite pronounced at forces of $\tilde{F} \geq 10$. Although this means rather large velocities for small polymers, the desorption behavior of very large polymers can be strongly influenced at already small velocities. To put in numbers, assuming Stokes friction in water with viscosity η and using $\tilde{F} = 10$ we have $V = \tilde{F} k_\mathrm{B} T \mu / N a = \tilde{F} k_\mathrm{B} T / 3\pi\eta N a^2 \approx 0.4\,\mathrm{mm/s}$ for a synthetic polymer with $a = 1\,\mathrm{nm}$ and $N = 10^4$, or $V \approx 4\,\mu\mathrm{m/s}$ for phage DNA of length of the order of $10\,\mu\mathrm{m}$ ($a = 100\,\mathrm{nm}$, $N = 100$). Polymer velocities of µm/s are easily reached in the biological or technological context, the pulling-enhanced adsorption mechanism is therefore relevant to a host of different systems. Note that in certain flow situations very high velocities are present, *e.g.* in polymer applications for paper making or plug flows on end-tethered polymers. In a different context, the dependence of the adsorption shift on the applied velocity $\tilde{V} = \tilde{F}/N$ leads to preferential adsorption of polymers with a high polymerization index in a constant velocity experiment and thus could be used for length separation. In a related but conceptually simpler equilibrium situation, a surface-anchored polymer is pulled by an external force at its free end, in which case the force is homogeneous along the polymer contour. Following our earlier reasoning leading to Eq. (4.15) and using Eq. (4.13), the effective Kuhn length in this case is given by $a_\mathrm{eff}^2/a^2 = 3\tilde{\mathcal{L}}(\tilde{F})$. As before, the force flattens the chain, the effective Kuhn length and the critical adsorption strength decrease.

In summary, we have shown that laterally pulling a polymer by one end reduces its perpendicular roughness and the entropic cost of adsorption, and thus *enhances* polymer adsorption. On the scaling level, this behavior is explained by a renormalized Kuhn length in the direction normal to the surface. The influence of bending stiffness, electrostatic interactions between the polymer and the surface, surface patterns and more complicated flow geometries constitute possible extensions of the present study but will most likely not change the general mechanism for pulling-enhanced adsorption. The case of simple shear flow, the influence of hydrodynamic coupling of the monomers, and the effects of a corrugated surface will be discussed in the following three sections.

4.3 Polymers in simple shear flow

In the Case (II) a polymer is located close to an adsorbing surface and the solvent is perturbed by a simple shear flow normal to the surface as given by Eq. (4.3). The BD simulations are adapted using a modified version of Eq. (2.39), *i.e.*

$$\tilde{\boldsymbol{R}}_i(n+1) = \tilde{\boldsymbol{R}}_i(n) + \tilde{\mu}\left[(\tilde{\gamma} Z_i, 0, 0) - \boldsymbol{\nabla}_{\tilde{\boldsymbol{R}}_i} \tilde{U}(n) + \sqrt{2/\tilde{\mu}}\,\tilde{\boldsymbol{\xi}}_i(n)\right] , \qquad (4.17)$$

where the rescaled shear rate takes values in the range of $10^{-4} \leq \tilde{\gamma} = \dot{\gamma}_z a^2/\mu k_\mathrm{B} T \leq 100$. Other parameters are the same as described in Sections 2.3.1 and 4.2. In a similar fashion as for the pulled polymer we find enhanced adsorption by shear flow as checked for $N = 32$, 64, and 128. The results are qualitatively the same, so we limit the discussion to the 128mer. As exemplary case we show in Fig. 4.7 the mean normalized adsorption potential $\tilde{W} = -\langle \tilde{U}^\mathrm{surf} \rangle / N\chi$ for a 128mer as a function of the adsorption strength χ and compare the equilibrium case (filled circles) with shearing at $\tilde{\gamma} = 10$ (open squares). For low values of the adsorption strength χ we note a

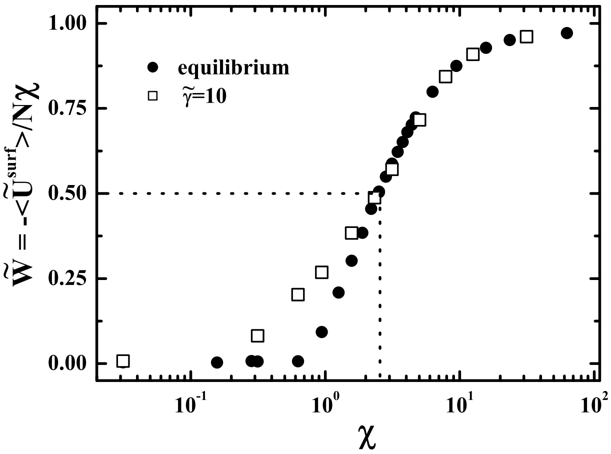

Figure 4.7: Mean normalized adsorption potential $\tilde{W} = -\langle\tilde{U}^{\rm surf}\rangle/N\chi$ for a 128mer as a function of the surface interaction parameter χ in equilibrium (filled circles) and being sheared with $\tilde{\gamma} = \dot{\gamma}_z a^2/k_{\rm B}T\mu = 10$ (open squares). When shearing, the curve in the low-χ regime is shifted to lower adsorption energies. For intermediate to high values of χ there is no considerable shift detectable. The lines denote the value of $\chi^{\rm ocrit}$ for the equilibrium case which coincides with its value for the sheared case within the simulation accuracy.

shift of the curve to smaller values of χ, *i.e.* enhanced adsorption. At values of χ above its 'overcritical' value defined by $\tilde{W}(\chi^{\rm ocrit}) = 1/2$, the curves start to overlap, and enhanced adsorption is no longer detectable. This is easily understood when taking the results for pulling an adsorbing polymer into account. For high adsorption strengths $\chi \gtrsim \chi^{\rm ocrit}$, the polymer adopts a flat configuration with long trains and only few, small loops, cf. Section 2.2 and Fig. 2.2. The stretching forces acting on the polymer are low and no flattening in the $\hat{z}$ direction occurs. Accordingly, the enhanced adsorption mechanism discussed previously does not come into play. On the other hand, close to the desorption transition, *i.e.* for small enough values of the surface interaction parameter $\chi < \chi^{\rm ocrit}$, the loop length diverges and the loops further away from the no-slip boundary surface experience stronger solvent flow, and the extensible flow component stretches the polymer; in this regime polymer adsorption is enhanced. The dependence of the shear influence on the adsorption strength is a fundamental difference to the case of pulling the polymer on one end as described in Section 4.2. There, the chain stretching and reduction in its roughness normal to the surface was rather independent of the adsorption strength. Hence, the effect of shearing cannot be identified only using the overcritical adsorption strength, as shown by the fact that these values hardly change with imposing shear flow. The mere analysis of the true critical adsorption strength, for which $\tilde{W}(\chi^*) \to 0$, is prohibited due to the uncertainty in pinpointing χ^* as discussed in Section 2.3.2. An attempt to take the variation of the shear effect with the adsorption strength into account is presented in the following.

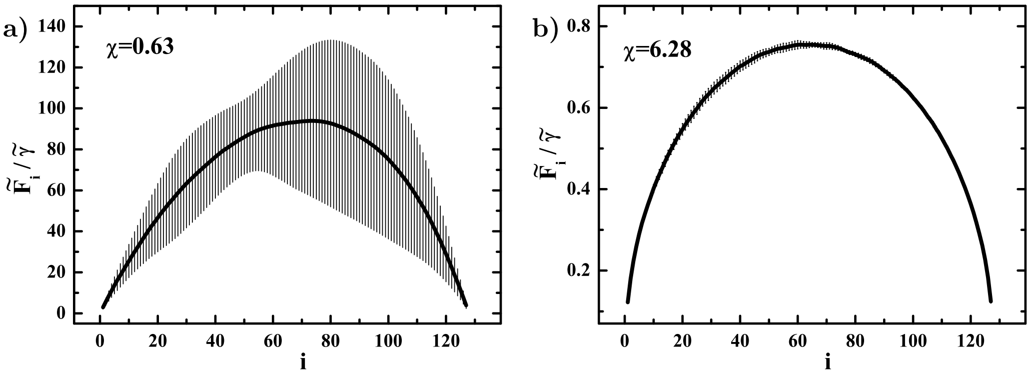

Figure 4.8: The mean rescaled and averaged lateral force $\tilde{F}_i/\tilde{\gamma} = F_i\mu/\dot{\gamma}_z a$ as a function of the bond index $i \in \{1 \ldots 127\}$ for a 128mer. The profiles are obtained from height distributions $\{\tilde{Z}_j\}$, $j \in \{1 \ldots 128\}$, recorded from *equilibrium* BD simulations at the adsorption strengths **a)** $\chi = 0.63$ and **b)** $\chi = 6.28$. Standard deviations serve as error estimates.

For weak shear rates, we estimate the influence by a first order perturbation of the equilibrium conformation of the polymer. The polymer height distributions at *equilibrium* but under specific values of the adsorption strength, $\{\tilde{Z}_j\}(\chi)$, $j \in \{1 \ldots N\}$, are taken from BD simulations. Using Eq. (4.8), the expected shear force on each bond in $\hat{x}$ direction is calculated. In Fig. 4.8 we show as exemplary cases the distribution of the mean rescaled stretching forces $\{\tilde{F}_i/\tilde{\gamma}\}(\chi)$, $i \in \{1 \ldots N-1\}$, for a 128mer for a) $\chi = 0.63$ and b) $\chi = 6.28$. The distributions are roughly bell shaped indicating that on average the largest forces act in the middle of the polymer. For $\chi = 0.63$, both the forces and their fluctuations are much larger than for $\chi = 6.28$ as rationalized before.

Using Eq. (4.15) the effective Kuhn length a_{eff} is calculated for a set of shear rates $10^{-4} \leq \tilde{\gamma} \leq 100$ using the distributions $\{\tilde{F}_i/\tilde{\gamma}\}(\chi)$ each obtained for the set of interaction parameters χ, which are available from the equilibrium simulation. Hence, we get a rough, first order perturbative estimate of the effective Kuhn length for chosen values of $\tilde{\gamma}$ and χ, $a_{\text{eff}}(\tilde{\gamma}, \chi)$. This quantity describes the flattening of a chain with a geometry or height distribution determined by χ in equilibrium, and sheared in bulk solution with a rate of $\dot{\gamma}_z$ hypothetically in the linear response regime.

We now assume that the renormalization which we used for the overcritical value of χ in the pulling case, Eq. (4.16), roughly holds for *any* point on the $\tilde{W}(\chi)$ curve. Hence, we obtain the new curve for the sheared case by shifting the equilibrium values $\tilde{W}_{\text{eq}}(\chi)$ by $a^2_{\text{eff}}(\tilde{\gamma}, \chi)/a^2$, and thus $\tilde{W}_{\tilde{\gamma}}(\chi') = \tilde{W}_{\text{eq}}(\chi)$, where $\chi' = \chi \times a^2_{\text{eff}}(\tilde{\gamma}, \chi)/a^2$. In Fig. 4.9 we show adsorption curves for a 128mer using shear rates of $\tilde{\gamma} = 0$ (equilibrium case, solid line), $\tilde{\gamma} = 0.1$ (grey diamonds), $\tilde{\gamma} = 1$ (black stars), and $\tilde{\gamma} = 10$ (open squares), where a) shows explicit BD simulation results and b) the predictions of the aforementioned procedure. Data for shear rates lower than 0.1 are not shown since they largely reproduce the equilibrium curve in both the simulations and the predicted values. The predictions qualitatively capture the mechanism of shear-induced adsorption enhancement. Due to the simplicity of the model the calculation overestimates the effect of shearing. In addition to the approximations already discussed in Section 4.2 for the pulling case this is mainly due to the following shortcomings: The disregard of the forces perpendicular to the $\hat{x}$ direction in deriving Eq. (4.8) and hence the disregard of tumbling motion leads to an overrating of the stretching motion. Secondly, the first order perturbative nature of the ansatz breaks down at too strong shear flows, *i.e.* the flattening of the chain height distribution by the shear forces further decreases the effect of the shear flow. This shortcoming is even more severe because increased adsorption also flattens the chains and hence reduces the flattening effect. Lastly, the assumption that the scaling relation Eq. (4.16) is valid not only for the critical and overcritical value, but for any value of χ, is a crude approximation. At the moment a more self-consistent model is under construction. Still, considering the clear results obtained from Section 4.2 we are confident to have identified a mechanism how shearing can lead to stronger adsorption in the weakly adsorbed regime.

In previous contributions discussing free draining BD simulations of polymers near adsorbing walls, Manias *et al.* [130] and Panwar *et al.* [133], have also found a flattening of the chain due to shear flow. Panwar *et al.* basically arrive at similar conclusions as presented here where they mostly argue on the basis of the distribution of trains, tails and loops, or the different spatial components of the radius of gyration. From our point of view, this procedure either involves a somewhat arbitrary height threshold for defining trains or contacts or is a rather indirect measure of the chain adsorption. Similarly, this applies to the work of Manias *et al.* who mostly use the number of contacts and the different spatial components of the diffusion coefficient to identify changes in the adsorption behavior. We feel that using the average adsorption energy U^{surf} as our main measure for the adsorption of the chain gives the most unequivocally defined quantity to analyze the influence on the adsorption behavior of the polymer chain.

Manias *et al.* also conclude that shear flow increases the diffusion coefficient normal to the surface which together with some peeling and tumbling mechanism leads to reduced adsorption due to shearing [130]. Following our previous reasoning with increased adsorption in the weakly adsorbing regime, this might take place for strongly adsorbed polymers or polymers in the intermediate adsorption range. In Fig. 4.10 we take a closer look at that regime, again for the 128mer. In a) we present an excerpt of Fig. 4.9a), where we plot the normalized adsorption potential $\widetilde{W}$ as a function of the adsorption strength χ. In b) we show the fraction of adsorbed monomers or trains, $\langle \Upsilon \rangle / N$, where a monomer counts as adsorbed when its height is less than the adsorption screening length, $\tilde{Z} < \tilde{\kappa}^{-1}$. Both data series do not suggest decreased adsorption in the medium to strong adsorption regime; however, for a definite statement more data with higher precision is needed. Using a similar analysis for loops and tails, we arrive at the same conclusion.

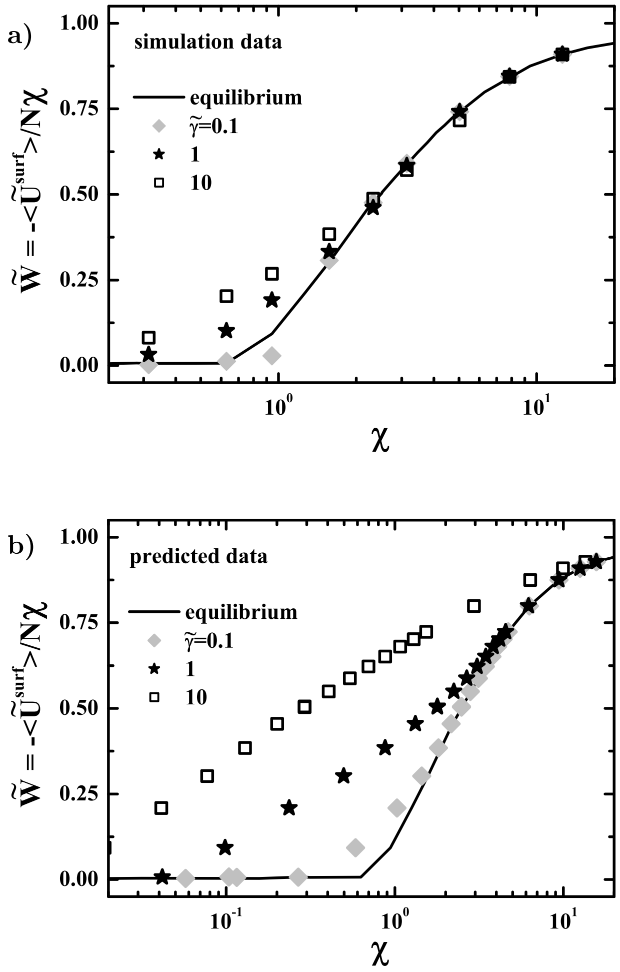

Figure 4.9: Mean normalized adsorption potential $\tilde{W} = -\langle \tilde{U}^{\mathrm{surf}} \rangle / N\chi$ for a 128mer as a function of the surface interaction parameter χ at shear rates of $\tilde{\gamma} = 0$ (equilibrium case, solid line), $\tilde{\gamma} = 0.1$ (grey diamonds), $\tilde{\gamma} = 1$ (black stars), and $\tilde{\gamma} = 10$ (open squares). **a)** Results from BD simulations, **b)** predictions from a first order perturbation ansatz in which the lateral force distribution due to the shear flow is calculated from the monomer height distribution in *equilibrium.* That force distribution is used in Eq. (4.15) to calculate the effective Kuhn length which in turn allows a mapping of the equilibrium curve to that of the sheared case, see text for details. The predictions capture the effect qualitatively, but overestimate it, cf. text for possible reasons.

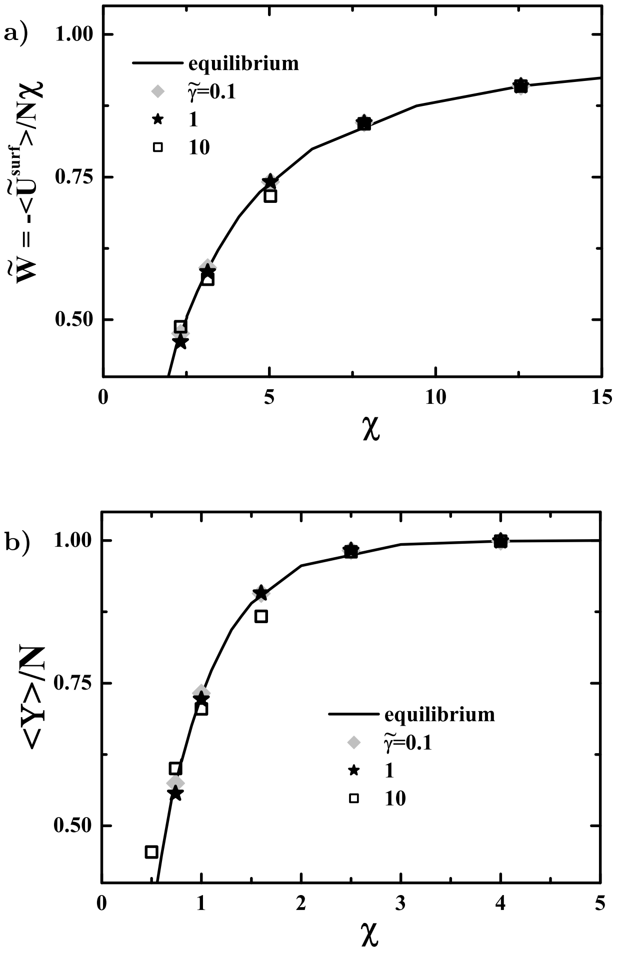

Figure 4.10: **a)** Mean normalized adsorption potential $\tilde{W} = -\langle \tilde{U}^{\mathrm{surf}} \rangle / N\chi$ and **b)** fraction of adsorbed monomers $\langle \Upsilon \rangle / N$ for a 128mer as functions of the surface interaction parameter χ at shear rates of $\tilde{\gamma} = \dot{\gamma}_z a^2/\mu k_{\mathrm{B}} T = 0$ (equilibrium case, solid line), $\tilde{\gamma} = 0.1$ (grey diamonds), $\tilde{\gamma} = 1$ (black stars), and $\tilde{\gamma} = 10$ (open squares). In both cases, the excerpt focuses on the strongly adsorbed regime, $\chi \geq \chi^{\mathrm{ocrit}}$. Note the different scales on the χ axes. Adsorbed monomers (trains) are defined by $\tilde{Z} < \tilde{\kappa}^{-1}$. No substantial changes in the quantities are found upon shearing.

Summarizing, shearing of dilute polymer solutions results in polymer configurations stretched and extended in the direction of the shear flow for the case of weakly adsorbed polymers. Similarly to the case of a laterally driven polymer, this leads to a decreased roughness in the direction normal to the surface, and hence *increased* polymer adsorption. In the strongly adsorbed regime, there is no pronounced effect due to flat polymer configurations hardly subject to the shear flow.

4.4 Hydrodynamic interactions in non-equilibrium adsorption

In Sections 2.3, 4.2, and 4.3, the hydrodynamic interaction of the monomers as well as the effect of a no-slip boundary of the wall have been neglected. For the equilibrium case this is fully justified, since the equilibrated system must not depend on the mobilities of the particles. In the case of non-equilibrium adsorption, it is often well justified to neglect hydrodynamic interactions since they drop rapidly enough close to a wall with no-slip boundary condition, cf. Section 1.2. From a technical point of view it is also a convenient way to separate different non-equilibrium effects from each other. In this section we follow a systematic approach and extend the non-equilibrium adsorption studies presented in the preceding sections by taking the hydrodynamic interaction into account.

The Langevin equation Eq. (2.37) is modified and now reads

$$\frac{\mathrm{d}\boldsymbol{R}_i}{\mathrm{d}t} = \sum_{j=1}^{N} \left[-\boldsymbol{\mu}_{ij} \boldsymbol{\nabla}_{\boldsymbol{R}_j} U(t) + \boldsymbol{\nabla}_{\boldsymbol{R}_j} \boldsymbol{\mu}_{ij} k_{\mathrm{B}} T \right] + \boldsymbol{\xi}_i'(t) \,, \tag{4.18}$$

where $\boldsymbol{\xi}_i'$ is a vectorial random velocity satisfying

$$\left\langle \boldsymbol{\xi}_i'(t) \otimes \boldsymbol{\xi}_j'(t') \right\rangle = 2 k_{\mathrm{B}} T \boldsymbol{\mu}_{ij} \delta(t - t') \,. \tag{4.19}$$

The coupling of the monomer motion is incorporated on the Stokes level, *i.e.* for zero Reynolds number, via the mobility tensor for the particles i and j, $\boldsymbol{\mu}_{ij}$. It also includes the effect of the no-slip boundary, planar wall using the stationary Green's function $\boldsymbol{G}^{\mathrm{B}}$ of the Stokes equation derived by Blake [33]. The multipole expansion of the mobility tensor reads within second order

$$\boldsymbol{\mu}_{ij}(\boldsymbol{R}_i, \boldsymbol{R}_j) = \left(1 + (a^2/24) \boldsymbol{\nabla}^2_{\boldsymbol{R}_i}\right) \left(1 + (a^2/24) \boldsymbol{\nabla}^2_{\boldsymbol{R}_j}\right) \boldsymbol{G}^{\mathrm{B}}(\boldsymbol{R}_i, \boldsymbol{R}_j) \text{ for } i \neq j. \tag{4.20}$$

The self-mobility μ_{ii} is obtained from Eq. (4.20) by taking the limit $\mathrm{R}_i \rightarrow \mathrm{R}_j$ and regularization with the intrinsic Stokes mobility of a sphere, $\mu = 3\pi\eta a$ [34]. Note that this procedure is computationally far more demanding than the method using free draining mobilities, and the maximum system size feasible on standard computers is limited to about $N \leq 100$ for simulations with high external fields. For the cases of pulling at one polymer end with velocity V, Case (I), the balancing force of varying direction and magnitude which is needed to move the first monomer with a rescaled velocity $\tilde{V}$ in $\hat{x}$ direction is calculated and added into Eq. (4.18). For exposing the polymer to shear flow of rate $\dot{\gamma}_z$, Case (II), Eq. (4.18) is extended by a shear term with a rescaled shear rate $\tilde{\gamma}$ as in Section 4.3.

The simulations are done for a 64mer with the same parameters as described in Sections 4.2 and 4.3. In Fig. 4.11 we plot the rescaled adsorption potential $\tilde{W} = -\langle \tilde{U}^{\mathrm{surf}} \rangle / N\chi$ as a function of the adsorption strength χ for the equilibrium case and various pulling velocities. In a) we show the results from simulations with free draining (FD) mobilities as in Section 4.2, b) are the data using hydrodynamic interaction (HI). As expected, the equilibrium results (solid lines) from both methods coincide within the precision of the simulations. For moderate pulling velocities, $\tilde{V} \leq 0.1$, the HI simulations quantitatively confirm the results obtained in the FD case. For elevated velocities, $\tilde{V} \geq 1$, the transition into the desorbed state changes from continuous (FD) to discontinuous (HI). In the HI case we find a critical adsorption energy larger than in the pulled, free draining case but still smaller than in the equilibrium case, $\chi^*_{\mathrm{eq}} > \chi^*_{\mathrm{HI}}(\tilde{V}) > \chi^*_{\mathrm{FD}}(\tilde{V})$, at which the internal energy drops discontinuously to zero. With further increasing pulling velocities, the hydrodynamic effect becomes more important; still the critical adsorption strength is smaller in the HI case than in equilibrium, *i.e.* in the HI case the adsorption is still enhanced with respect to the equilibrium situation, but this enhancement is smaller than in the FD case.

It has recently been shown by Sendner and Netz that a homogeneously and laterally driven rod close to a flat, non-adsorbing surface, *e.g.* a homogeneously charged rod electrophoretically driven parallel to a wall or a sedimenting rod close to a vertical wall, experiences a repulsive lift force away from the surface [137]. This lift force is due to the anisotropy of the hydrodynamic mobility parallel and normal to a rod [31] and due to an anisotropically distributed orientation of the rod in the vicinity of the no-slip boundary [137]. The authors showed that the corresponding potential decays as slowly as a Coulomb potential, $\propto 1/Z$. The combination of such a possibly weak, but long-ranged repulsive potential with the short-ranged attractive adsorption potential of the wall is known to change the adsorption transition type into discontinuous [138]. Although the situation can be expected to be different for long, flexible polymers that are solely driven at one end as studied here, the concept of the lift force still applies. Our simulations confirm the predicted change in the nature of the transition.

In another contribution, the same authors have showed a very similar mechanism to be active for polymers in shear flow [139]. Equivalently, an anisotropic angular distribution gives rise to a lift force decaying with the same power, *i.e.* like $1/Z^2$ in the force or like $1/Z$ in the potential. We test the influence of that lift force in HI simulations and show the results in Fig. 4.12, where the rescaled adsorption potential $\tilde{W}$ is shown as a function of the surface interaction parameter χ. a) shows FD results, b) are HI simulation data points. Again we observe the onset of a discontinuous adsorption transition with increasing shear rate. Due to the relative weakness of the adsorption enhancement by shearing in the FD case, the repulsive hydrodynamic effect dominates in the HI simulations. At rescaled shear

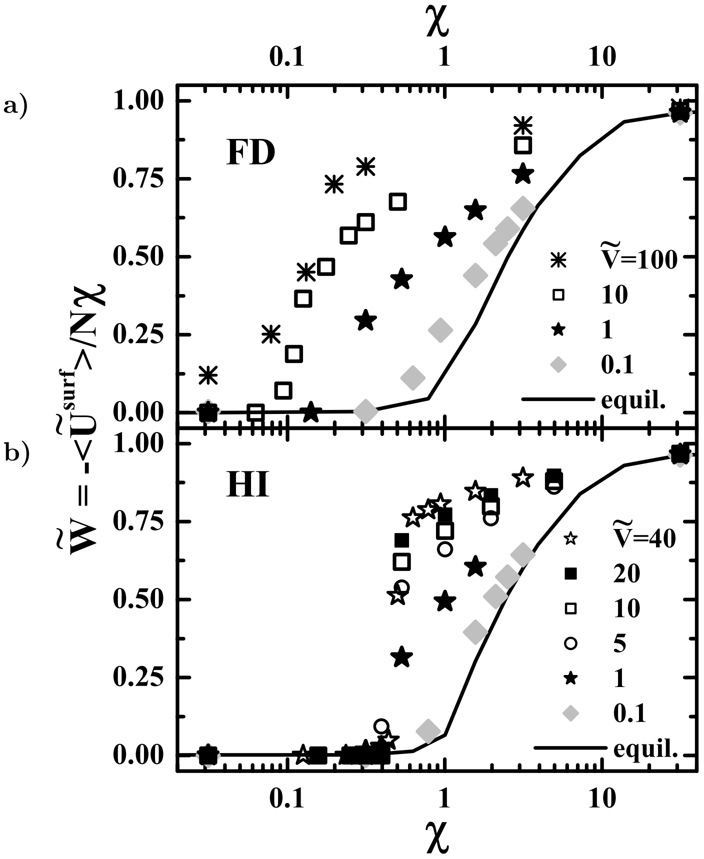

Figure 4.11: Mean normalized adsorption potential $\tilde{W} = -\langle \tilde{U}^{\mathrm{surf}} \rangle / N\chi$ for a 64mer as a function of the surface interaction parameter χ in equilibrium (solid lines) and being pulled with $\tilde{V} = Va/k_{\mathrm{B}}T\mu$. Results from BD simulations using **a)** free draining (FD) and **b)** hydrodynamic interaction (HI) of the monomer beads, where the rescaled velocities range from 0.1 (grey diamonds) to 40 (open stars, HI) or 100 (crosses, FD). HI simulations confirm the mechanism of enhanced adsorption by pulling, but also show a discontinuous desorption transition for higher pulling rates at some elevated critical adsorption energy of $\chi^*_{\mathrm{eq}} > \chi^*_{\mathrm{HI}}(\tilde{V}) > \chi^*_{\mathrm{FD}}(\tilde{V})$.

rates of $\tilde{\gamma} = 1$, where in the FD case slight adsorption enhancement is observed, the critical adsorption energy is already shifted to larger values in the HI case than for equilibrium adsorption, $\chi^*_{\mathrm{HI}}(\tilde{\gamma}) > \chi^*_{\mathrm{eq}} > \chi^*_{\mathrm{FD}}(\tilde{\gamma})$. Hence, in the HI simulations we observe net *reduced* adsorption under shearing.

Concluding this section, Brownian dynamics simulations including hydrodynamic interactions (HI) among the monomers taking the hydrodynamic no-slip boundary condition at the wall into consideration have confirmed the mechanism of enhanced adsorption by lateral pulling or simple shear flow as found by free draining (FD) simulations. For elevated pulling velocities and shear rates, a hydrodynamic lift force changes the adsorption transition from continuous to discontinuous type and shifts the critical adsorption strength to larger values. Hence, this effect counteracts the enhanced adsorption. In the case of shearing, the hydrodynamic effect dominates and leads to a net increase of the critical adsorption strength; for lateral pulling the resulting net adsorption is still enhanced.

4.5 Adsorption on corrugated surfaces

In the preceding sections the adsorbing wall has been supposed to be flat and homogeneous. This is a good approximation for atomistically flat surfaces with an attractive adsorption potential that is homogeneous on the length scale experienced by the polymer. Good examples for this are hydrophobic substrates where the hydrophobic interaction between a monomer and an individual surface site decays fast enough, such that only the surface and to some extent bulk integrated interaction, *i.e.* the Hamaker constants of the materials, are of importance. For charged substrates a homogeneous potential can only be assumed if the screening length is larger than the typical monomer bond length, and the bond length itself is larger than the typical distance of attractive sites on the substrate, $\kappa^{-1} > a > l$. For polyelectrolytes with large spatial distances between their charged groups, *e.g.* polymers with a low degree of sulfonation, this is accurate for highly charged surfaces such as mica at medium to high pH and at an ionic strength of less than $10^{-2}\,\mathrm{M}$. On the contrary, in many relevant cases polymers do experience corrugated potentials on charged surfaces.

In this section we investigate the effect of strongly localized attractive surface sites in the context of non-equilibrium adsorption, where we here focus on lateral pulling. To simplify the situation, we will only look at single particles, $N = 1$, and limit our considerations to a one-dimensional surface or a line. The corrugation is supposed to be periodic and to impose a similar lateral potential as used in the Frenkel-Kontorova model, Section 3.2. For better comparison, we choose the vertical part to be of the same analytical, short-ranged form as in the adsorption models before, Sections 2.3 and 4.2 to 4.4 and so introduce a model potential with different

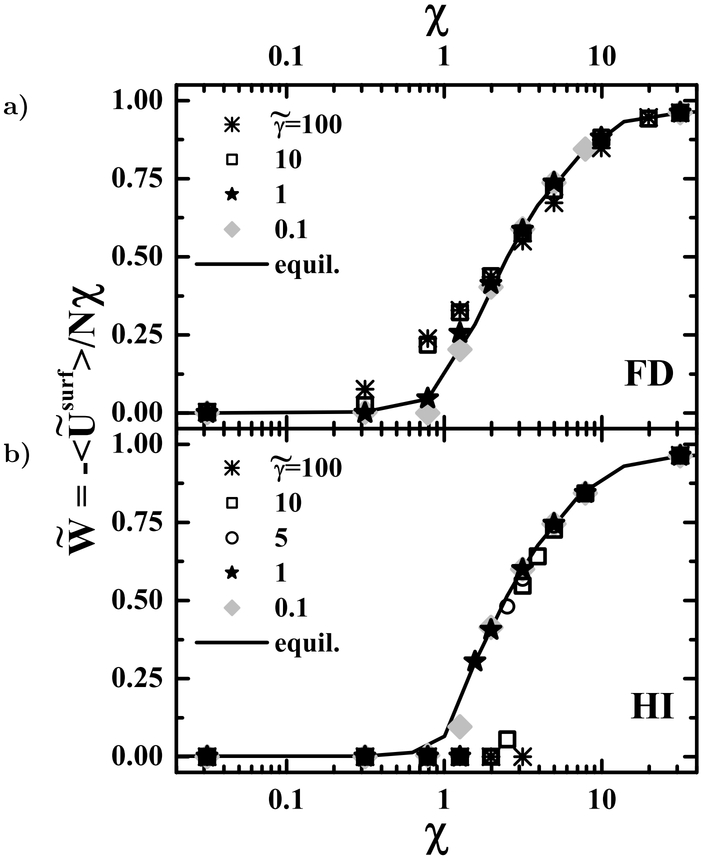

Figure 4.12: Mean normalized adsorption potential $\tilde{W} = -\langle \tilde{U}^{\mathrm{surf}} \rangle / N\chi$ for a 64mer as a function of the surface interaction parameter χ in equilibrium (solid lines) and being sheared with $\tilde{\gamma} = \dot{\gamma}_z a^2/\mu k_{\mathrm{B}} T$. Results from BD simulations using **a)** free draining (FD) and **b)** hydrodynamic interaction (HI) of the monomer beads, where the rescaled shear rates range from 0.1 (grey diamonds) to 100 (crosses). HI simulations show a discontinuous desorption transition for higher shear rates, $\tilde{\gamma} \geq 1$, at some elevated critical adsorption energy of $\chi^*_{\mathrm{HI}}(\tilde{\gamma}) > \chi^*_{\mathrm{eq}} > \chi^*_{\mathrm{FD}}(\tilde{\gamma})$.

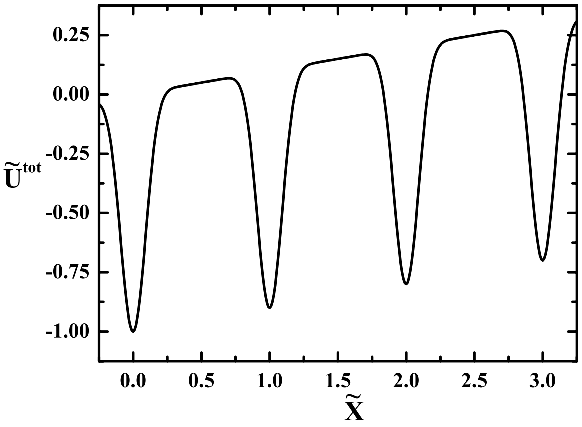

Figure 4.13: Total potential energy $\tilde{U}^{\mathrm{tot}}$ from Eq. (4.22) of a single particle at fixed height $\tilde{Z} = 0$ in a surface potential Eq. (4.21) and pulled with a rescaled force of $\tilde{F} = 0.1$. Surface interaction parameter is chosen as $\chi = 1$, corrugation power is $\beta = 6$. The particle is pulled to the left with $-\tilde{F}$ to provide better convergence in numerical integration routines.

interaction ranges in the lateral direction than in the vertical direction. In the two dimensions accessible to the particle $\hat{x}$ and $\hat{z}$, the rescaled surface potential reads

$$\tilde{U}^{\mathrm{surf}}(\tilde{X}, \tilde{Z}) = -\chi \exp\left(-\tilde{\kappa}\tilde{Z}\right) \left[\frac{\cos\left(2\pi\tilde{X}\right) + 1}{2}\right]^{\beta} , \tag{4.21}$$

where the length rescaling is done via the surface site distance l, thus $\tilde{X} = X/l$ and $\tilde{Z} = Z/l$. For the vertical decay length we take $\tilde{\kappa} = 1$; the corrugation power is chosen as $\beta = 6$, to produce strongly localized attractive sites, see also Fig. 4.13. The total potential energy is given by the sum of the surface energy and a pulling term,

$$\tilde{U}^{\mathrm{tot}}(\tilde{X}, \tilde{Z}, \tilde{F}) = \tilde{U}^{\mathrm{surf}}(\tilde{X}, \tilde{Z}) + \tilde{F}\tilde{X} , \tag{4.22}$$

where $\tilde{F} = Fl/k_{\mathrm{B}}T$ is the rescaled pulling force. Note that pulling with $-\tilde{F}$ is advantageous for the numerical integration in the analytical treatment. In Fig. 4.13 we plot $\tilde{U}^{\mathrm{tot}}$ for $\tilde{Z} = 0$ and $\chi = 1$. BD simulations following Eqs. (2.37) and (3.22) are done with a rescaled time step of $\tilde{\mu} = 10^{-6}$ over $n = 10^{10}$ time steps using different values of the adsorption strength, $0.1 \leq \chi \leq 1000$, and of the external pulling force $1 \leq \tilde{F} \leq 1000$.

To make the connection to Section 3.2, we first conduct simulations at fixed particle height $\tilde{Z} = 0$. In Fig. 4.14 we plot the normalized mobility $\langle\mu\rangle/\mu$ as a function of the external pulling force $\tilde{F} = Fl/k_{\mathrm{B}}T$. Data is presented for $\chi = 6.28$ (circles) and $\chi = 62.8$ (crosses). The general form of the curves is the same as of those shown in Section 3.2. For low enough external force, the particle sticks to the

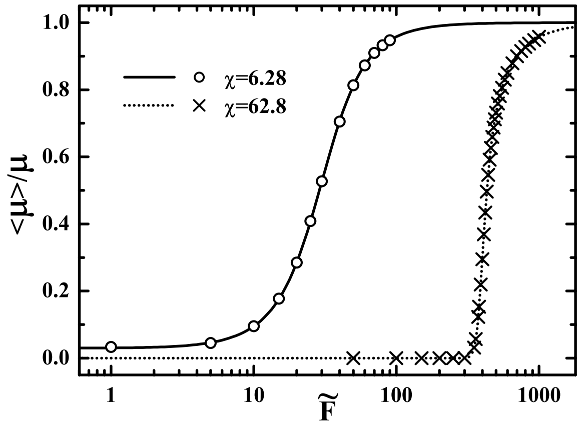

Figure 4.14: Average mobilities $\langle\mu\rangle/\mu$ for a single particle pulled through a strongly corrugated potential Eq. (4.21) as a function of the rescaled pulling force $\tilde{F} = Fl/k_{\rm B}T$. The particle height is fixed at $\tilde{Z} = 0$, the corrugation power is chosen as $\beta = 6$, the surface interaction strength is $\chi = 6.28$ (circles and solid line) and $\chi = 62.8$ (crosses and dotted line). Data points are taken from simulations, the lines from theory, Eq. (4.26).

attractive surface sites apart from short escapes caused by thermal collisions. The average mobility is exponentially damped and practically static fraction is observed. At much larger forces the average mobility approaches its bulk value and the motion is uniform regardless of the potential corrugation. Similarly, the average surface potential experienced by the particle has the reverse form, as seen in Fig. 4.15. For low pulling forces, $\tilde{F} \to 0$, the normalized adsorption potential $-\langle\tilde{U}^{\rm surf}\rangle/\chi$, approaches the Boltzmann weighted average over the adsorption energy Eq. (4.21). For $\chi = 6.28$ this equilibrium average is $-\langle\tilde{U}^{\rm surf}\rangle_{\tilde{F}\to 0}/\chi = 0.90$, for $\chi = 62.8$ we have $-\langle\tilde{U}^{\rm surf}\rangle_{\tilde{F}\to 0}/\chi = 0.98$; only in the limit of $\chi \to \infty$ a normalized equilibrium potential of unity is reached, $-\langle\tilde{U}^{\rm surf}\rangle_{\tilde{F}\to 0}/\chi = 1$. On the other hand, for large enough pulling forces, $\tilde{F} \to \infty$, the particle probes each point along the $\hat{x}$ coordinate with equal probability. The average normalized surface potential in all cases reaches the arithmetic average over Eq. (4.21), $-\langle\tilde{U}^{\rm surf}\rangle_{\tilde{F}\to\infty}/\chi = 0.23$ indicated in Fig. 4.15 by the horizontal, dashed line.

The simulation data in Figs. 4.14 and 4.15 coincide perfectly with predictions shown for $\chi = 6.28$ as solid lines and for $\chi = 62.8$ as dotted lines. These predictions are obtained by numerical integration of the distribution function at constant $\tilde{Z}$ which can be formulated exactly for this simple system. The distribution function for finding the particle at rescaled time $\tilde{t} = t\mu k_{\rm B}T/l^2$ and position $\tilde{X}$, $P(\tilde{X},\tilde{t})$, is available from the Fokker-Planck equation which in the *stationary* case reads [32, 140]

$$0 = \frac{\partial P(\tilde{X},\tilde{t})}{\partial \tilde{t}} = \frac{\partial\left(\frac{\partial \tilde{U}^{\rm tot}}{\partial \tilde{X}} P(\tilde{X},\tilde{t})\right)}{\partial \tilde{X}} + \frac{\partial^2 P(\tilde{X},\tilde{t})}{\partial \tilde{X}^2}\,. \tag{4.23}$$

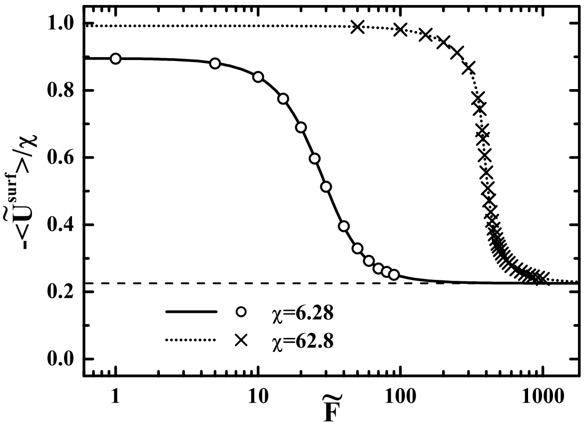

Figure 4.15: Average surface potential $-\langle\tilde{U}^{\rm surf}\rangle/\chi$ for a single particle pulled through a strongly corrugated potential Eq. (4.21) as a function of the rescaled pulling force $\tilde{F} = Fl/k_{\rm B}T$. The particle height is fixed at $\tilde{Z} = 0$, the corrugation power is $\beta = 6$, the interaction strength is chosen as $\chi = 6.28$ (circles and solid line) and $\chi = 62.8$ (crosses and dotted line). Data points are taken from simulations, the lines from theory, Eq. (4.27). The dashed, horizontal line denotes the large force limit and arithmetic average over the surface potential $-\langle\tilde{U}^{\rm surf}\rangle_{\tilde{F}\to\infty}/\chi = 0.23$. The low force limits are given by the Boltzmann averages over the potential, $-\langle\tilde{U}^{\rm surf}\rangle_{\tilde{F}\to 0}/\chi = 0.90$ ($\chi = 6.28$) and $-\langle\tilde{U}^{\rm surf}\rangle_{\tilde{F}\to 0}/\chi = 0.98$ ($\chi = 62.8$).

For potentials consisting of a linear and a periodic part, $\tilde{U}^{\rm surf}(\tilde{X}) = \tilde{U}^{\rm surf}(\tilde{X}+1)$, both of which are independent of time, the formal stationary solution is given by

$$P(\tilde{X}) = \frac{\exp\left(-\tilde{U}^{\rm tot}(\tilde{X})\right)}{Q} \times \left[\frac{\int_0^1 {\rm d}\tilde{X}' \exp\left(\tilde{U}^{\rm tot}(\tilde{X}')\right)}{1-\exp\left(\tilde{U}^{\rm tot}(1)-\tilde{U}^{\rm tot}(0)\right)} - \int_0^{\tilde{X}} {\rm d}\tilde{X}' \exp\left(\tilde{U}^{\rm tot}(\tilde{X}')\right)\right], \quad (4.24)$$

where Q is a constant for normalizing $\int_0^1 {\rm d}\tilde{X}\, P(\tilde{X})$ to unity. We also keep in mind that both the total potential energy and the probability distribution function depend on the fixed parameters $\tilde{Z}$, $\tilde{F}$, and χ, but simplify the notation to $\tilde{U}^{\rm tot}(\tilde{X})$ and $P(\tilde{X})$. For $\tilde{F} \to 0$, the distribution function Eq. (4.24) simplifies into the Boltzmann distribution,

$$P^{\rm B}(\tilde{X}) = \exp\left(-\tilde{U}^{\rm surf}(\tilde{X})\right)/Q', \quad (4.25)$$

where Q' is needed for proper normalization. The rescaled mobility is available as

$$\langle\mu\rangle/\mu = \frac{1}{-F\mu}\left\langle\frac{{\rm d}X}{{\rm d}t}\right\rangle = \frac{1}{\tilde{F}Q}\int_0^1 {\rm d}\tilde{X}\,\frac{\partial\tilde{U}^{\rm tot}(\tilde{X};\tilde{Z},\tilde{F})}{\partial\tilde{X}} P(\tilde{X};\tilde{Z},\tilde{F})\,. \quad (4.26)$$

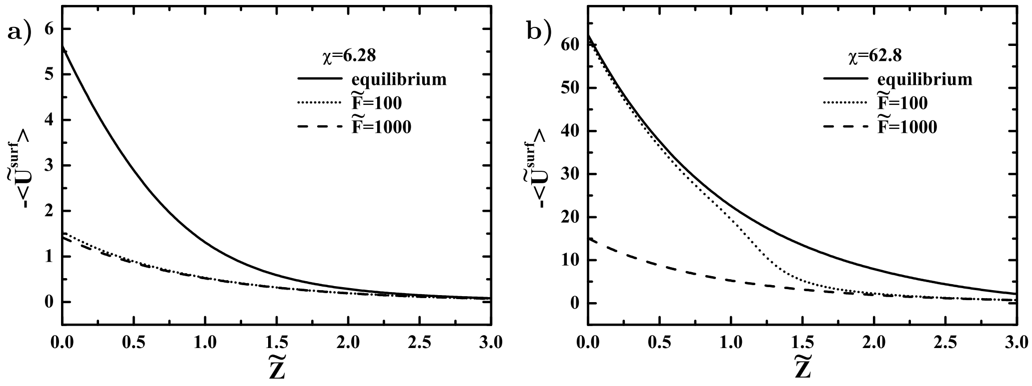

Figure 4.16: Average surface potential $-\langle\tilde{U}^{\mathrm{surf}}\rangle$ for a single particle as a function of its rescaled height $\tilde{Z}$. The curves are obtained from Eq. (4.27) using the fixed surface potential parameters $\tilde{\kappa} = 1$, $\beta = 6$, and **a)** $\chi = 6.28$ and **b)** $\chi = 62.8$. Both cases show equilibrium data ($\tilde{F} = 0$, solid lines) and data for the particle being laterally pulled with $\tilde{F} = 100$ (transient regime, dotted lines) and $\tilde{F} = 1000$ (high-force regime, dashed lines).

The average surface potential at fixed force, height, and adsorption strength is similarly obtained as

$$-\left\langle \tilde{U}^{\mathrm{surf}} \right\rangle / \chi = -\frac{1}{\chi Q} \int_0^1 \mathrm{d}\tilde{X}\, \tilde{U}^{\mathrm{surf}}(\tilde{X};\tilde{Z}) P(\tilde{X};\tilde{Z},\tilde{F}) \,. \tag{4.27}$$

Using Eq. (4.27), it is now easy to construct an effective potential energy profile for the pulled particle. For that, we keep the surface attraction χ and the pulling force $\tilde{F}$ constant and calculate $-\langle\tilde{U}^{\mathrm{surf}}\rangle$ as a function of the particle height $\tilde{Z}$. In Fig. 4.16 we show these profiles for the equilibrium case (solid lines), and for pulling forces of $\tilde{F} = 100$ (dotted lines) and $\tilde{F} = 1000$ (dashed lines). The plots are for a) $\chi = 6.28$ and b) $\chi = 62.8$. For $\tilde{F} = 1000$ the corrugation in both cases, *i.e.* for low and high surface attraction, is weak enough and the large-force limit $-\langle\tilde{U}^{\mathrm{surf}}\rangle = 0.23\,\chi \exp\left(-\tilde{\kappa}\tilde{Z}\right)$ is obtained at all height values $\tilde{Z}$. With $\tilde{F} = 100$ an intermediate case applies: For $\chi = 6.28$ the average adsorption potential drops to values close to those of the high-force limit. However, at $\chi = 62.8$ the particle sticks to the adsorption sites as in the equilibrium case for small distances from the surface. With increasing height the drop in the maximum interaction potential leads to weaker corrugation and hence, at a height between $0.5 < \tilde{Z} < 2$ a transition occurs for $\tilde{F} = 100$ from the low-force into the high-force limit.

The decrease in the average experienced adsorption potential with increasing pulling force points to the possibility of shifting the adsorption transition on a corrugated substrate to higher adsorption strengths by lateral pulling. This hypothesis is tested in simulations by relaxing the height constraint on the particle. As described in Sections 2.3 and 4.2 to 4.4, the average adsorption energy is measured as

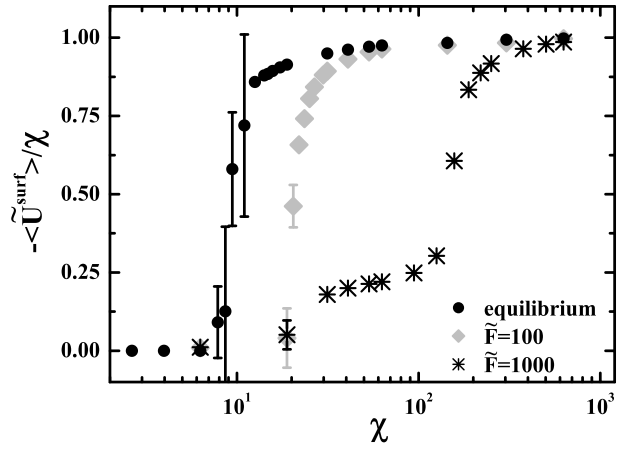

Figure 4.17: Mean normalized adsorption potential $-\langle\tilde{U}^{\mathrm{surf}}\rangle/N\chi$ for a single particle as a function of the surface interaction parameter χ. The particle is subject to the laterally corrugated surface potential Eq. (4.21) ($\beta = 6$, $\tilde{\kappa} = 1$); data is for the equilibrium case (black circles), and for lateral pulling with a rescaled force of $\tilde{F} = 100$ (grey diamonds) and $\tilde{F} = 1000$ (crosses). Upon pulling, the average experienced adsorption potential is reduced with respect to the equilibrium case, hence the (over)critical adsorption strength is shifted towards larger values of χ, and reduced adsorption is observed.

a function of the adsorption strength and shown in Fig. 4.17, both in equilibrium (black circles) and at fixed lateral pulling forces of $\tilde{F} = 100$ (grey diamonds) and $\tilde{F} = 1000$ (crosses). Indeed, we observe a decrease of the average normalized adsorption energies $-\langle\tilde{U}^{\mathrm{surf}}\rangle/\chi$ with increasing pulling force. Accordingly, pulling leads to an increase of the critical and overcritical adsorption strengths and hence to *reduced* adsorption.

In principle, it is possible to use the height profiles of the effective substrate potential energy from Fig. 4.16 to calculate adsorption isotherms for fixed adsorption strength χ and pulling force $\tilde{F}$. For that, appropriately normalized Boltzmann averages of these energies over the height have to be performed. In the case of a single particle in semi-infinite space, as applies to the BD simulations shown in Fig. 4.17, there is no adsorption transition and the equilibrium particle position is always at infinite distance from the surface, cf. Section 2.3. However, for finite particle concentration, the potential energy profiles can be converted into density profiles [24]. In a similar fashion, for finite simulation box sizes in the $\hat{z}$ direction the average adsorption energies obtained from simulations are expected to reproduce the effective surface potentials Boltzmann-averaged over the finite $\hat{z}$ range. We leave this procedure to works going beyond the single polymer and single particle regime.

Relating the observed decrease in adsorption to other non-equilibrium effects discussed in this chapter, reduced adsorption can only be effective when the corrugation of the substrate is large enough such that the particle experiences different average adsorption potentials in the equilibrium and in the pulled case. For this study, we used a hypothetical model potential with different decay length scales in the vertical and in the lateral direction. Apart from this being a simple way to produce a laterally strongly corrugated potential landscape, this toy model might be of physical relevance in situations where the interaction does not only depend on the mere distance between the solute and the surface site, but also on their mutual orientation, as in hydrogen bonds. Limited orientational freedom of surface hydroxyl groups might result in different potential range length scales for the distinct directions with respect to the surface normal.

In a similar fashion we can assume that a polymer dragged over a corrugated surface is subject to reduced adsorption. As discussed in Section 3.2, such a mechanism would crucially depend on the commensurability of the two lattices defined by the polymer bond length and the surface site distance. For disordered surfaces we expect this effect to be of minor importance or even to vanish. More importantly, pulling on one end of a polymer also flattens it and enhances adsorption as discussed in Section 4.2. As our analysis has shown there, this effect grows with increasing pulling force regardless of the length of the polymer once very short oligomers are neglected, cf. Fig. 4.6. This is in contrast to the desorption effect observed here, where the total force needed to pull a polymer over a corrugated surface with the same velocity and uniform motion increases about linearly in N, as suggested in Section 3.2. Hence, for fixed external force, we expect the enhancement in adsorption caused by the flattening of the chain to dominate over the adsorption reduction through surface corrugation with increasing length of the chain. Preliminary BD simulations in model potentials such as the one used here have confirmed this hypothesis already with only short oligomers ($N = 10$). Likewise, at highly corrugated surfaces with a strong potential in the non-equilibrium desorption effect, very high forces are needed for pulling the polymer or adsorbent smoothly, see Eq. (3.32), again suggesting a strong flattening of the chain and hence adsorption increase. Nonetheless, we suspect the laterally corrugated potential energy landscape to be the cause of the partial desorption observed in the MD simulations for the polypeptide on the hydrophilic diamond surface, see Section 3.3 and Fig. 3.19. However, a fundamental difference between the BD and MD simulation models is the competitive binding of explicit water molecules to the surface hydroxyl groups which adds another timescale for the MD simulations. On the contrary, the surface potential in the BD simulations is constant over time. Again, for long enough polypeptides we expect non-equilibrium desorption due to surface corrugation to be negligible even though the situation is more complicated.

Summarizing, we have used BD simulations to investigate the changes in the adsorption of a single particle when the particle is laterally pulled over a corrugated surface. We have identified a mechanism how the pulling leads to a reduced average adsorption potential experienced by the solute. Thus, pulling leads to *reduced* adsorption. This effect is suggested to be irrelevant for long polymers. The average mobility and surface potential energy at fixed height and pulling force is well described by a Fokker-Planck formalism which has been solved by numerical integration.

Chapter 5

Elasticity of single polymers

Understanding polymer conformations both with and without external fields is a key element to the field of polymer science. In fact, the combination of the monomer connectivity and hence the restriction of their spatial positions on the one hand and the vast number of possible spatial configurations of these polymer molecules on the other hand bring about interesting phenomena such as phase transitions and self-similarity. For this reason the elasticity of polymers and thus their configurational entropy have been long-studied subjects. Interconnected chains as simplified models for polymer molecules mark the introduction of polymers into the field of statistical physics and date back into about the middle of the twentieth century [22, 23, 141, 142]. Put in another way, these models have established the foundation of theoretical polymers physics.

In the context of this thesis, it is in most cases of polymers far from equilibrium *not* sufficient to apply ideal, Gaussian polymer models as we have also shown in Chapter 4. Appropriate models must go beyond the level of linear response theory. Since we are mostly interested in non-equilibrium but stationary states, equilibrium elasticity theory is an appropriate tool and a reasonable starting point. For the explicit time evolution of polymer conformations see *e.g.* Refs. [143, 144] and references therein.

From a practical point of view, single polymer elasticity is an important feature for many aspects of polymer applications such as the (visco-)elastic response of dense and dilute polymer networks, *e.g.* rubber [145], the dynamics of polymer brushes [10], or biomolecular interactions and recognition [12]. Protein ubiquitination and protein translocation by the signal recognition particle into the endoplasmatic reticulum are two such biological processes where polypeptides are believed to be stretched into extended configurations.

On the single molecule level, the use of AFM force spectroscopy and optical or magnetic tweezers [61, 134] has enabled to probe the elasticity of single polymers to an extremely high resolution. This includes unfolding of biomolecules with specific folding patterns and conformational transitions such as the protein titin, polysaccharides or DNA [146]. Synthetic macromolecules with elasticities that are mostly captured by the conformational diversity of chain molecules rather than involving specific folding interactions have also been studied [61, 91, 147, 148]. Considering the great advance in single molecule technology and accordingly the measurement precision, we develop improved descriptions of equilibrium single polymer elasticity on the microscopic scale. In the first part, Section 5.1, the classical discrete models are briefly reviewed and a freely rotating chain (FRC) model with extensible monomers and finite bending rigidity is introduced. Section 5.2 discusses the transfer matrix implementation for microscopic alternating copolymers and its application to polypeptides. In Section 5.3 the rotational rigidity of polypeptides is investigated and a modified FRC model is proposed to deal with such situations.

5.1 A discrete extensible semi-flexible chain model

The classical model for polymer elasticity is named after its authors Kratky and Porod [141, 142]. Its continuum version, the so-called worm-like chain (WLC) model is used throughout the biological physics community to describe the elasticity of semi-flexible biopolymers [23]. Because of the popularity of one interpolation formula that has been introduced by Marko and Siggia [149] it is often also used for modeling the elasticity of synthetic, rather flexible polymers although its connection with a microscopic model has only recently been shown [93]. In this treatise we will not consider the WLC due to its lack of a microscopic foundation and its particularly bad performance for most polymers with a simple, single-stranded backbone at intermediate to large stretching forces. The interested reader is referred to Refs. [18, 23, 150] and references therein.

All polymer models that we will discuss in the following take into account bonded nearest neighbor interactions only. They neglect next-nearest neighbor interactions via the backbone and *e.g.* repulsive Coulomb or attractive van-der-Waals interactions between any two monomers. These idealizations are appropriate for uncharged polymers in good solvent, for other treatments see *e.g.* Refs. [151–153]. Excluded volume effects are also neglected which is justifiable for forces perturbing the polymer $F \geq k_\mathrm{B}T/a \approx 4\,\mathrm{pN}$, following a similar reasoning as in Section 3.3.3 and assuming a typical bond length of $1\,\mathrm{nm}$. The force range experimentally studied is usually well above this threshold, hence neglecting finite monomer volumes is a valid approximation. The same is true for the disregard of the surfaces which the polymers are attached to. It is possible to include non-penetrable surfaces into the numerical treatment we introduce here, but at already small stretching forces no deviations from the case of an isolated chain can be found. This is so, because the return probability of a chain becomes vanishingly small if an external force is applied. In the literature this point is commonly neglected by using the free chain models without further notice.

The simplest of any discrete microscopic polymer models is the freely jointed chain (FJC) [22, 23]. In a FJC with N monomers, $N-1$ bonds of constant length a are used to model the polymer, cf. Fig. 5.1a). Both the bond angle γ and the rotational angle ψ are free, Fig. 5.1c). A next step is to take into account the typical bond angles of the polymer, but still assuming free rotation around the preceding bond, Fig. 5.1d). Hence, γ and a are fixed, but ψ is free. This model is called freely rotating chain (FRC) and has been analyzed in detail only recently [93]. It is quite useful for modeling *e.g.* linear alkane chains in which typically a tetrahedral angle is appropriate for the bond angle, $\gamma \approx 70.5^\circ = \pi - 109.5^\circ$. Allowing the bond length a in a FRC to vary introduces extensibility, Fig. 5.1e). The bond is possibly also compressed, but this does not contribute significant conformations when a stretching force is applied. Fig. 5.1f) shows a FRC model into which flexibility of the bond angle γ has been introduced. Deformations of microscopic polymer bonds are important in the strong stretching regime, $D \to L$, as has been shown in several contribution, see *e.g.* Ref. [91]. Here, $D = Z_N - Z_1$ is the distance between the first and the last monomer in the direction of the force $\hat{z}$, and $L = (N-1)a_0 \cos(\gamma_0/2)$ is the FRC contour length. With very few exception [154] most studies have incorporated enthalpic extensibility by separating the entropic from the enthalpic contributions [18, 91, 150]. Here we go beyond this approximation and introduce a FRC model which is extensible and semi-flexible: the discrete extensible semi-flexible chain (DESC) model. The equilibrium thermodynamics of the model are exactly solved using a numerical transfer matrix approach [22, 93, 155].

5.1.1 The transfer matrix treatment of DESC

For a FRC or DESC polymer under an external force F in $\hat{z}$ direction it is sufficient to know the position of each monomer projected to the $\hat{z}$ axis, Z_i $(i \in \{1 \ldots N\})$, and the angle which the bond leading to monomer i takes with that axis, θ_i, cf. also Fig. 5.1b). Note that we renumber bonds as compared to Chapter 4 and now have a virtual bond $\boldsymbol{r}_1$ leading to the first monomer whose meaning will become clear later. For shorthand notation we introduce $\boldsymbol{\Gamma}_i = \{Z_i, \theta_i\}$. The polymer configuration with i monomers is formulated in terms of its end-to-end probability distribution or Green's function, $P_i(\boldsymbol{\Gamma}_i; \boldsymbol{\Gamma}'_1)$, which gives the probability of monomer i being in state $\boldsymbol{\Gamma}_i$ given that the first monomer 1 is in state $\boldsymbol{\Gamma}'_1$. Considering only nearest-neighbor bonds along the polymer molecule, we can use a propagation operator $\boldsymbol{\mathcal{T}}(\boldsymbol{\Gamma}_i, \boldsymbol{\Gamma}_{i-1})$ called the transfer operator or transfer matrix, such that the Green's function for the ith monomer can be constructed from the Green's function of the preceding $(i-1)$th monomer as

$$P_i(\boldsymbol{\Gamma}_i; \boldsymbol{\Gamma}'_1) = \int \mathrm{d}\,\boldsymbol{\Gamma}_{i-1} \boldsymbol{\mathcal{T}}(\boldsymbol{\Gamma}_i, \boldsymbol{\Gamma}_{i-1}) P_{i-1}(\boldsymbol{\Gamma}_{i-1}; \boldsymbol{\Gamma}'_1)\,. \tag{5.1}$$

In thermal equilibrium, the transfer operator reads

$$\boldsymbol{\mathcal{T}}(\boldsymbol{\Gamma}_i, \boldsymbol{\Gamma}_{i-1}) = \int_0^\infty \mathrm{d}a_i \int_0^\pi \mathrm{d}\gamma_i\, \boldsymbol{\mathcal{C}}(\boldsymbol{\Gamma}_i, \boldsymbol{\Gamma}_{i-1}; a_i, \gamma_i) \exp\left(-\frac{E(a_i, \gamma_i)}{k_\mathrm{B} T}\right), \tag{5.2}$$

where $\boldsymbol{\mathcal{C}}(\boldsymbol{\Gamma}_i, \boldsymbol{\Gamma}_{i-1}; a_i, \gamma_i)$ is the connectivity operator containing the geometry of the polymer model and is of purely entropic origin. a_i and γ_i are the length and the

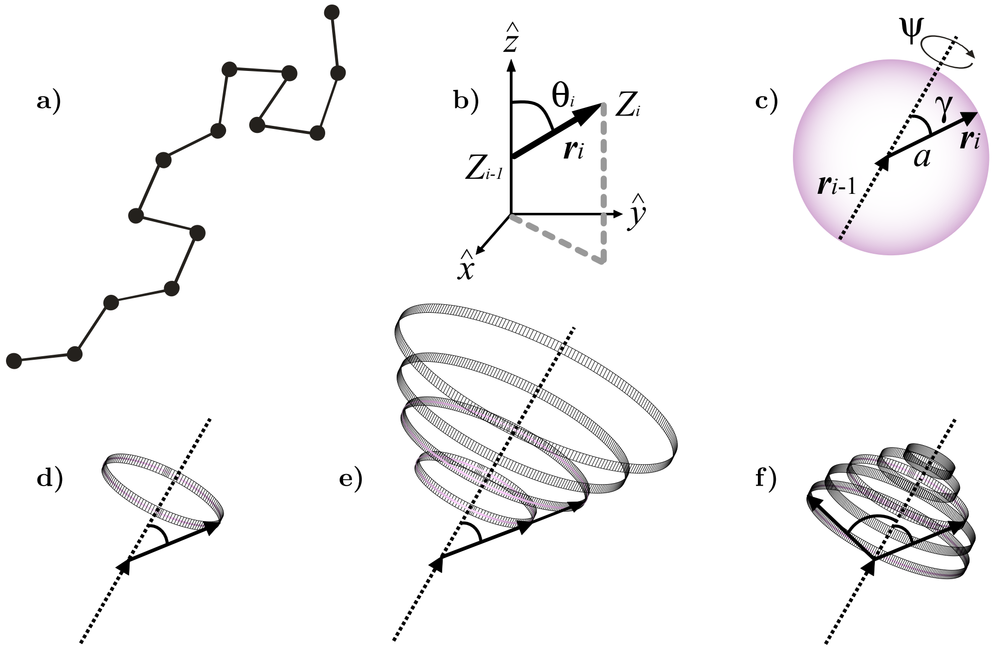

Figure 5.1: Sketches of microscopically based polymer models. **a)** Freely jointed chain (FJC), interconnected monomers are presented as small spheres. **b)** Coordinate system useful for discrete polymer models; the $\hat{z}$ axis coincides with the direction of an externally applied force, $z = 0 = Z_1$ is the position of the first monomer; the current bond $\boldsymbol{r}_i$ (solid arrow) is characterized by its azimuthal angle with the $\hat{z}$ axis, θ_i, and the height positions of monomer $i-1$, Z_{i-1}, and of monomer i, Z_i. Note that a renumbering of bonds has occurred as compared with Chapter 4, we now have N monomers and N bonds, where bond 1 is a virtual bond (see text). For shorthand notation, $\boldsymbol{\Gamma}_i = \{Z_i, \theta_i\}$ is introduced. **c)-f)** Graphical representation of different polymer models with only nearest neighbor interactions along discrete bonds. The preceding bond $\boldsymbol{r}_{i-1}$ is shown by a dashed arrow, one possible next bond $\boldsymbol{r}_i$ is presented by the solid arrow. The azimuthal angle of bond i with respect to bond $i-1$ is denoted as γ, the zenithal or rotational angle is ψ, and the bond length is a. **c)** FJC model: a is fixed to a_0, both γ and ψ are free; monomer $i+1$ is situated anywhere on a sphere of radius a_0 around the position of monomer i with equal probability. **d)** Freely rotating chain (FRC) model: a and bond angle γ are fixed, ψ is free; monomer $i+1$ lives on a circle of radius $a_0 \cos\gamma_0$. **e)** extensible FRC: like FRC, but a varies; monomer $i+1$ is found on a cone with opening angle 2θ. **f)** semi-flexible FRC: like FRC, but γ varies; monomer $i+1$ sits on surface sectors of a sphere, for full variability of γ the FJC is recovered. The chain model developed in Section 5.1 is a combination of **e)** and **f)**: a discrete extensible semi-flexible chain (DESC). Its extended ($a = a_0 + \Delta a$) and bent ($\gamma = \gamma_0 - \Delta\gamma$) configurations of nearest neighbor bonds are not of the same probability as the equilibrium configuration, but are Boltzmann weighted using the microscopic energy obtained from *ab initio* calculations or *ad-hoc* energy functions.

angle of bond i, respectively. The exponential term introduces a thermal weight via the energy of the state where we assume that in addition to a free rotation around the preceding bond axis, the bond $\boldsymbol{r}_i$ can distort and form an individual bond angle γ_i and bond length a_i, but only under an energy penalty of $E(a_i, \gamma_i)$.

Using passive rotation matrices [22, 93] one can show that the connectivity operator evaluates for our model to

$$\boldsymbol{\mathcal{C}}(\boldsymbol{\Gamma}_i, \boldsymbol{\Gamma}_{i-1}; a_i, \gamma_i) = \int_0^{2\pi} \mathrm{d}\psi_i \, \delta\left(\theta_i - g(\theta_{i-1}, \gamma_i, \psi_i)\right) \times \delta\left((Z_i - Z_{i-1}) - a_i g(\theta_{i-1}, \gamma_i, \psi_i)\right) , \quad (5.3)$$

where $\delta(x)$ is the Dirac delta function. The characteristic function $g(\theta, \gamma, \psi)$ is given by

$$g(\theta, \gamma, \psi) = \arccos\left(\cos\theta \cos\gamma + \sin\theta \sin\gamma \cos\psi\right) . \quad (5.4)$$

Using a discretized $\boldsymbol{\Gamma}$ space, we calculate the transfer matrix to arbitrary precision for any given potential $E(a, \gamma)$. With that, it is possible to numerically integrate and iterate Eq. (5.1). For a polymer consisting of N monomers and $N-1$ real bonds, the final Green's function elaborates to

$$P_N(\boldsymbol{\Gamma}_N; \boldsymbol{\Gamma}'_1) = \int \cdots \int \prod_{i=2}^{N} \left[\mathrm{d}\boldsymbol{\Gamma}_i \, \boldsymbol{\mathcal{T}}(\boldsymbol{\Gamma}_i, \boldsymbol{\Gamma}_{i-1})\right] P_1(\boldsymbol{\Gamma}_1; \boldsymbol{\Gamma}'_1) , \quad (5.5)$$

i.e. the transfer matrix is applied $N-1$ times on the Green's function of the initial monomer $P_1(\boldsymbol{\Gamma}_1; \boldsymbol{\Gamma}'_1)$. For the starting configuration $\boldsymbol{\Gamma}'_1$, the monomer position is chosen to be at $z = Z_1 = 0$. The virtual bond $\boldsymbol{r}_1$ points from all directions to the first monomer 1, hence the distribution function P_1 becomes a delta function in $\hat{z}$ space and a uniform distribution in θ space. By that, all orientations of the first real bond $\boldsymbol{r}_2$ are equally probable. In principle, it is possible to use an explicit starting bond direction. This can be useful for describing the bending rigidity of rigid chains with very stiff chain anchors.

External potentials and forces, such as the pulling force in an AFM or a tweezers experiment, are included by a convolution of an additional Boltzmann factor. For the Gibbs ensemble, in which the variable of control is the external force on the last monomer, F, the Green's function becomes

$$P_N^{\mathrm{G}}(\boldsymbol{\Gamma}_N; \boldsymbol{\Gamma}'_1, F) = P_N(\boldsymbol{\Gamma}_N; \boldsymbol{\Gamma}'_1) \times \exp\left(\frac{FD}{k_{\mathrm{B}}T}\right) . \quad (5.6)$$

When the height of the AFM cantilever, Z_{c}, or accordingly the tweezer focus is controlled, a convolution with the term $\exp\left(-k_{\mathrm{c}}(Z_{\mathrm{c}} - Z_N)^2/2k_{\mathrm{B}}T\right)$ can be done, where k_{c} is the bending force constant of the cantilever or the optical trap. This is often slightly inaccurately called a Helmholtz ensemble [92]. In this work, we limit the discussion of force-extension relations to those obtained in the Gibbs ensemble.

Observables of interest can now be calculated using the Green's function as a distribution weight. In the Gibbs ensemble the mean polymer extension as a function of the applied force, $\langle D\rangle = \langle Z_N - Z_1\rangle$, elaborates to

$$\langle D\rangle(F) = \frac{\int \mathrm{d}\mathbf{\Gamma}_N\, D P_N^{\mathrm{G}}(\mathbf{\Gamma}_N;\mathbf{\Gamma}_1', F)}{\int \mathrm{d}\mathbf{\Gamma}_N\, P_N^{\mathrm{G}}(\mathbf{\Gamma}_N;\mathbf{\Gamma}_1', F)}\,. \tag{5.7}$$

Equivalently, but for numerical reasons less favorable, the observables can be obtained from the partition function

$$\mathcal{Z}^{\mathrm{G}}(F) = \int \mathrm{d}\mathbf{\Gamma}_N\, P_N^{\mathrm{G}}(\mathbf{\Gamma}_N;\mathbf{\Gamma}_1', F) \tag{5.8}$$

by its logarithmic derivative with respect to the conjugate variable,

$$\langle D\rangle(F) = k_{\mathrm{B}}T\frac{\partial \ln \mathcal{Z}^{\mathrm{G}}(F)}{\partial F}\,. \tag{5.9}$$

Other observables and their fluctuations can be obtained accordingly.

Instead of using a convolution as in Eq. (5.6), it is possible to directly include the thermal weights due to any external field or potential into the transfer process Eq. (5.5) by using a modified transfer operator,

$$\boldsymbol{\mathcal{T}}'(\mathbf{\Gamma}_i,\mathbf{\Gamma}_{i-1}) = \boldsymbol{\mathcal{T}}(\mathbf{\Gamma}_i,\mathbf{\Gamma}_{i-1})\exp\left(-\frac{E(\mathbf{\Gamma}_i,\mathbf{\Gamma}_{i-1})}{k_{\mathrm{B}}T}\right), \tag{5.10}$$

which includes an additional energy weight due to the bond configurations $\mathbf{\Gamma}_j = \{Z_j, \theta_j\}$. This is necessary for *inhomogeneous* external fields, *e.g.* those exerted by an impenetrable wall ($E(Z_j < 0) = \infty$) or any other situation with $\hat{z}$ dependent *force.* An external force imposed on one end of the polymer chain while the other end is held fixed is equivalent to a *homogeneous* field F independent of the monomer position Z_j or the bond orientation θ_j, thus both methods are applicable. With Eq. (5.10), a denser integration grid and hence higher precision is possible which is advantageous for obtaining the asymptotic elastic behavior [93]. For our rather sophisticated model we have two dimensions in the P_i integration space ($\mathbf{\Gamma}_j = \{Z_j, \theta_j\}$) and three additional dimensions in the $\boldsymbol{\mathcal{T}}$ space (ψ, b and γ). The typical discretization in the $\boldsymbol{\mathcal{T}}$ space is done as $\Delta Z_{i-1}/a_{\mathrm{max}} = 401$ and $\Delta(\cos\theta_{i-1}) = \Delta(\cos\theta_i) = 401$; typical integration grids are $\Delta\psi/2\pi = 10^4$, $\Delta a/(a_{\mathrm{max}}-a_{\mathrm{min}}) = 100$, and $\Delta\gamma/(\gamma_{\mathrm{max}}-\gamma_{\mathrm{min}}) = 100$. Here Δx denotes the integration or discretization step size in quantity x, and x_{min} and x_{max} are the minimum and maximum value in that quantity, respectively. With the number of bonds being of the order of $50 \leq N-1 \leq 450$, it is with current computer power not feasible to perform highly discretized transfer matrix procedures using Eqs. (5.5) and (5.10), since the time consuming iteration process needs to be done for each value of the force. We therefore only report results obtained by the method using a subsequent force convolution, *i.e.* Eqs. (5.5), (5.2), and (5.6).

5.1.2 Classical and new chain models in the DESC formalism

The form of the potential energy in Eq. (5.2), $E(a, \gamma)$, can be freely chosen. We perform tests mimicking a FJC with $E(a, \gamma) = \infty$ for all $a \neq a_0$ and different FRCs with $E(a, \gamma) = \infty$ for all $a \neq a_0$ or $\gamma \neq \gamma_0$. Thus, the bond length is fixed to a_0, and for the FRCs also the bond angle is fixed to γ_0. In Fig. 5.2 we compare the results by DESC with the exact and asymptotic solutions of the FJC. Its partition function is given by Eq. (4.11) and its force-extension relation for a polymer with N monomers and $N-1$ bonds reads

$$\langle D \rangle = (N-1) a_0 \, \mathcal{L}\left(\frac{F a_0}{k_\mathrm{B} T}\right) , \tag{5.11}$$

where $\mathcal{L}(x) = \coth x - x^{-1}$ is the Langevin function, cf. also Section 4.1, and $(N-1)a_0 = L$ can be identified with the contour length of the polymer. For clarity, the DESC data points (crosses) have been reduced in density. The exact FJC relation (solid line) is shown together with its asymptotic solution for small forces (dotted line),

$$\langle D \rangle = (N-1) a_0 \, \frac{F a_0}{3 k_\mathrm{B} T} , \tag{5.12}$$

and the asymptotic solution for large forces (dashed line),

$$\langle D \rangle = (N-1) a_0 \left(1 - \frac{k_\mathrm{B} T}{F a_0}\right) , \tag{5.13}$$

As usual, we use rescaled units $\tilde{F} = F a_0 / k_\mathrm{B} T$ and $D/L = D/(N-1)a_0$. The agreement of the numerical DESC data points, whose density is reduced for clarity, with the exact solution proves to be excellent.

We further check FRC models in the DESC code against an independent numerical code [93, 156]. The results are equivalent. In Fig. 5.3 we show FRC force-extension data for $\gamma = 10^\circ$ (short-dashed line), 30° (dot-dashed), 45° (finely dotted), 60° (dot-dot-dashed), 70.529° (solid), and 80° (dotted). For comparison, the FJC solution (dashed) is also included, and for clarity the results of the benchmark code are omitted. We use $N-1 = 100$ bonds, for which the FRC models yield results converged to the $N \to \infty$ limit. Fig. 5.3 shows the intuitive result that FRC polymers with smaller bond angle are more easily stretched into their maximal length than those with larger bond angle or than an FJC.

Similarly we test the DESC performance using a FJC with a harmonic bond potential $V(a) = k/2(a-a_0)^2$. Its exact partition function for one bond is given by

$$\begin{aligned}\mathcal{Z}(F) &= \int_0^\pi \mathrm{d}\theta \, \sin\theta \int_0^\infty \mathrm{d}a \, a^2 \exp\left(\frac{F a \cos\theta}{k_\mathrm{B} T} - \frac{k}{2 k_\mathrm{B} T}(a-a_0)^2\right) \\ &\propto \frac{1}{F}\left(\frac{k_\mathrm{B} T}{k}\right)^{3/2} \exp\left(\frac{F^2 - 2 F k a_0}{2 k k_\mathrm{B} T}\right) J(F) , \end{aligned} \tag{5.14}$$

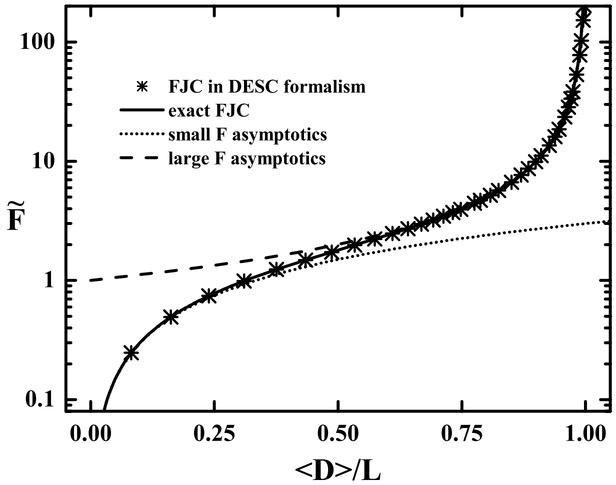

Figure 5.2: Rescaled force $\tilde{F} = Fa_0/k_\mathrm{B}T$ as a function of the average rescaled polymer end-to-end distance in the force direction, $\langle D\rangle/L = \langle D\rangle/a_0(N-1)$, for a FJC. The exact solution Eq. (5.11) is shown as solid line, the asymptotic behavior for the low force regime Eq. (5.12) as dotted line, the high force asymptotic solution Eq. (5.13) as dashed line. The numerical FJC data produced with the DESC formalism is reduced in density and shown as crosses; the exact solution is reproduced.

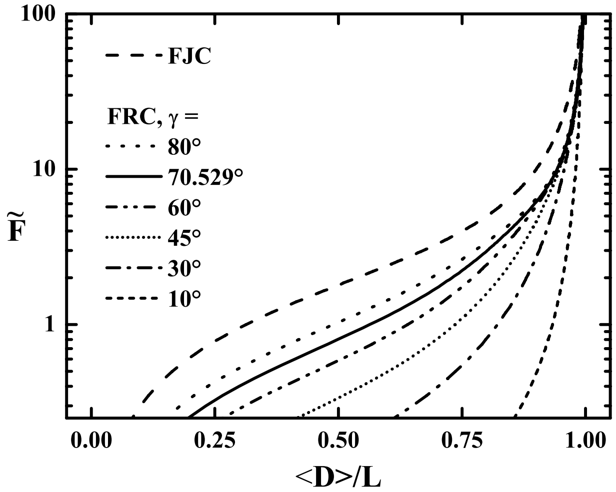

Figure 5.3: Rescaled force $\tilde{F} = Fa_0/k_\mathrm{B}T$ as a function of the average rescaled polymer end-to-end distance in the force direction, $\langle D\rangle/L$, for a FJC and various FRC chains. In the case of the FJC the polymer contour length is $L = (N-1)a_0$, for the FRC models it is $L = (N-1)a_0\cos(\gamma/2)$. The number of bonds is $N-1 = 100$ for which the FRC curves converge to the $N \to \infty$ limit. The FRC bond angles range from 10° to 80°, see legend. 70.529° is the tetrahedral angle applicable to most alkanes.

where we use

$$J(F) = \exp\left(\frac{2Fa_0}{k_{\mathrm{B}}T}\right)\left[1 + \mathrm{Erf}\left(\frac{F + ka_0}{\sqrt{2kk_{\mathrm{B}}T}}\right)\right](F + ka_0) \\ + \left[1 - \mathrm{Erf}\left(\frac{F - ka_0}{\sqrt{2kk_{\mathrm{B}}T}}\right)\right](F - ka_0)\,, \quad (5.15)$$

and the error function $\mathrm{Erf}(x) = 2/\sqrt{\pi}\int_0^x \mathrm{d}t \exp\left(-t^2\right)$. Thus the exact force-extension law becomes

$$\begin{aligned} \langle D\rangle = \frac{N-1}{Fk\,J(F)} \exp\left(-\frac{F^2 + k^2 a_0^2}{kk_{\mathrm{B}}T}\right) & \\ \times \Bigg\{ 2Fa_0 k^{3/2}\sqrt{\frac{2k_{\mathrm{B}}T}{\pi}} \exp\left(\frac{(F + ka_0)^2}{2kk_{\mathrm{B}}T}\right) & \\ + \exp\left(\frac{(F + ka_0)^2}{kk_{\mathrm{B}}T}\right)[F(F + ka_0)^2 - k^2 a_0 k_{\mathrm{B}}T]\left[1 + \mathrm{Erf}\left(\frac{F + ka_0}{\sqrt{2kk_{\mathrm{B}}T}}\right)\right] & \\ + \exp\left(\frac{F^2 + k^2 a_0^2}{kk_{\mathrm{B}}T}\right)[F(F - ka_0)^2 + k^2 a_0 k_{\mathrm{B}}T]\left[1 - \mathrm{Erf}\left(\frac{F - ka_0}{\sqrt{2kk_{\mathrm{B}}T}}\right)\right]\Bigg\}\,. & \quad (5.16) \end{aligned}$$

In the literature, the approximation of splitting the entropic FJC part from the enthalpic stretching contribution is often applied, cf. Refs. [18, 150] and references therein, and a force law according to

$$\langle D\rangle = (N-1)a_0\left(1 + \frac{F}{ka_0}\right)\mathcal{L}\left(\frac{Fa_0}{k_{\mathrm{B}}T}\right) \quad (5.17)$$

is used. In Fig. 5.4 we show the results for the extensible FJC model in the DESC formalism (circles, reduced in density), its analytical solution Eq. (5.16) (red line), the approximation Eq. (5.17) (green dashed line), and the inextensible standard FJC solution Eq. (5.11) (blue line). In Ref. [91] stretching moduli for different polymer backbones are calculated. Considering only the harmonic contribution and rescaling the force constants, these authors give $\tilde{k} = ka_0^2/k_{\mathrm{B}}T = 4940$ for polypeptides, $\tilde{k} = 1820$ for alkanes, and $\tilde{k} = 1480$ for ss-DNA. For the extensible FJC test case we choose a stretching force constant of $\tilde{k} = 1000$ which is a lower bound of a realistic polymer bond stretching modulus. The DESC data nicely reproduces the exact solution. Additionally the approximation of independent entropic and enthalpic stretching, Eq. (5.17), works very well for $\tilde{k} = 1000$ in the FJC case. Pronounced deviations in the regime $0 \leq D/(N-1)a_0 \leq 1.5$ only occur for $\tilde{k} < 100$ which is not relevant for polymers. As an exemplary case we show in Fig. 5.5 the breakdown of the approximative formula (dashed line) with respect to the exact solution (solid line) for $\tilde{k} = 10$. In the inset, the rescaled force is drawn on a logarithmic scale.

In a similar way as for the FJC, bond elasticity has been taken into account in FRC models by a separation of the entropic and enthalpic contributions [91, 148, 157]. With the DESC method we test this approximation, again using $\tilde{k} = 1000$

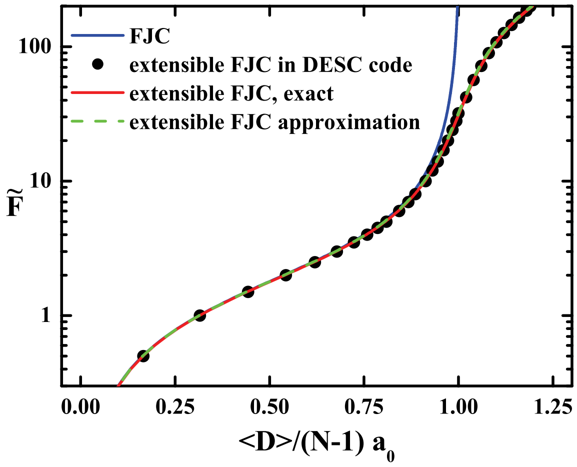

Figure 5.4: Rescaled force $\tilde{F} = Fa_0/k_\mathrm{B}T$ as a function of the average rescaled polymer end-to-end distance in the force direction, $\langle D\rangle/(N-1)a_0$, for a FJC and an extensible FJC with $\tilde{V} = V/k_\mathrm{B}T = \tilde{k}(a/a_0-1)^2/2$, where we choose $\tilde{k} = 1000$. Data is shown for the FJC, Eq. (5.11), as blue line, for the exact solution of the extensible FJC, Eq. (5.16), as red line, for the approximative extensible FJC, Eq. (5.17), as dashed green line. Numerical data for the extensible FJC is produced with the DESC formalism and shown reduced in density as solid circles; the exact solution is reproduced. For $\tilde{k} = 1000$ which is a lower realistic bound for polymers, the approximative formula coincides with the exact solution and the DESC data.

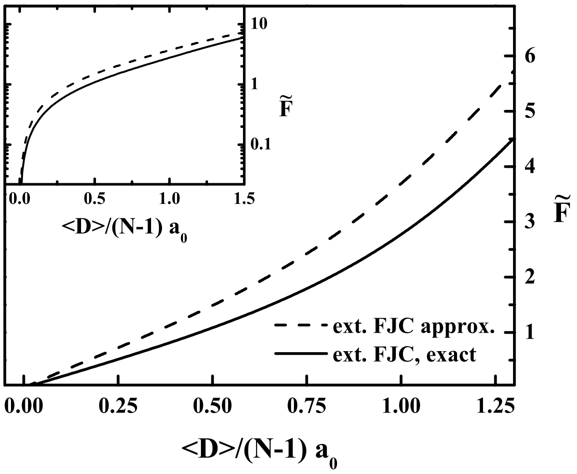

Figure 5.5: Rescaled force $\tilde{F} = Fa_0/k_\mathrm{B}T$ as a function of the average rescaled end-to-end distance in the force direction, $\langle D\rangle/(N-1)a_0$, for an extensible FJC with $\tilde{V} = V/k_\mathrm{B}T = \tilde{k}(a/a_0-1)^2/2$. A rather weak elastic modulus of $\tilde{k} = 10$ is chosen as *not* applicable to polymers. The exact solution, Eq. (5.16), is shown as solid line, the approximative formula, Eq. (5.17), as dashed line. The inset shows the force on a logarithmic scale.

and bond angles of $30^\circ \leq \gamma \leq 80^\circ$ for extensible FRC chains with $N-1=100$ bonds. In Fig. 5.6 we show the exact DESC results as data points which we reduce in density for clarity. The lines denote force-extension relations that are obtained from the data for an *inextensible* FRC, $\langle D \rangle_{\text{inext}}$, by a convolution with an enthalpic stretching part to yield the values for the *extensible* FRC, $\langle D \rangle_{\text{ext}}$, as

$$\langle D \rangle_{\text{ext}} = \langle D \rangle_{\text{inext}} \left(1 + \frac{F}{ka_0} \right) . \tag{5.18}$$

The numerically exact force relation for the inextensible FRC is taken from the DESC calculations presented before. In Fig. 5.6a) a generally good agreement of the approximative formula (lines) with the exact data (data points) is observed. In b) we present an excerpt on a linearly scaled force axis indicating slight deviations in the range $0.875 < \langle D' \rangle < 1.0$, where $D' = D/(N-1)a_0 \cos(\gamma/2)$ is the maximum contour length of the corresponding inextensible FRC. These deviations increase with decreasing bond angle and hence increasing entropic stiffness. For $\gamma = 30^\circ$ and $\langle D' \rangle = 0.975$ we have $\tilde{F} = 12.5$ from Eq. (5.18) and $\tilde{F} = 11.5$ from the exact treatment and hence a 9 % overestimate by the use of the approximative approach. As expected, the deviation also decreases when going to very large forces and end-to-end distances, $\langle D' \rangle > 1.0$, and also with increasing enthalpic chain stiffness. The latter is checked by using $\tilde{k} = 1820$ and $\tilde{k} = 5000$ as has been suggested for alkanes and polypeptides, respectively [91]. At the same point in the force-extension curve and again for $\gamma = 30^\circ$, the relative deviation drops from 9 % ($\tilde{k} = 1000$) over 6 % ($\tilde{k} = 1820$) to 2 % ($\tilde{k} = 5000$). We conclude that splitting the elasticity into entropic and enthalpic contributions as in Eq. (5.18) is a valid approximation for many polymers. However, in the case of polymers with small bond angles such as poly-p-phenylenes and poly-pyrroles [158, 159] an exact treatment becomes more important. How well scaling formulae [93] perform with extensible FRCs has yet to be determined.

In this section we limit our considerations to the cases described above. The full capability of the DESC model is still to be explored since virtually any potential energy function in the a-γ space can be used. We have performed further calculations with different chains models, such as the elastically jointed chain (a fixed, $V \propto -\cos\gamma$) [93, 160], the discrete persistent chain ($V \propto \gamma^2$) [161] and their extensible variants. We have also verified the functionality of potential energy functions including semi-flexibility with models such as the semi-flexible harmonic chain ($V \propto \cos\gamma + k/2(a-a_0)^2$) [154]. Taking higher order terms than harmonic stretching and bending constants into account is easily done as will be demonstrated in Section 5.2 where alternating copolymers are discussed. For the case of alkanes, for which DESC can be assumed to include all important elasticity features, *ab initio* calculations are currently performed to map out the microscopic bond potentials in great detail. These will later be introduced into the DESC formalism.

To summarize, the discrete extensible semi-flexible chain (DESC) model allows for the thermodynamically exact treatment of bond elasticity going beyond the freely rotating chain (FRC) model. A slight overestimation of the common approximative

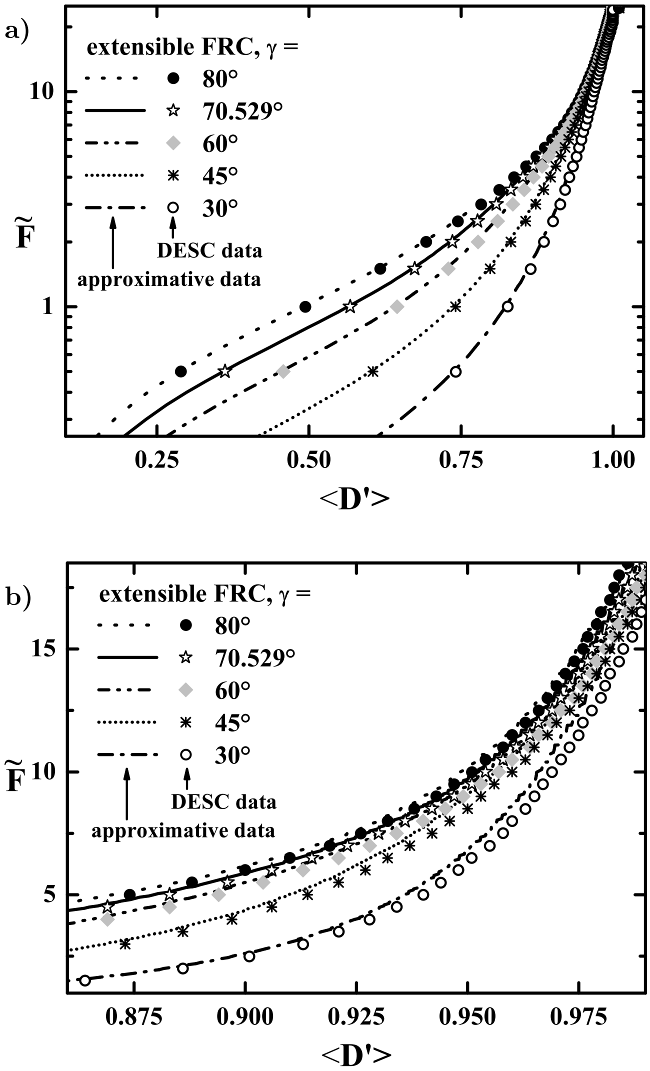

Figure 5.6: Rescaled force $\tilde{F} = Fa_0/k_\mathrm{B}T$ as a function of the average rescaled end-to-end distance in the force direction, $\langle D'\rangle = \langle D\rangle/(N-1)a_0\cos(\gamma/2)$ for an extensible FJC with $\tilde{V} = V/k_\mathrm{B}T = \tilde{k}(a/a_0-1)^2/2$. The microscopic elasticity constant is chosen as $\tilde{k} = 1000$, which serves as an approximate lower bound for polymers [91]. The exact DESC data is reduced in density and shown as data points, see also legend. DESC data for inextensible FRCs are converted using the approximative formula Eq. (5.18) and shown as lines. Generally reasonable agreement between the approximation and the exact data is observed. An excerpt of **a)** is presented in **b)** on a linear force scale indicating a maximal deviation of the approximation from the exact result of about 9 % for $\gamma = 30°$ at $\langle D'\rangle = 0.975$ where $\tilde{F} = 12.5$ from the approximation and $\tilde{F} = 11.5$ from the exact DESC treatment.

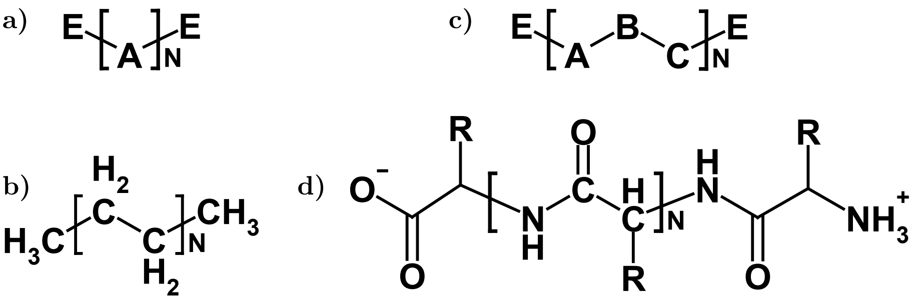

Figure 5.7: **a)** Homopolymer with N units of the same type A and end groups. **b)** poly(ethylene), homopolymer where only one bond type along the backbone appears: $\mathrm{RCH_2 - CH_2R}$. **c)** Alternating copolymer with regularly alternating monomers A, B, and C. **d)** Polypeptide; concerning chemical monomers or coarse-grained monomers, *i.e.* the amino acids, it belongs to the class of homopolymers; concerning chemical bond types, it is an example of an alternating copolymer.

approach based on the splitting of entropic and enthalpic elasticities is revealed for extensible FRCs with small bond angles.

5.2 Polypeptides as alternating copolymers

Homopolymers are polymers that consist of only one type of monomer, as schematically depicted in Fig. 5.7a). The classical example for such a macromolecule is poly(ethylene), the simplest alkane polymer, Fig. 5.7b). From a chemical point of view there are many macromolecules considered as homopolymers which do involve different bonds along the backbone, *e.g.* polypeptides, see Fig. 5.7d). This is so because the chemical unit considered as a monomer is in this case a peptide unit consisting of different atoms. Although coarse-graining procedures taking into account the enthalpic elasticity of the whole chemical monomer, such as the peptide unit, are quite successful [91, 148], it is straightforward to generalize the transfer matrix formalism introduced in Section 5.1.1 for the case of microscopic copolymers. In the simplest case these copolymers have regularly alternating bonds, see Fig. 5.7c). In a microscopic picture in which we take account of each bond along the backbone, polypeptides can be regarded as one example of an alternating copolymer.

To describe the elastic behavior of polypeptides, their side chains R, are of minor importance as has been shown before [91]. Following these findings we take poly(glycine) (R = H) as our generic model for polypeptide elasticity, cf. Fig. 5.8a) and b). Three different bonds types are identified: the $\mathrm{RC(O) - NHR}$ bond (1), the $\mathrm{RHN - CH_2R}$ bond (2), and the $\mathrm{RH_2C - C(O)R}$ bond (3) with each a corresponding bond angle $\gamma^{(i)}$ and a bond length $a^{(i)}$. Three fragments with each three backbone atoms are built, see Fig. 5.8c)-e). The corresponding bond potential is assumed to be additive, $V^{(i)}(\gamma, a) = V_\gamma^{(i)}(\gamma) + V_a^{(i)}(a)$. These potentials are determined by density functional theory (DFT) calculations [26] using Gaussian03 [162]. The hybrid potential B3LYP [163, 164] together with the basis set 6-311++G** [165, 166] is employed. The geometries are optimized into minima. These optimized structures are then again optimized using a single constraint on one of the bond lengths $a^{(i)}$ or one angle $\gamma^{(i)}$. This procedure is repeated for a series of values for both the bond length and the angle to obtain a detailed energy landscape. Note that our *ab initio* calculations are done at zero temperature. However, the dependence of the microscopic moduli on the temperature is estimated to be much smaller than the entropic effects, which are later taken into account by the DESC model. Also, the *ab initio* calculations only include the polymer fragment and hence reflect the situation in vacuo. Still, the results prove to be quantitatively useful [91]. Small deviations only occur in polar solvents such as water and can be used to extract solvent effects quantitatively [157].

The energy profiles for the three different bonds are plotted in Fig. 5.9. a) shows the coordinate system: The previous bond $\boldsymbol{r}_{j-1}$ and the actual bond $\boldsymbol{r}_j$ are rotated into the $\hat{x}$-$\hat{y}$ plane. Bond $\boldsymbol{r}_{j-1}$ points in the $\hat{y}$ direction and the monomer connecting bonds $\boldsymbol{r}_{j-1}$ and $\boldsymbol{r}_j$ is at the origin $(0, 0)$. The orientation and the end point of the actual bond are thus coded by an inverse polar coordinate transformation. The same coordinate system is used in Fig. 5.9b) to d) showing the potential energy by color coded contours for the bonds (1), (2), and (3), respectively.

The bond energies obtained from *ab initio* quantum chemistry calculations now serve as input to calculate the transfer matrix for each bond type (i), $\boldsymbol{\mathcal{T}}^{(i)}(\boldsymbol{\Gamma}_j, \boldsymbol{\Gamma}_{j-1})$. Eq. (5.5) is modified by applying the transfer matrices in alternating order, thus

$$P_N(\boldsymbol{\Gamma}_N;\boldsymbol{\Gamma}'_1) = \int ... \int \prod_{j=2}^{N} \Big[\mathrm{d}\boldsymbol{\Gamma}_j\, \boldsymbol{\mathcal{T}}^{(3)}(\boldsymbol{\Gamma}_j, \boldsymbol{\Gamma}_l) \\ \mathrm{d}\boldsymbol{\Gamma}_l\, \boldsymbol{\mathcal{T}}^{(2)}(\boldsymbol{\Gamma}_l, \boldsymbol{\Gamma}_k)\; \mathrm{d}\boldsymbol{\Gamma}_k\, \boldsymbol{\mathcal{T}}^{(1)}(\boldsymbol{\Gamma}_k, \boldsymbol{\Gamma}_{j-1})\Big]\, P_1(\boldsymbol{\Gamma}_1;\boldsymbol{\Gamma}'_1)\,, \quad (5.19)$$

where the indices k, l are different for each j. This procedure has been followed in the DESC formalism with the above bond potentials for polypeptides. The resulting force-extension data for polymers with $N = 50$ (dashed line), $N = 100$ (solid line), and $N = 150$ (dotted line) are shown in Fig. 5.10a). In b) we plot the normalized force curves, *i.e.* F as a function of $\langle D\rangle/N$. All data is collapsed indicating that the limit $N \to \infty$ is reached and suggesting that the DESC/alternating copolymer code yields useful results. A more detailed analysis of the data including a comparison with experimental data is in progress.

In summary, the transfer matrix formalism can be extended for the case of alternating copolymers. Under a microscopic interpretation, polypeptides are examples of alternating copolymers since their constitutents, the amino acids have three different backbone atoms. Quantum chemistry has been used to obtain the polypeptide bond stretching and bending potential. This potential energy landscape has been used to generate force-extension data for polypeptides within the DESC/alternating copolymer formalism. The ease of implementing different bonds into the transfer

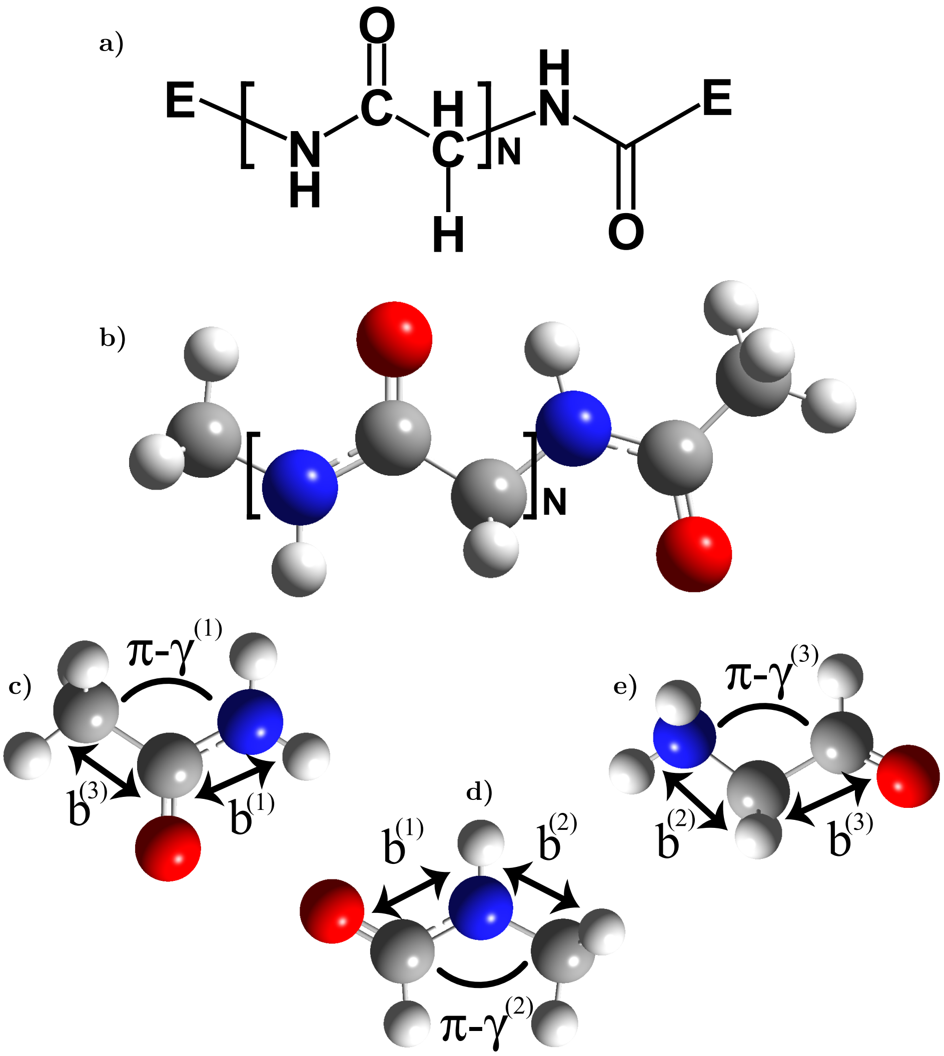

Figure 5.8: **a)** and **b)** Poly(glycine) as a generic form of polypeptides. **c)**, **d)**, and **e)** Polypeptide fragments from which bond potentials are calculated. Three bonds with $V^{(i)}(\gamma^{(i)}, a^{(i)}) = V_{\gamma}^{(i)}(\gamma^{(i)}) + V_{a}^{(i)}(a^{(i)})$, $i \in \{1, 2, 3\}$, are defined. Quantum chemistry is used to calculate these bond potentials: In each of the fragments the angle is bent to obtain the bond angle potential, and in each of the fragments both bond lengths are stretched and compressed in independent calculations.

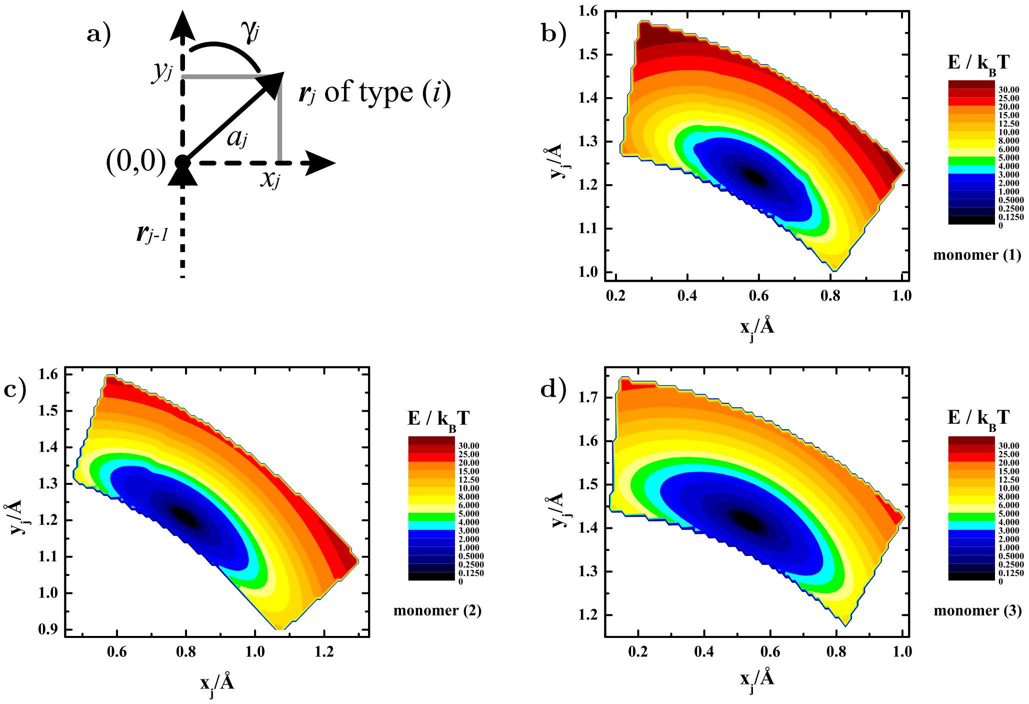

Figure 5.9: Microscopic bond potentials for a polypeptide molecule. **a)** Coordinate system: Both previous bond $\boldsymbol{r}_{j-1}$ and actual bond $\boldsymbol{r}_j$ are in the $\hat{x} - \hat{y}$ plane; $\boldsymbol{r}_{j-1}$ points in the $\hat{y}$ direction; the monomer connecting both bonds is at the origin $(0, 0)$. The actual bond is of type (i), with $i \in \{1, 2, 3\}$. Different bond lengths a_j and angles γ_j of the actual bond are coded by an inverse polar coordinate transformation $a_j^2 = x_j^2 + y_j^2$, $\tan \gamma_j = x_j / y_j$. **b)** Energy for bond (1), **c)** for bond (2), **d)** for bond (3). For definitions of bond numbering, see Fig. 5.8.

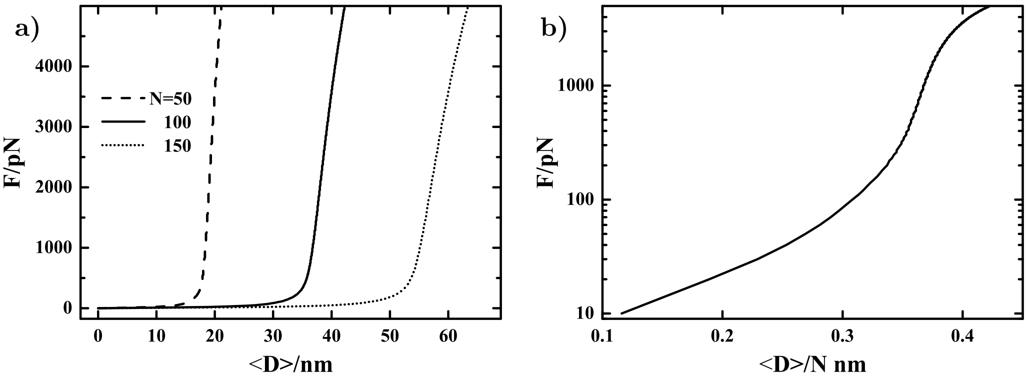

Figure 5.10: Force extension data for a generic polypeptide (polyglycine). Data is calculated using the alternating copolymer formalism and the DESC method (FRC with bendable and stretchable bonds). The bond potentials of the three individual bond types are calculated from *ab initio* quantum chemistry, see also Fig. 5.9. **a)** Force F as a function of the end-to-end distance, $\langle D\rangle$, for chains of different length: $N = 50$ (dashed line), $N = 100$ (solid line), $N = 150$ (dotted line), where N is the number of amino acids in the chain. **b)** F on a logarithmic scale *vs.* the rescaled length, $\langle D\rangle/N$. Curves for different N collapse indicating that the limit $N \to \infty$ is reached.

matrix method might prove useful for calculating the elastic properties of block copolymers, and even statistic or random copolymers, given that sufficient computational resources are present.

5.3 Rotational rigidity in polypeptides and a modified FRC model

In the previous sections we have assumed that free rotation around the previous bond axis is a valid approximation. All of the discrete models studied and reviewed in this chapter so far rely on the assumption of evenly distributed values of ψ, see Fig. 5.1. Indeed, for many classes of polymers this procedure is legitimate. In the case of alkanes, *e.g.*, it is known that their *cis* and *gauche* conformations have different energies [107, 152]; however for already small pulling forces these rotational barriers are overcome and hence extensible FJC and FRC models reproduce experimental data within high precision [91]. For the case of proteins and polypeptides it is known that a much larger rotational barrier exists [167, 168]. This is due to a partial double bond character of the RC(O) − NHR bond (1) caused by mesomeric states and resonance effects, see Fig. 5.11. The hindrance of rotation and the mostly planar N − C(O) − C group is also one of the reasons for β sheet formation. From nuclear magnetic resonance (NMR) studies and crystallographic analysis Ramachandran plots can be generated [167]. They show that in the native forms

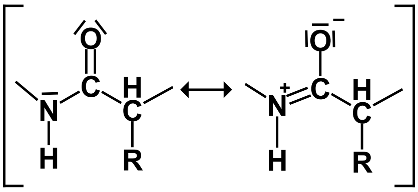

Figure 5.11: Resonance effect leading to increased rotational rigidity in polypeptides. Rotation around the RC(O) – NHR bond (1) is hindered due to its partial double bond character. In the case of native and crystallized proteins, the *cis* state depicted here is known to be less populated than the *trans* configuration.

of proteins the *cis* conformation that is depicted in Fig. 5.11 is less populated than the *trans* conformation in which the chain adopts a zig-zag form. However, at least in the native state and the crystallized form, other conformations than these planar configurations, play only a negligible role.

At this point it is interesting to see if rotational barriers are still of concern for polypeptides when an external force is applied. This might have severe consequences for folding and unfolding events *in vivo*, since these processes could in principle be greatly enhanced in their kinetics and even the equilibrium could be shifted from one structure to another. The rotational barrier can be checked, again using quantum chemistry methods. Following the same procedure as in Section 5.2, *ab initio* calculations are performed where one of two dihedral angles $\psi^{(1)}$ or $\psi^{(2)}$ is constrained, cf. also sketch in Fig. 5.12a). Note that rotating bond (1) probes the $\psi^{(2)}$ potential, and rotation of bond (3) changes $\psi^{(1)}$, see also Fig. 5.1c) for the nomenclature. The torsional potential is shown in b) as a dotted line and filled diamonds for $\psi^{(1)}$, and as a solid line and empty circles for $\psi^{(2)}$. As expected, bond (1) is much more inelastic with respect to torsional strain and thus rotation of $\psi^{(2)}$ is hindered. Not only are the minima in the case of $\psi^{(2)}$ separated by barriers considerably larger than $10\,k_{\mathrm{B}}T$, but the curve is also much steeper indicating higher restoring forces. We conclude that it is an oversimplification to freely rotate bond (1) in a FRC model or a DESC analogue.

A further improvement addressing this issue is the incorporation of an effective, stiff bond into the DESC or FRC formalism. This is demonstrated in Fig. 5.13. We introduce a new effective bond with a bond length $a^{(e)}$ and two bond angles $\gamma^{(e)}$ and $\beta^{(e)}$, which spans *two* microscopic, real bonds, cf. Fig. 5.13c). The first of these two bonds merged into the effective bond is the RC(O) – NHR bond (1) around which rotation is prohibited. A new bond angle $\beta^{(e)}$ is needed which rotates the axis of the previous bond to that of the second microscopic bond within the effective bond. Which second bond merges into the effective bond depends on the direction A or B of building up the polymer, see Fig. 5.13a) and b). To keep the methodology simple in the beginning, we start parameterizing DESC with fixed bond lengths and angles, *i.e.* with an effective bond FRC. The parameters are taken from the ground

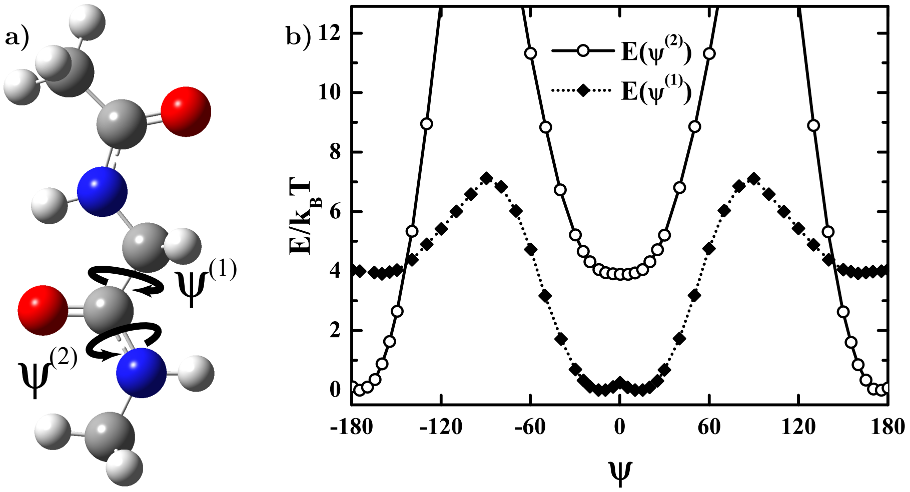

Figure 5.12: **a)** Dimer molecule for which the *ab initio* calculations are done and the numbering of the torsional angles. **b)** Torsional potentials of the bonds at the carbonyl C, bond (1) with $\psi^{(2)}$ and bond (3) with $\psi^{(1)}$. Rotation around the RC(O) – NHR bond (1), is strongly hindered due to its partial double bond character, see also Fig. 5.11. It is a poor approximation to freely rotate the dihedral angle $\psi^{(2)}$, rather it is fixed at either $\psi^{(2)} \approx 0°$ or $\approx 180°$.

state of the dimer calculation shown in Fig. 5.13 and are $a^{(e)} = 2.45\,\text{Å}$, $\gamma^{(e)} = 7.19°$, $\beta^{(e)} = 35.47°$, $a^{(f)} = 1.53\,\text{Å}$, and $\gamma^{(f)} = 70.97°$ for the building direction A. For direction B we have $a^{(e)} = 2.44\,\text{Å}$, $\gamma^{(e)} = -7.19°$, $\beta^{(e)} = 23.46°$, $a^{(f)} = 1.44\,\text{Å}$, and $\gamma^{(f)} = 70.97°$. Bond (f) is in both cases a standard FRC bond, so the only change in the transfer matrix formalism has to be done in the connectivity operator for the effective bond (e). Eq. (5.3) is modified and reads for the effective bond

$$\boldsymbol{\mathcal{C}}(\boldsymbol{\Gamma}_i, \boldsymbol{\Gamma}_{i-1}; a_i, \gamma_i, \beta_i) = \int_0^{2\pi} \mathrm{d}\psi_i \, \delta\left(\theta_i - g(\theta_{i-1}, \beta_i, \psi_i)\right) \\ \times \delta\left((Z_i - Z_{i-1}) - a_i g(\theta_{i-1}, \gamma_i, \psi_i)\right) . \quad (5.20)$$

The effective bond model is tested in the FRC implementation of the effective bond algorithm using $N = 150$ and $N = 200$ amino acids. Both building directions A and B, cf. Fig. 5.13, are used and give identical results. In Fig. 5.14a) the force extension data is shown for the effective FRC model with $N = 150$ (solid line) and $N = 200$ (dashed line). The DESC curve for $N = 150$ is also presented (dotted line). Since there is no enthalpic elasticity included in the effective bond algorithm yet, the force in that model diverges at the maximal polymer length. The results after rescaling by N are shown in b) where all effective FRC curves, *i.e.* for both building direction and both monomer numbers, collapse into the solid line suggesting

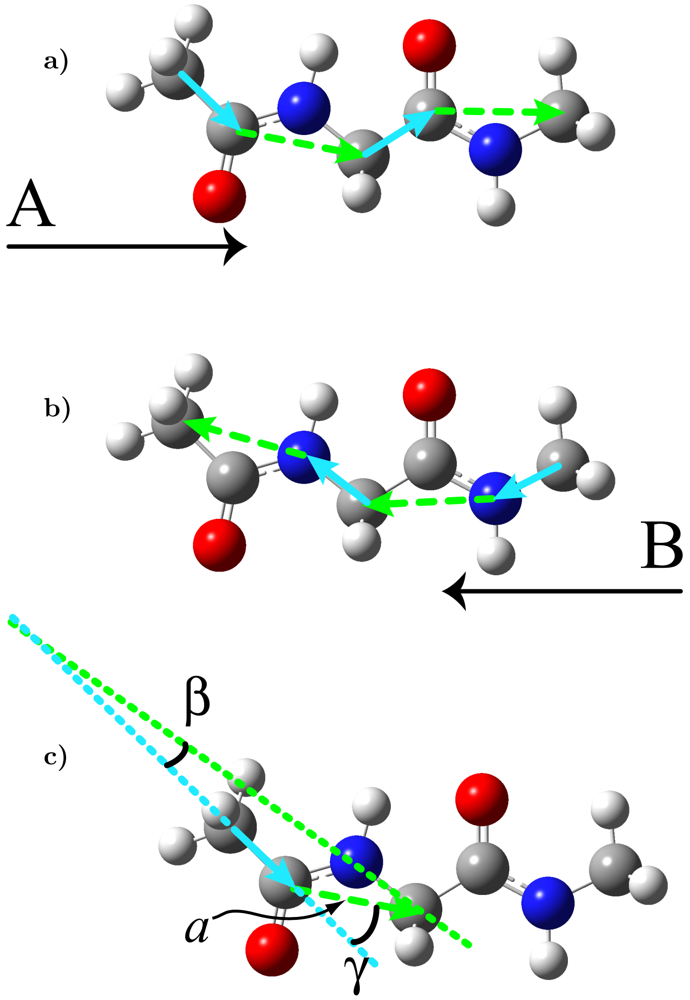

Figure 5.13: The effective bond model for the FRC or DESC formalism. Since rotation around the $\mathrm{RC(O)-NHR}$ bond (1) must be prevented, we introduce an effective bond which spans bond (1) and a second bond. In all cases, the new effective bonds are highlighted by green, dashed arrows. The cyan colored solid arrow denotes the remaining, normal FRC or DESC bond. **a)** and **b)** show the position of the effective bond depending on the building direction A (from C terminus to N terminus) and direction B (vice versa). The new parameterization of the effective bond is explained in **c)**. The new bond length a and angle γ are effective in the sense that they span two real bonds. A second bond angle β is needed which rotates the axis of the previous bond onto the axis of the second microscopic bond within the effective bond. For the second bond in the model (cyan) no changes in the FRC parameterization are needed.

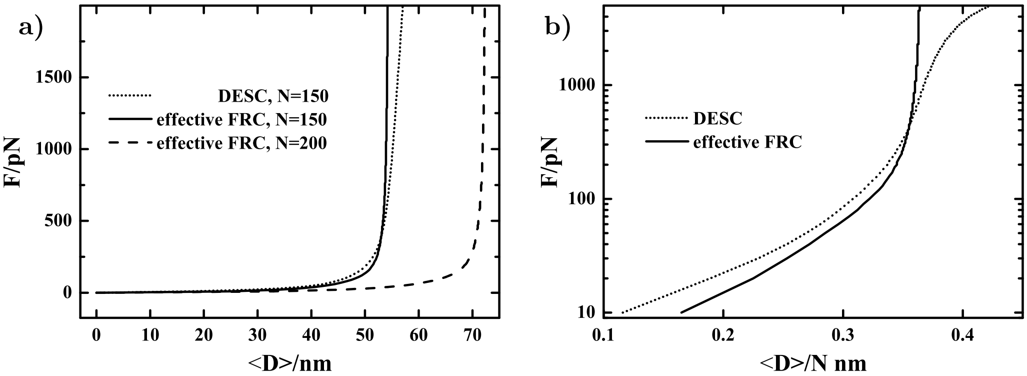

Figure 5.14: Force extension data for a generic polypeptide (polyglycine). **a)** Data is calculated using the FRC model extended by an effective bond addressing the torsional rigidity of the RC(O) − NHR bond: $N = 150$ amino acids (solid line), $N = 200$ amino acids (dashed line). DESC data as from Fig. 5.10 is also shown for $N = 150$ (dotted line). The effective bond FRC model has two inextensible and stiff bonds, one of which spans two microscopic bonds to account for the torsional rigidity, see text and Fig. 5.13 for details. The DESC model includes all three microscopic bonds with a bending and stretching potential for each. In **b)** we show the force as a function of the rescaled end-to-end distance, $\langle D\rangle/N$. All effective FRC versions collapse (solid line), *i.e.* those for the building direction A and B (see Fig. 5.12) and for both monomer numbers. The DESC curve is also shown (dotted line).

a properly working algorithm and the $N \to \infty$ limit. The DESC curve (dotted line) is also shown.

In summary, we have shown how to calculate polymer elasticities taking rotational barriers into account. Such hindrance of torsional rotation is present in polypeptides, but also many other polymers involving double or triple bonds in their backbone, such as polyacetylenes or azobenzene. We anticipate further improvement of polymer elasticity theory when taking stiff bonds as well as enthalpic extensibility and semi-flexibility as realized in the DESC model into account.

Chapter 6

Summary

The dynamics of single polymers at solid-liquid interfaces and their response to external fields are discussed using a wide arsenal of theoretical and numerical tools.

Chapter 1 highlights the motivation for studying these phenomena and describes the theoretical and experimental framework in this field. A short introduction into the theoretical methods used in this work is given.

In Chapter 2 we give an introductory view on the adsorption of an ideal polymer onto a flat, homogeneous surface. The diffusion equation approach is shown to be equivalent to a Poland-Scheraga description. Brownian dynamics (BD) simulations are described in which the adsorption of coarse-grained polymer chains to a flat surface is studied. Although the simulations have a finite duration and the polymer models are of finite length, we identify a regime in which the polymer is adsorbed strongly enough to the substrate and where it is possible to map the adsorption transition of a single, infinitely long polymer. A discussion on polymer adsorption as studied by force spectroscopy with atomic force microscopes (AFM) closes the chapter. We find that in the absence of friction effects, it is a good approximation to associate the desorption force with the free energy of adsorption per unit length.

Chapter 3 discusses the translational friction of polymers adsorbed to solid substrates, and in particular starts with an analysis of the influence of friction on the desorption forces measured with an AFM. It is shown by how much these forces increase with respect to the equilibrium value, and an experiment of how to measure frictional coefficients of polymers on surfaces is proposed. BD simulations with a Frenkel-Kontorova type model show how the interaction of a polymer with a corrugated surface potential increases the solvent drag and thus the friction forces on the polymer. The effect of (in)commensurability and the dependence on the polymer length is checked. Molecular dynamics simulations with atomistic models of a polypeptide, water, and a diamond surface are conducted. The simulations reveal a high lubricity of the polypeptide on a hydrophobic surface with mobilities comparable to the case of bulk water. On a hydrophilic, OH-terminated surface a pronounced stick-slip motion is found which is caused by the periodic breaking and formation of hydrogen bonds. As a result, the polypeptide mobility is reduced by a factor of at least thirty as compared to the hydrophobic surface. This is remarkable since the adsorption energies are of the same order of magnitude on both surfaces.

The adsorption of polymers far from equilibrium is studied in Chapter 4. We find that when a polymer is pulled on one end parallel to an adsorbing surface, it adsorbs more *easily*. The flattening of the chain due to pulling corresponds to a decrease of the effective Kuhn length normal to the surface. A calculation taking the Kuhn length into account reproduces the observed increase in adsorption within scaling precision. A similar effect is found for polymers in sheared solutions. Polymers close enough to the adsorption transition extend into the solution and are subjected to a flattening drag by the shear flow, hence they adsorb more strongly. For low temperatures or high adsorption strengths, the polymer is adsorbed to the surface in a flat configuration, thus the shear flow has no effect. Hydrodynamic interactions between the monomers and with a no-slip boundary wall have a reverse effect for both a polymer pulled at one end and a polymer in shear flow: The polymer is driven away from the surface and hence adsorption is reduced. At the same time the adsorption transition turns from a continuous into a discontinuous type. A single particle which is pulled parallel to a corrugated surface experiences on average a smaller adsorption energy than at equilibrium. As a result, the particle adsorption is reduced by pulling. A corresponding mechanism for a polymer pulled at one end over a corrugated surface is expected to be much weaker and to be dominated by the flattening effect.

The elasticity of single polymers is discussed in Chapter 5 on the basis of discrete polymer models incorporating microscopic bond parameters. A discrete extensible semi-flexible chain (DESC) is introduced extending the freely rotating chain (FRC) model by extensible and bendable bonds. The transfer matrix approach provides numerical solutions for DESC using bond potentials of any choice. For rod-like FRC polymers we show the breakdown of approaches separating entropic from enthalpic elasticity. The transfer matrix approach is extended to the case of alternating copolymers. Bond stretching and bending potentials are calculated for polypeptides with an *ab initio* method and applied in the alternating copolymer scheme. Polypeptide torsional rigidity is analyzed with quantum chemistry calculations, and one bond along the backbone is found to be hindered for rotation. A FRC model with an effective bond spanning two microscopic bonds is established for such cases. Polypeptide parameters are applied in this effective FRC formalism to obtain force-extension relations.

Future work on the discrete polymer models will consider a combination of the DESC model and the effective bond methodology. The effects of geometric surface corrugations on non-equilibrium polymer adsorption need to be further considered. When driven polymers are stretched by obstacles interesting adsorption phenomena are expected. A subtle interplay between geometric and chemical heterogeneity for patterned surfaces is likely. The friction of polymers on solid surfaces requires further studies, especially when it comes to more complicated geometries, such as pores or channels. For the detailed understanding of such processes models on the atomistic level are ultimately needed and require further improvement.

Parts of this thesis have been published in or submitted to peer-reviewed journals, or manuscripts for such contributions are in preparation. These contributions include

- A. Serr and R. R. Netz, Pulling adsorbed polymers from surfaces with the AFM: stick *vs.* slip, peeling *vs.* gliding, *Europhys. Lett.* **2006**, *73* (2), 292.
- A. Serr and R. R. Netz, Enhancing polymer adsorption by lateral pulling, *EPL* **2007**, *78* (6), 68006.
- D. Horinek, A. Serr, M. Geisler, T. Pirzer, U. Slotta, S. Q. Lud, J. A. Garrido, T. Scheibel, T. Hugel, and R. R. Netz, Single molecule peptide hydrophobicity results from the interplay of water structure effects and dispersion interaction, submitted to *Nature Mat.*, **2007**.
- D. Horinek, A. Serr, D. Bonthuis, and R. R. Netz, Hydrophobic attraction studied by molecular dynamics, submitted to *Langmuir*, **2007**.
- A. Serr, C. Sendner, and R. R. Netz, Non-equilibrium polymer adsorption, in preparation, **2007**.
- A. Serr, D. Horinek, and R. R. Netz, Polymer super-lubricity on hydrophobic *vs.* high-friction stick-slip motion on hydrophilic surfaces, in preparation, **2007**.
- A. Serr, F. Hanke, H. J. Kreuzer, and R. R. Netz, Stretching of discrete semi-flexible extensible polymer chains, in preparation, **2007**.
- F. Hanke, A. Serr, R. R. Netz, and H. J. Kreuzer, On the rotational rigidity and elastic response of polypeptides, in preparation, **2007**.

Other contributions related to this work, but not covered here have been published as

- H. Boroudjerdi, Y. W. Kim, A. Naji, R. R. Netz, X. Schlagberger, and A. Serr, Statics and dynamics of strongly charged soft matter, *Phys. Rep.* **2005**, *416* (3-4), 129.
- A. Serr and R. R. Netz, Polarizabilities of hydrated and free ions derived from DFT calculations, *Int. J. Quant. Chem.* **2006**, *106* (14), 2960.
- F. Kühner, M. Erdmann, L. Sonnenberg, A. Serr, J. Morfill, and H. E. Gaub, Friction of single polymers at surfaces, *Langmuir* **2006**, *22* (26), 11180.
- P. A. Neff, A. Serr, B. K. Wunderlich, and A. R. Bausch, Label-free electrical determination of trypsin activity by a silicon-on-insulator based thin film resistor, to appear in *ChemPhysChem* **2007**.

Bibliography

[1] H. Dautzenberg, W. Jaeger, J. Kötz, B. Philipp, C. Seidel, D. Stscherbina, *Polyelectrolytes*, Carl Hanser, Munich, **1994**.

[2] D. F. Evans, H. Wennerström, *The Colloidal Domain*, Wiley-VCH, New York, 2nd ed., **1999**.

[3] R. J. Hunter, *Foundations of Colloid Science*, *Vol. 1*, Oxford University Press, Oxford, **1986**.

[4] W. B. Russel, D. A. Saville, W. R. Schowalter, *Colloidal Dispersions*, Cambridge University Press, Cambridge, **1989**.

[5] A. Göthlich, S. Koltzenburg, G. Schornick, *Chem. Unserer Zeit* **2005**, *39*, 262.

[6] J. Gregory in *Chemistry and Technology of Water Soluble Polymers* (Ed.: C. A. Finch), Plenum Press, New York, **1983**.

[7] P. F. Luckham, J. Klein, *J. Chem. Soc. Faraday Trans.* **1990**, *86*, 1363.

[8] R. D. Vold, M. J. Vold, *Colloid and Interface Chemistry*, Addison-Wesley, London, **1983**.

[9] P. M. Claesson, A. Dedinaitea, O. J. Rojas, *Adv. Colloid Interf. Sci.* **2003**, *104*, 53.

[10] P. F. Luckham, M. S., *Adv. Coll. Interf. Sci.* **1997**, *73*, 1.

[11] J. Wang, *Nucl. Acids Res.* **2000**, *28*, 3011.

[12] B. Alberts, A. Johnson, J. Lewis, M. Raff, K. Roberts, P. Walter, *Molecular Biology of the Cell*, Garland Science, New York, 4th ed., **2002**.

[13] H. G. Hauthal, *NiU-Chemie* **1994**, *5*, 4.

[14] G. Wagner, *Waschmittel*, Wiley-VCH, Weinheim, 3rd ed., **2004**.

[15] J. Rieger, E. Hädicke, I. U. Rau, D. Boeckh, *Tenside Surf. Det.* **1997**, *34*, 430.

[16] J. Rieger, *Tenside Surf. Det.* **2002**, *39*, 221.

[17] R. E. Bulo, D. Donadio, A. Laio, F. Molnar, J. Rieger, M. Parrinello, *Macromol.* **2007**, *40*, 3437.

[18] A. Janshoff, M. Neitzert, Y. Oberdörfer, H. Fuchs, *Angew. Chem. Int. Ed.* **2000**, *39*, 3212.

[19] K. Svoboda, S. M. Block, *Annu. Rev. Biophys. Biomol. Struct.* **1994**, *23*, 247.

[20] S. T. Hess, S. Huang, A. A. Heikal, W. W. Webb, *Biochem.* **2002**, *41*, 697.

[21] X. Châtellier, T. J. Senden, J.-F. Joanny, J.-M. di Meglio, *Europhys. Lett.* **1998**, *41*, 303.

[22] P. J. Flory, *Statistical Mechanics of Chain Molecules*, Carl Hanser, Munich, **1989**.

[23] A. Yu. Grosberg, A. R. Khokhlov, *Statistical Physics of Macromolecules*, AIP Press, Woodbury, **1994**.

[24] G. J. Fleer, M. A. C. Stuart, J. M. H. M. Scheutjens, T. Cosgrove, B. Vincent, *Polymers at Interfaces*, Chapman & Hall, London, **1998**.

[25] E. Frey, K. Kroy, *Ann. Phys. (Leipzig)* **2005**, *14*, 20.

[26] I. N. Levine, *Quantum Chemistry*, Prentice-Hall, Upper Saddle River, 5th ed., **2000**.

[27] J. Thar, W. Reckien, B. Kirchner, *Top. Curr. Chem.* **2007**, *268*, 133.

[28] T. Murakhtina, J. Heuft, E. J. Meijer, D. Sebastiani, *ChemPhysChem* **2006**, *7*, 2578.

[29] D. Frenkel, B. Smit, *Understanding Molecular Simulation*, Academic Press, San Diego, 2nd ed., **2002**.

[30] J. Happel, H. Brenner, *Low Reynolds Number Hydrodynamics*, Martinus Nijhoff Publishers, The Hague, 2nd ed., **1983**.

[31] M. Doi, S. F. Edwards, *The Theory of Polymer Dynamics*, Oxford University Press, Oxford, **1986**.

[32] H. Risken, *The Fokker-Planck Equation*, Springer, Berlin, 2nd ed., **1996**.

[33] J. R. Blake, *Proc. Camb. Phil. Soc.* **1971**, *70*, 301.

[34] Y. W. Kim, R. R. Netz, *J. Chem. Phys.* **2006**, *124*, 114709.

[35] R. R. Netz, D. Andelman, *Phys. Rep.* **2003**, *380*, 1.

[36] R. Dennington II, T. Keith, J. Millam, K. Eppinnett, W. L. Hovell, R. Gilliland, *GaussView, vers. 3.09*, **2003**, Semichem, Inc., Shawnee Mission.

[37] W. Humphrey, A. Dalke, K. Schulten, *J. Mol. Graph.* **1996**, *14.1*, 33.

[38] POV-Team, *POV-Ray, vers. 3.6*, **2003**, http://www.povray.org/.

[39] *Adobe Illustrator CS, vers. 11*, **2003**, Adobe Systems, Inc., San Jose.

[40] *CorelDRAW, vers. 11*, **2002**, Corel Corporation, Inc., Ottawa.

[41] *Origin, vers. 7*, **2002**, OriginLab Corporation, Northampton.

[42] P. G. de Gennes, *Scaling Concepts in Polymer Physics*, Cornell University, Ithaca, **1979**.

[43] P. G. de Gennes, *Macromol.* **1981**, *14*, 1637.

[44] E. Eisenriegler, K. Kremer, K. Binder, *J. Chem. Phys.* **1982**, *77*, 6296.

[45] E. Eisenriegler, *Polymers near Surfaces*, World Scientific, Singapore, **1993**.

[46] P. Linse, *Macromol.* **1996**, *29*, 326.

[47] V. Yamakov, A. Milchev, O. Borisov, B. Dünweg, *J. Phys.: Condens. Matter* **1999**, *11*, 9907.

[48] A. Shafir, D. Andelman, *Phys. Rev. E* **2004**, *70*, 061804.

[49] C. Friedsam, H. E. Gaub, R. R. Netz, *Europhys. Lett.* **2005**, *72*, 844.

[50] A. Milchev, K. Binder, *Macromol.* **1996**, *29*, 343.

[51] J. McNamara, C. Y. Kong, M. Muthukumar, *J. Chem. Phys.* **2002**, *117*, 5354.

[52] E. A. Di Marzio, C. M. Guttman, *J. Chem. Phys.* **1991**, *95*, 1189.

[53] A. A. Gorbunov, A. M. Skvortsov, *J. Chem. Phys.* **1993**, *98*, 5961.

[54] L. I. Klushin, A. M. Skvortsov, F. A. M. Leermakers, *Phys. Rev. E* **2002**, *66*, 036114.

[55] F. W. Wiegel, *Introduction to Path-Integral Methods in Physics and Polymer Science*, World Scientific, Singapore, **1986**.

[56] D. Poland, H. A. Scheraga, *Theory of Helix-Coil Transitions in Biopolymers*, Academic Press, New York, **1970**.

[57] P. Hänggi, P. Talkner, M. Borkovec, *Rev. Mod. Phys.* **1990**, *62*, 251.

[58] S. Metzger, M. Müller, K. Binder, J. Baschnagel, *Macromol. Theory Simul.* **2002**, *11*, 985.

[59] S. Metzger, M. Müller, K. Binder, J. Baschnagel, *J. Chem. Phys.* **2003**, *118*, 8489.

[60] X. Châtellier, J.-F. Joanny, *Phys. Rev. E* **1998**, *57*, 6923.

[61] C. Friedsam, H. E. Gaub, R. R. Netz, *Biointerphases* **2006**, *1*, MR1.

[62] H.-J. Butt, B. Cappella, M. Kappl, *Surf. Sci. Rep.* **2005**, *59*, 1.

[63] P. S. Doyle, E. S. Shaqfeh, A. P. Gast, *J. Fluid Mech.* **1997**, *334*, 251.

[64] R. G. Larson, *J. Rheol.* **2005**, *49*, 1.

[65] *Rheology for Polymer Melt Processing*, (Eds.: J.-M. Piau, J.-F. Agassant), Elsevier, Amsterdam, **1996**.

[66] *The Wiley Polymer Networks Group Review Series, Vol. 2*, (Eds.: B. T. Stokke, A. Elgsaeter), Wiley, Chichester, **1999**.

[67] B. N. J. Persson, *Sliding Friction*, Springer, Berlin, 2nd ed., **2000**.

[68] J. Krim, *Am. J. Phys.* **2002**, *70*, 890.

[69] M. O. Robbins, M. H. Müser in *Modern Tribology Handbook* (Ed.: B. Bhushan), CRC Press, Boca Raton, **2001**.

[70] B. Maier, J. O. Rädler, *Phys. Rev. Lett.* **1999**, *82*, 1911.

[71] B. Maier, J. O. Rädler, *Macromol.* **2000**, *33*, 7185.

[72] S. A. Sukhishvili, Y. Chen, J. D. Müller, E. Gratton, K. S. Schweizer, S. Granick, *Nature* **2000**, *406*, 146.

[73] S. A. Sukhishvili, Y. Chen, J. D. Müller, E. Gratton, K. S. Schweizer, S. Granick, *Macromol.* **2002**, *35*, 1776.

[74] D. Pastré, O. Piétrement, A. Zozime, E. Le Cam, *Biopolym.* **2005**, *77*, 53.

[75] F. Kühner, M. Erdmann, L. Sonnenberg, A. Serr, J. Morfill, H. E. Gaub, *Langmuir* **2006**, *22*, 11180.

[76] C. J. Olson Reichhardt, C. Reichhardt, *Phys. Rev. E* **2006**, *74*, 051908.

[77] S. C. Bae, S. Granick, *Annu. Rev. Phys. Chem.* **2007**, *58*, 353.

[78] A. Schallamach, *Wear* **1963**, *6*, 375.

[79] J. M. Golden, *J. Phys. A: Math. Gen.* **1975**, *8*, 966.

[80] T. Charitat, J.-F. Joanny, *Eur. Phys. J. E* **2000**, *3*, 369.

[81] A. L. Ponomarev, T. D. Sewell, C. J. Durning, *Macromol.* **2000**, *33*, 2662.

[82] A. L. Ponomarev, T. D. Sewell, C. J. Durning, *J. Polym. Sci. B: Polym. Phys.* **2000**, *38*, 1146.

[83] P. Kraikivski, R. Lipowsky, J. Kierfeld, *Europhys. Lett.* **2004**, *66*, 763.

[84] P. Kraikivski, R. Lipowsky, J. Kierfeld, *Eur. Phys. J. E* **2005**, *16*, 319.

[85] P. Kraikivski, R. Lipowsky, J. Kierfeld, *Europhys. Lett.* **2005**, *71*, 138.

[86] T. G. Desai, P. Keblinski, S. K. Kumar, S. Granick, *Phys. Rev. Lett.* **2007**, *98*, 218301.

[87] M. Tanaka, J. Hermann, I. Haase, M. Fischer, S. G. Boxer, *Langmuir* **2007**, *23*, 5638.

[88] S. Cui, C. Liu, Z. Wang, X. Zhang, S. Strandman, H. Tenhu, *Macromol.* **2004**, *37*, 946.

[89] J. Long, Z. Xu, J. H. Masliyah, *Langmuir* **2006**, *22*, 1652.

[90] H. J. Kreuzer, M. Grunze, *Europhys. Lett.* **2001**, *55*, 640.

[91] T. Hugel, M. Rief, M. Seitz, H. E. Gaub, R. R. Netz, *Phys. Rev. Lett.* **2005**, *94*, 048301.

[92] H. J. Kreuzer, S. H. Payne, *Phys. Rev. E* **2001**, *63*, 021906.

[93] L. Livadaru, R. R. Netz, H. J. Kreuzer, *Macromol.* **2003**, *36*, 3732.

[94] F. Hanke, L. Livadaru, H. J. Kreuzer, *Europhys. Lett.* **2005**, *69*, 242.

[95] W. H. Press, S. A. Teukolsky, W. T. Vetterling, B. P. Flannery, *Numerical Recipes*, Cambridge University Press, Cambridge, 2nd ed., **1992**.

[96] G. He, M. O. Robbins, *Tribol. Lett.* **2001**, *10*, 7.

[97] G. M. McClelland in *Adhesion and Friction*, *Vol. 17* (Eds.: M. Grunze, H. J. Kreuzer), Springer, Berlin, **1989**, p. 1.

[98] O. Braun, Y. Kivshar, *The Frenkel-Kontorova Model*, Springer, Berlin, **2004**.

[99] B. N. J. Persson, *Phys. Rev. B* **1993**, *48*, 18140.

[100] J. Nelson Onuchic, P. G. Wolynes, *Curr. Op. Struct. Biol.* **2004**, *14*, 70.

[101] J. N. Israelachvili, *Intermolecular and Surface Forces*, Academic Press, London, 2nd ed., **1992**.

[102] D. Horinek, A. Serr, M. Geisler, T. Pirzer, T. Hugel, S. Q. Lud, J. A. Garrido, T. Scheibel, R. R. Netz, submitted to *Nature Mat.*

[103] D. Chandler, *Nature* **2005**, *437*, 640.

[104] K. A. Dill, T. M. Truskett, V. Vlachy, B. Hribar-Lee, *Annu. Rev. Biophys. Biomol. Struct.* **2005**, *34*, 173.

[105] W. F. van Gunsteren, S. R. Billeter, A. A. Eising, P. H. Hünenberger, P. Krüger, A. E. Mark, W. R. P. Scott, I. G. Tironi, *Biomolecular Simulation: The GROMOS96 manual and user guide*, Hochschulverlag AG an der ETH Zürich, Zurich, **1996**.

[106] H. J. C. Berendsen, J. P. M. Postma, W. F. van Gunsteren, J. Hermans in *Intermolecular Forces* (Ed.: B. Pullmann), D. Reidel Publishing, Dordrecht, **1981**.

[107] K. P. C. Vollhardt, N. Schore, *Organic Chemistry*, W. H. Freeman, New York, 3rd ed., **1998**.

[108] W. R. P. Scott, P. H. Hünenberger, I. G. Tironi, A. E. Mark, S. R. Billeter, J. Fennen, A. E. Todd, T. Hube, P. Kruger, W. F. van Gunsteren, *J. Phys. Chem. A* **1999**, *103*, 3596.

[109] E. Lindahl, B. Hess, D. van der Spoel, *J. Mol. Mod.* **2001**, *7*, 306.

[110] H. J. C. Berendsen, D. van der Spoel, R. van Drunen, *Comp. Phys. Comm.* **1995**, *91*, 43.

[111] H. J. C. Berendsen, J. P. M. Postma, A. DiNola, J. R. Haak, *J. Chem. Phys.* **1984**, *81*, 3684.

[112] T. Darden, D. York, L. Pedersen, *J. Chem. Phys.* **1993**, *98*, 10089.

[113] B. Hess, H. Bekker, H. J. C. Berendsen, J. G. E. M. Fraaije, *J. Comp. Chem.* **1997**, *18*, 1463.

[114] D. van der Spoel, E. Lindahl, B. Hess, A. R. van Buuren, E. Apol, P. J. Meulenhoff, D. P. Tieleman, A. L. T. M. Sijbers, K. A. Feenstra, R. van Drunen, H. J. C. Berendsen, *Gromacs User Manual, vers. 3.3*, http://www.gromacs.org, **2005**.

[115] J. Danielsson, J. Jarvet, P. Damberg, A. Gräslund, *Magn. Reson. Chem.* **2002**, *40*, S89.

[116] A. E. Nkodo, J. M. Garnier, B. Tinland, H. Ren, C. Desruisseaux, L. C. McCormick, G. Drouin, G. W. Slater, *Electrophoresis* **2001**, *22*, 2424.

[117] J.-J. Lee, G. G. Fuller, *Macromol.* **1984**, *17*, 375.

[118] J.-J. Lee, G. G. Fuller, *J. Coll. Interf. Sci.* **1985**, *103*, 569.

[119] T. C. McGlinn, D. J. Kuzmenka, S. Granick, *Phys. Rev. Lett.* **1988**, *60*, 805.

[120] G. J. Besio, R. K. Prud'homme, J. B. Benziger, *Macromol.* **1988**, *21*, 1070.

[121] S. Chin, D. A. Hoagland, *Macromol.* **1991**, *24*, 1876.

[122] S. H. Chang, I. J. Chung, *Macromol.* **1991**, *24*, 567.

[123] D. Nguyen, C. J. Clarke, A. Eisenberg, M. H. Rafailovich, J. Sokolov, G. S. Smith, *J. Appl. Cryst.* **1997**, *30*, 680.

[124] I. Soga, S. Granick, *Langmuir* **1998**, *14*, 4266.

[125] D. L. Anastassopoulos, N. Spiliopoulos, A. A. Vradis, C. Toprakcioglu, S. M. Baker, A. Menelle, *Macromol.* **2006**, *39*, 8901.

[126] J. H. Kim, W.-X. Shi, R. G. Larson, *Langmuir* **2007**, *23*, 755.

[127] J. Atkinson, C. J. Goh, N. Phan-Thien, *J. Chem. Phys.* **1984**, *80*, 6305.

[128] S. Grisafi, C. J. Durning, *J. Coll. Interf. Sci.* **1989**, *130*, 35.

[129] S. Grisafi, C. J. Durning, *J. Coll. Interf. Sci.* **1989**, *130*, 45.

[130] E. Manias, A. Subbotin, G. Hadziioannou, G. ten Brinke, *Mol. Phys.* **1995**, *85*, 1017.

[131] M. H. Cohen Stuart, G. J. Fleer, *Annu. Rev. Mat. Sci.* **1996**, *26*, 463.

[132] M. Chopra, R. G. Larson, *J. Rheol.* **2002**, *46*, 831.

[133] A. S. Panwar, S. Kumar, *J. Chem. Phys.* **2005**, *122*, 154902.

[134] D. G. Grier, *Curr. Op. Coll. Interf. Sci.* **1997**, *3*, 264.

[135] P. G. de Gennes, *J. Chem. Phys.* **1974**, *60*, 5030.

[136] F. Brochard-Wyart, *Europhys. Lett.* **1995**, *30*, 387.

[137] C. Sendner, R. R. Netz, *EPL* **2007**, *79*, 58004.

[138] R. Lipowsky, T. M. Nieuwenhuizen, *J. Phys. A.: Math. Gen.* **1988**, *21*, L89.

[139] C. Sendner, R. R. Netz, submitted to *PRL*.

[140] P. Reimann, *Phys. Rep.* **2002**, *361*, 57.

[141] O. Kratky, G. Porod, *Recl. Trav. Chim. Pays-Bas* **1949**, *68*, 1106.

[142] G. Porod, *Monatsh. Chem.* **1949**, *80*, 251.

[143] P. Dimitrakopoulos, *Phys. Rev. Lett.* **2004**, *93*, 217801.

[144] O. Hallatschek, E. Frey, K. Kroy, *Phys. Rev. Lett.* **2005**, *94*, 077804.

[145] T. L. Hill, *An Introduction to Statistical Thermodynamics*, Dover, New York, **1986**.

[146] F. Ritort, *J. Phys.: Condens. Matter* **2006**, *18*, R531.

[147] C. Ortiz, G. Hadziioannou, *Macromol.* **1999**, *32*, 780.

[148] G. Neuert, T. Hugel, R. R. Netz, H. E. Gaub, *Macromol.* **2006**, *39*, 789.

[149] J. F. Marko, E. D. Siggia, *Macromol.* **1995**, *28*, 8759.

[150] T. Hugel, M. Seitz, *Macromol. Rapid Commun.* **2001**, *22*, 989.

[151] R. R. Netz, *Macromol.* **2001**, *34*, 7522.

[152] L. Livadaru, H. J. Kreuzer, *Phys. Chem. Chem. Phys.* **2004**, *6*, 3872.

[153] Y. Sasanuma, S. Asai, R. Kumagai, *Macromol.* **2007**, *40*, 3488.

[154] J. Kierfeld, O. Niamploy, V. Sa-yakanit, R. Lipowsky, *Eur. Phys. J. E* **2004**, *14*, 17.

[155] L. Livadaru, R. R. Netz, H. J. Kreuzer, *J. Chem. Phys.* **2003**, *118*, 1404.

[156] F. Hanke, H. J. Kreuzer, *Phys. Rev. E* **2005**, *72*, 031805.

[157] S. Cui, C. Albrecht, F. Kühner, H. E. Gaub, *J. Am. Chem. Soc.* **2006**, *128*, 6636.

[158] B. Fückel, G. Hinze, G. Diezemann, F. Nolde, K. Müllen, J. Gauss, T. Basché, *J. Chem. Phys.* **2006**, *125*, 144903.

[159] Y.-H. Eom, H. Jeong, H. Orland, J. Yi, *Europhys. Lett.* **2006**, *76*, 325.

[160] A. Lamura, T. W. Burkhardt, G. Gompper, *Phys. Rev. E* **2001**, *64*, 061801.

[161] C. Storm, P. C. Nelson, *Phys. Rev. E* **2003**, *67*, 051906.

[162] M. J. Frisch, G. W. Trucks, H. B. Schlegel, G. E. Scuseria, M. A. Robb, J. R. Cheeseman, J. A. Montgomery Jr., T. Vreven, K. N. Kudin, J. C. Burant, J. M. Millam, S. S. Iyengar, J. Tomasi, V. Barone, B. Mennucci, M. Cossi, G. Scalmani, N. Rega, G. A. Petersson, H. Nakatsuji, M. Hada, M. Ehara, K. Toyota, R. Fukuda, J. Hasegawa, M. Ishida, T. Nakajima, Y. Honda, O. Kitao, H. Nakai, M. Klene, X. Li, J. E. Knox, H. P. Hratchian, J. B. Cross, C. Adamo, J. Jaramillo, R. Gomperts, R. E. Stratmann, O. Yazyev, A. J. Austin, R. Cammi, C. Pomelli, J. W. Ochterski, P. Y. Ayala, K. Morokuma, G. A. Voth, P. Salvador, J. J. Dannenberg, V. G. Zakrzewski, S. Dapprich, A. D. Daniels, M. C. Strain, O. Farkas, D. K. Malick, A. D. Rabuck, K. Raghavachari, J. B. Foresman, J. V. Ortiz, Q. Cui, A. G. Baboul, S. Clifford, J. Cioslowski, B. B. Stefanov, G. Liu, A. Liashenko, P. Piskorz, I. Komaromi, R. L. Martin, D. J. Fox, T. Keith, M. A. Al-Laham, C. Y. Peng, A. Nanayakkara, M. Challacombe, P. M. W. Gill, B. Johnson, W. Chen, M. W. Wong, C. Gonzalez, J. A. Pople, *Gaussian 03, rev. C01*, **2003**, Gaussian, Inc., Wallingford.

[163] C. T. Lee, W. T. Yang, R. G. Parr, *Phys. Rev. B* **1988**, *37*, 785.

[164] A. D. Becke, *J. Chem. Phys.* **1993**, *98*, 5648.

[165] R. Krishnan, J. S. Binkley, R. Seeger, J. A. Pople, *J. Chem. Phys.* **1980**, *72*, 650.

[166] M. J. Frisch, J. A. Pople, J. S. Binkley, *J. Chem. Phys.* **1984**, *80*, 3265.

[167] C. M. Venkatachalam, G. N. Ramachandran, *Annu. Rev. Biochem.* **1969**, *38*, 45.

[168] I. A. Solov'yov, A. V. Yakubovitch, A. V. Solov'yov, W. Greiner, *J. Exp. Theo. Phys.* **2006**, *102*, 314.

Personal Acknowledgements – Persönliche Danksagung

In addition to the acknowledgments already given for the help in accomplishing this work, I would like to give some very personal acknowledgments.

First of all, I would like to thank many people who have made life in Munich versatile, exciting, and enjoyable.

Markus Breidenich machte seinem Namen als Hochkulturbeauftragten alle Ehre. Bei ihm ist fraglich, ob das Vergnügen gegenseitig war – ich jedenfalls finde, dass sich Hoch- und Subkultur sehr gut ergänzt haben. Sebastian Fischer machte lange Abende noch länger *und* interessanter. Das liegt ohne Zweifel an seinem facettenreichen Interesse. An dieser Stelle auch schöne Grüße an Andrea.

Hirofumi Wada has made wonderful impressions in various ways and I had a marvelous time with him. See you soon, Hiro, in whatever place. Alfredo Alexander-Katz is quite a character. Probably also due to that I was so lucky and happy to share the office and many great hours (in private intimacy) with him. Greetings and hugs to him and Sofia. I truly miss the wonderful time with (and sometimes even the endless and ever-repeated stories of) Jason Derouchey, a really American American, and Manoel Manghi, a truly French Frenchman. Álvaro Tejero Cantero is one of two guys I admire for their seemingly never-ending thirst for foreign culture and literature. Thanks for also being a great companion and perfect househusband. In many ways I had wonderful times with Daniel Peña Arteaga. Keep up with your relaxed spirit—I might need some calming words from you for my next job. Thanks also to Ioannis Daoutidis for completing our party.

Marta Balbás Gambra hat neben vielem anderen spanisches Flair, guten Wein und immer gute Laune mit eingebracht. Vielen Dank. Christian Sendner ist der beste Kollege, den man sich vorstellen kann. Hauptsache, man hält ihn mit Essen irgendwelcher Form bei Laune. Außerdem gehört er zusammen mit Thomas Einert, Dominik Horinek, Joachim Dzubiella, Felix Sedlmeier und Sebastian zu einem Team von Kollegen, mit denen es immer größten Spaß gemacht hat, Fachgespräche auch einmal sportlich und dennoch am grünen Tisch auszutragen. Joachim kann es sogar auf dem echten Rasen am besten. Dabei sind Hannes Lüling, Javier Madronero, Immanuel Kalcher, Ferdinand Kühner und Álvaro aber fast genauso gut. Franz Xaver Walther Eberhard Schlagberger war immer für irgendwelchen Unsinn zu haben. Meistens hat er dann sogar "something like a car" zur Verfügung gestellt.

Sonja Ortner, die gute Seele der Arbeitsgruppe, war immer hilfsbereit, zuvorkommend und freundlich – und dass, obwohl sie aus Österreich kommt wie übrigens auch Udo Jürgens. Vielen Dank für alles. Roland Netz hat zwischen Arbeitseifer und Konferenzreisen immer mal wieder mit Winterschulen, Wandertagen, Sommer- und Weihnachtsfeiern sowie in Santa Barbara auch mit Hilfe seiner ganzen Familie für gute und manchmal auch äußerst ausgelassene Stimmung (siehe beispielsweise Antholz) gesorgt.

I wish to express my gratitude to people I had the pleasure to work and share good times with, namely Douwe Bonthuis, Michael Hinczewski, Prabal Maiti, David Hofmann, Julius Schulz, Shavkat Mamatkulov, Vladimir Lobaskin, Jir̂í Janeĉek, Hoda Boroudjerdi and Ali Naji, Yong Woon Kim, Thomas Westphal, Swetlana Jungblut, Julia Schwartz, Ulrich Gerland and Richard Neher in reverse chronological order. Auch mit Felix Hanke und Matthias Erdmann ging es über rein fachliche Zusammenarbeit hinaus. Danke auch an Euch.

Of course there are also friends where I did not have the luck to live closer to them during my time in Munich. Let me keep the list short, too short of course, and limit my acknowledgment to Valérie and Paolo (Nicoud-)Galletto and Claire Chassagne.

Hier zum ersten Mal und ausnahmsweise *ohne* Nennung der mittlerweile erworbenen akademischen Grade darf ich mich bei den dicksten (**“Wer ist hier dick?”**) und langjährigsten Freunden bedanken: Marcel Ahijado Salomon, Patrik Plattner und Ulrich Wüllner sind einfach nicht abzuschütteln – hoffentlich nie im Leben! Andrew Smith und Ingo Stefes geben dem Wort Heimkehr eine tiefere Bedeutung. Natürlich grüße ich auch Karin, Petra und Carolin.

Besonders herzlicher Dank gilt Ursula und Dieter Lemberg für ihre über Jahre hinweg geleistete Unterstützung.

Am Schluss, aber damit auch auf gewisse Weise an erster Stelle kommt mein Vater, der mir immer hilft, mich berät oder sonstwie von der Arbeit abhält. Nie vergessen werde ich meine Mutter, der ich immer mehr verdanke, wie mir scheint, und die jetzt noch stolzer wäre als nach meiner letzten eingereichten Arbeit.

Zusammenfassung

In der vorliegenden Arbeit mit dem Titel

Dynamik einzelner Polymere an Oberflächen

wird das Antwortverhalten einzelner Polymeren auf externe Kräfte in der Nähe von Oberflächen untersucht.

In Kapitel 1 wird die Motivation für die bearbeiteten Themen erläutert, und Bezüge zu theoretischen und experimentellen Methoden sowie technischen Anwendungen werden hergestellt.

Kapitel 2 gibt eine Einführung in die Adsorption von idealen Polymeren auf ebenen, homogenen Oberflächen. Es wird gezeigt, dass die Methode der Polymerpfadintegrale und das Poland-Scheraga-Modell äquivalente Beschreibungen darstellen. In Brownschen Dynamik-Simulationen wird die Adsorption von grobgekörnten Polymermodellen an ebenen Oberflächen simuliert. Das wegen endlich langer Polymere notwendige Fenster für Simulationszeiten, das die Abbildung auf den thermodynamischen Grenzfall eines unendlich langen Polymers ermöglicht, wird diskutiert. Weiterhin wird die Methode der Kraftspektroskopie mittels Atomkraftmikroskope (AFM) und ihre Anwendung auf Polymeradsorption besprochen.

In Kapitel 3 wird die Reibung eines einzelnen Polymers analysiert, das an eine feste Oberfläche adsorbiert ist. Der Einfluss solcher Reibung auf AFM-Kraftmessungen wird erläutert und ein Experiment zur Messung von Reibungskonstanten vorgeschlagen. Das Frenkel-Kontorova-Modell wird im Zusammenhang mit Polymerreibung besprochen. Mittels dieses Modelles wird erläutert, wie inhomogene Oberflächen in Form einer gewellten Potenziallandschaft die Reibung des Lösungsmittels verstärken. Der Einfluss der (In-)Kommensurabilität und der Polymerlänge wird aufgezeigt. Molekulardynamik-Simulationen mit atomistischer Auflösung werden verwendet, um die Reibung eines Polypeptids an der Wasser-Diamant-Grenzfläche zu untersuchen. Auf hydrohob terminiertem Diamant ist die Mobilität nur geringfügig gegenüber der in reinem Wasser verringert. Auf OH-terminierten, hydrophilen Oberflächen hingegen ist die Bewegung wegen des wiederkehrenden Bruchs und der Bildung von Wasserstoffbrücken durch wechselndes Kleb- und Rutschverhalten gekennzeichnet. Die Mobilität des Polypeptids ist mehr als dreißigfach verringert gegenüber der auf hydrophobem Diamant. Solche drastischen Unterschiede sind aufgrund sehr ähnlicher

Adsorptionskräfte auf hydrophobem und hydrophilem Material, die auch experimentell nachgewiesen wurden, völlig unerwartet.

Das Adsorptionsverhalten fern des Gleichgewichts wird in Kapitel 4 diskutiert. Ein an einem Ende seitlich zur Oberfläche gezogenes Polymer adsorbiert *stärker*. Die Rauigkeit der Kette in Richtung der Oberflächennormalen wird durch das Ziehen verringert, so dass die Entropiekosten für die Adsorption abnehmen. Mittels einer effektiven Kuhnlänge wird der Effekt auf skalentheoretischer Ebene quantitativ beschrieben. Für Polymere im Scherfluss und nahe am Adsorptionsübergang wird ein ähnlicher Effekt beobachtet. Im Bereich starker Adsorption nimmt das Polymer eine flache Konfiguration auf der Oberfläche an, daher hat hier der Scherfluss keinen Einfluss. Hydrodynamische Wechselwirkungen zwischen den Monomeren sowie mit der Wand bewirken einen entgegengesetzten Trend; das Polymer wird von der Wand weggetrieben und die Adsorption vermindert. Gleichzeitig wird statt des sonst üblichen kontinuierlichen Desorptionsübergangs ein diskontinuierlicher Übergang beobachtet. Auf Oberflächen mit gewelltem Potenzial wird durch laterales Ziehen von einzelnen Teilchen deren Desorption induziert, da sie im Mittel einer geringeren Adsorptionskraft ausgesetzt sind. Die Analyse dieses Effekts zeigt, dass für seitlich auf gewellten Oberflächen gezogene Polymere der Effekt der verstärkten Adsorption durch verminderte Kettenrauigkeit überwiegen sollte.

Die Elastizität einzelner Polymere wird in Kapitel 5 auf der Grundlage von diskreten Polymermodellen untersucht. Ein solches an ein Freely Rotating Chain-Polymer (FRC) angelehntes, mit dehn- und biegbaren Bindungen ausgestattetes Modell wird vorgeschlagen und mittels der Transfermatrixmethode numerisch gelöst. Mittels dieser numerisch exakten Methode wird gezeigt, dass andere, auf der Separation von entropischer und enthalpischer Elastizität basierende Näherungen in bestimmten Fällen versagen. Die Transfermatrixmethode wird auf alternierende Copolymere erweitert. Dieser Formalismus wird auf Polypeptide angewandt, für die aus quantenchemischen Rechnungen die mikroskopischen Bindungspotenziale erhalten werden. Die Torsionssteifigkeit eines Bindungstyps in Polypeptiden wird anhand von *ab initio* Berechnungen nachgewiesen und ein erweitertes FRC-Modell vorgestellt, das die rotationssteife Bindung mittels einer effektiven, zwei mikroskopische Bindungen umfassenden Bindung überbrückt. Mit Parametern für Polypeptide wird dieser Formalismus angewandt.

Teile dieser Arbeit wurden bereits in wissenschaftlichen Journalen veröffentlicht, sind an solche submittiert oder in Vorbereitung dazu. Darunter sind

- A. Serr and R. R. Netz, Pulling adsorbed polymers from surfaces with the AFM: stick *vs.* slip, peeling *vs.* gliding, *Europhys. Lett.* **2006**, *73* (2), 292.
- A. Serr and R. R. Netz, Enhancing polymer adsorption by lateral pulling, *EPL* **2007**, *78* (6), 68006.
- D. Horinek, A. Serr, M. Geisler, T. Pirzer, U. Slotta, S. Q. Lud, J. A. Garrido, T. Scheibel, T. Hugel, and R. R. Netz, Single molecule peptide hydrophobicity results from the interplay of water structure effects and dispersion interaction, submitted to *Nature Mat.*, **2007**.
- D. Horinek, A. Serr, D. Bonthuis, and R. R. Netz, Hydrophobic attraction studied by molecular dynamics, submitted to *Langmuir*, **2007**.
- A. Serr, C. Sendner, and R. R. Netz, Non-equilibrium polymer adsorption, in preparation, **2007**.
- A. Serr, D. Horinek, and R. R. Netz, Polymer super-lubricity on hydrophobic *vs.* high-friction stick-slip motion on hydrophilic surfaces, in preparation, **2007**.
- A. Serr, F. Hanke, H. J. Kreuzer, and R. R. Netz, Stretching of discrete semi-flexible extensible polymer chains, in preparation, **2007**.
- F. Hanke, A. Serr, R. R. Netz, and H. J. Kreuzer, On the rotational rigidity and elastic response of polypeptides, in preparation, **2007**.

Weitere Beiträge, die nicht in dieser Arbeit behandelt wurden, liegen veröffentlicht vor unter den Titeln

- H. Boroudjerdi, Y. W. Kim, A. Naji, R. R. Netz, X. Schlagberger, and A. Serr, Statics and dynamics of strongly charged soft matter, *Phys. Rep.* **2005**, *416* (3-4), 129.
- A. Serr and R. R. Netz, Polarizabilities of hydrated and free ions derived from DFT calculations, *Int. J. Quant. Chem.* **2006**, *106* (14), 2960.
- F. Kühner, M. Erdmann, L. Sonnenberg, A. Serr, J. Morfill, and H. E. Gaub, Friction of single polymers at surfaces, *Langmuir* **2006**, *22* (26), 11180.
- P. A. Neff, A. Serr, B. K. Wunderlich, and A. R. Bausch, Label-free electrical determination of trypsin activity by a silicon-on-insulator based thin film resistor, to appear in *ChemPhysChem* **2007**.